

ERBIUM DOPED GaAs/AlGaAs QUANTUM WELLS
AND
NORMAL MODE COUPLING OF SEMICONDUCTOR MICROCAVITIES

by

Eric Karl Lindmark

A Dissertation Submitted to the Faculty of the
COMMITTEE ON OPTICAL SCIENCES (GRADUATE)

In Partial Fulfillment of the Requirements
For the Degree of

DOCTOR OF PHILOSOPHY

In the Graduate College

THE UNIVERSITY OF ARIZONA

1997

INFORMATION TO USERS

This manuscript has been reproduced from the microfilm master. UMI films the text directly from the original or copy submitted. Thus, some thesis and dissertation copies are in typewriter face, while others may be from any type of computer printer.

The quality of this reproduction is dependent upon the quality of the copy submitted. Broken or indistinct print, colored or poor quality illustrations and photographs, print bleedthrough, substandard margins, and improper alignment can adversely affect reproduction.

In the unlikely event that the author did not send UMI a complete manuscript and there are missing pages, these will be noted. Also, if unauthorized copyright material had to be removed, a note will indicate the deletion.

Oversize materials (e.g., maps, drawings, charts) are reproduced by sectioning the original, beginning at the upper left-hand corner and continuing from left to right in equal sections with small overlaps. Each original is also photographed in one exposure and is included in reduced form at the back of the book.

Photographs included in the original manuscript have been reproduced xerographically in this copy. Higher quality 6" x 9" black and white photographic prints are available for any photographs or illustrations appearing in this copy for an additional charge. Contact UMI directly to order.

UMI

A Bell & Howell Information Company
300 North Zeeb Road, Ann Arbor MI 48106-1346 USA
313/761-4700 800/521-0600

ERBIUM DOPED GaAs/AlGaAs QUANTUM WELLS
AND
NORMAL MODE COUPLING OF SEMICONDUCTOR MICROCAVITIES

by

Eric Karl Lindmark

A Dissertation Submitted to the Faculty of the
COMMITTEE ON OPTICAL SCIENCES (GRADUATE)

In Partial Fulfillment of the Requirements
For the Degree of

DOCTOR OF PHILOSOPHY

In the Graduate College

THE UNIVERSITY OF ARIZONA

1997

UMI Number: 9729495

UMI Microform 9729495
Copyright 1997, by UMI Company. All rights reserved.

**This microform edition is protected against unauthorized
copying under Title 17, United States Code.**

UMI
300 North Zeeb Road
Ann Arbor, MI 48103

THE UNIVERSITY OF ARIZONA ®
GRADUATE COLLEGE

As members of the Final Examination Committee, we certify that we have read the dissertation prepared by Eric K. Lindmark

entitled Erbium Doped GaAs/AlGaAs Quantum Wells and Normal Mode

Coupling of Semiconductor Microcavities

and recommend that it be accepted as fulfilling the dissertation requirement for the Degree of Doctor of Philosophy

Galina Khitrova

Galina Khitrova

3-28-97

Date

Hyatt Gibbs

Hyatt M. Gibbs

3-28-97

Date

Seppo Honkanen

Seppo Honkanen

3-28-97

Date

Date

Date

Final approval and acceptance of this dissertation is contingent upon the candidate's submission of the final copy of the dissertation to the Graduate College.

I hereby certify that I have read this dissertation prepared under my direction and recommend that it be accepted as fulfilling the dissertation requirement.

Galina Khitrova

Galina Khitrova

3-28-97

Dissertation Director

Date

STATEMENT BY AUTHOR

This dissertation has been submitted in partial fulfillment of requirements for an advanced degree at The University of Arizona and is deposited in the University Library to be made available to borrowers under rules of the Library.

Brief quotations from this dissertation are allowable without special permission, provided that accurate acknowledgment of source is made. Requests for permission for extended quotation from or reproduction of this manuscript in whole or in part may be granted by the head of the major department or the Dean of the Graduate College when in his or her judgment the proposed use of the material is in the interests of scholarship. In all other instances, however, permission must be obtained from the author.

SIGNED:  _____

ACKNOWLEDGEMENTS

I wish to thank my advisor Galina Khitrova for giving me an opportunity to do research in a top-notch research group. She has taught me the value of doing quality research as well as the benefits of a skin-scorching sauna. I also want to thank Hyatt Gibbs for his scientific insights, as well as helping me become an expert at using a fax machine.

Now I will thank my fellow students with whom I have worked for the past many years: Jill Berger, Ove Lyngnes, Tom Nelson, John Prineas, and Dave Wick. Without them, I probably would have gone crazy and ended up on a median selling the Tucson Citizen for alcohol money.

I also say good luck to the newest members of the group: Sahnggi Park and Eun Seong Lee.

Thanks goes to my Russian collaborators whom I have only met by email. They are A.V. Kavokin, M.A. Kaliteevski, O.B. Gusev, M.S. Bresler, I.N. Yassievich, B.P. Zakharchenya, and V.F. Masterov.

Thanks goes to the U.S. Government who paid for the majority of my stay at the University of Arizona. My first year I was on a Grant in Aid of Areas of National Need (GAANN) Fellowship, and my last two and a half years were supported by the Air Force's Palace Knight program. The middle part of my stay was also supported on government grants of some sort.

I want to thank my maternal grandparents for their support. My grandfather was a professor of Electrical Engineering at the University of Minnesota and encouraged me during my studies of Electrical Engineering as an undergraduate at Virginia Tech as well as a master's student at the University of Minnesota. My grandmother has been very supportive during my stay here offering many reminiscences of her and my grandfather's travails while he was getting his Ph.D. She told me she helped retype his dissertation five times. I am glad I live in the days of word-processors.

I want to especially thank my parents for moral as well as financial support. When I graduated from Minnesota with my master's degree and couldn't find a job, they did not kick me out into the street. When I decided to go back to school they not only encouraged me, but also moved two U-Haul trailers full of stuff from Minnesota to Tucson thus freeing up my bedroom for other uses.

Special thanks goes to wife Julie for putting up with me and giving me the support I needed. I also want to thank my son Jacob even though he was a major cause of sleep deprivation during the writing of this dissertation.

To Julie and Jake, may it make you rich

TABLE OF CONTENTS

	page
LIST OF ILLUSTRATIONS	8
LIST OF TABLES	12
ABSTRACT	13
1. Overall Introduction	15
2. Introduction to Erbium-Doped Semiconductors	18
<i>Some History of the Rare Earth Erbium</i>	18
<i>Erbium in Semiconductors</i>	21
<i>Light from Erbium-Doped Semiconductors</i>	24
3. Erbium Doped AlGaAs/GaAs Quantum Wells	28
<i>Introduction</i>	28
<i>Experimental Procedure</i>	29
Sample preparation	29
Experimental measurements	31
<i>Experimental Results</i>	37
Er-induced Ga-Al interdiffusion and Er diffusion	37
Er-photoluminescence and defects induced by Er	47
<i>Discussion of Er-Luminescence Excitation and De-Excitation Mechanism</i>	56
Excitation and de-excitation processes of erbium luminescence	56
Analysis of experimental data	59
<i>Conclusions</i>	61
4. Normal Mode Coupling	62
<i>Introduction</i>	62
<i>Our Samples</i>	66
<i>Experimental Setup</i>	68
<i>NMC20 Measurement</i>	69
<i>NMC22 Measurements</i>	72

TABLE OF CONTENTS—*Continued*

	page
<i>NMC28 Measurement</i>	74
<i>Nonlinear Experiment</i>	76
<i>Other NMC Work We Have Done</i>	83
5. Normal Mode Coupling in a Microcavity With Two Different Quantum Wells	84
<i>Introduction</i>	84
<i>Experimental Discussion</i>	84
<i>Theory</i>	85
<i>Discussion of Results</i>	96
<i>Conclusions</i>	97
APPENDIX A Summary of Erbium Sample Growth	100
APPENDIX B Summary of NMC Sample Growth	103
REFERENCES	106

LIST OF ILLUSTRATIONS

		page
FIGURE 2.1	The periodic table of the elements with the lanthanides or rare earths in the second to the bottom row.....	20
FIGURE 2.2	Some of the energy transitions in Er^{3+}	22
FIGURE 2.3	QW structure on the left used to try and match an erbium transition on the right. ΔE_{ch} is tuned to equal ΔE_{Er} by varying the thickness of the QW.....	26
FIGURE 3.1	Conduction band structure for Er20, 21, 22, and 23	30
FIGURE 3.2	Erbium concentration as a function of Er cell temperature.....	32
FIGURE 3.3	Absorption measurement setup	34
FIGURE 3.4	Temperature dependent PL measurement setups for a) transmission geometry and b) reflection geometry.....	36
FIGURE 3.5	SIMS profile for Er26.....	38
FIGURE 3.6	SIMS profiles for a) Er20, b) Er21, and c) Er23.....	39
FIGURE 3.7	High resolution PL spectra of a) Er26, b) Er21, and c) Er29	40
FIGURE 3.8	SIMS profiles for a) Er25 and b) Er34	42
FIGURE 3.9	Absorption spectra for Er20, Er22, Er21, and Er23. Curves are separated vertically by 1.0 for clarity.....	43
FIGURE 3.10	High resolution PL spectra of Er21 at $T_1 = 5\text{K}$ (solid line) and $T_2 = 40\text{K}$ (dashed line)	47
FIGURE 3.11	High resolution PL spectra taken at 1.8K of a) Er21 and b) Er22	49
FIGURE 3.12	PL spectrum of Er23 taken at 10.5 K demonstrating the presence of shallow defect states in Er-doped GaAs/AlGaAs.....	51

LIST OF ILLUSTRATIONS—*Continued*

	page
FIGURE 3.13 Temperature evolution of the PL spectra of Er23 demonstrating the temperature quenching of the <i>Db</i> and <i>Dc</i> defect lines	53
FIGURE 3.14 Temperature evolution of the PL spectra of Er23 demonstrating the temperature quenching of the <i>a</i> , <i>b</i> , and <i>c</i> lines for the ranges a) 12 K to 60 K and b) 70 K to 200 K.....	54
FIGURE 3.15 a) Temperature dependence of the intensities of the <i>Db</i> defect line and the erbium <i>a</i> , <i>b</i> , and <i>c</i> lines for Er23. b) Temperature dependence of the intensities of the erbium <i>a</i> lines for Er29 and Er23.	55
FIGURE 3.16 PL spectrum taken at 10 K of Er23 in a wide spectral range (800-1800 nm).....	57
FIGURE 3.17 Energy level diagram and transition scheme for the Auger excitation of erbium ions via <i>Da</i> , <i>Db</i> , and <i>Dc</i> defect centers. For comparison of the defect and f-f transition energies, the positive direction of the energy axis for the Er ³⁺ ion levels is reversed.	60
FIGURE 4.1 Structure of a DBR microcavity. Top and bottom mirrors are 10 and 12.5 periods of GaAs and AlAs quarter wave layers. The λ cavity contains an In _{0.03} Ga _{0.97} As QW.....	65
FIGURE 4.2 a) Absorption spectrum of 20 InGaAs QW's (NMC21) used in our NMC samples. Spectrum taken at 4K. b) Calculated reflectivity spectrum of NMC20 showing Fabry-Perot dip at 873 nm.	67
FIGURE 4.3 a) White light absorption setup. b) White light reflectivity setup.	70
FIGURE 4.4 Reflectivity spectrum of NMC20 taken at 4K near minimum splitting.	71
FIGURE 4.5 a) Reflectivity spectra for different detunings on sample NMC22 at 4K. Spectra are separated for clarity. b) Anticrossing diagram for NMC22 taken at 4K. The beam spot positions are not the same as a), but are taken from the same sample.....	73

LIST OF ILLUSTRATIONS—*Continued*

		page
FIGURE 4.6	a) Reflectivity spectrum for NMC28 at 4K showing NMC with the quantum well HH exciton. b) Reflectivity spectrum for NMC28 at 4K showing NMC with the quantum well LH exciton. c) Reflectivity spectrum for NMC28 at 4K showing NMC with the GaAs exciton of the cavity spacer and mirror layers.....	75
FIGURE 4.7	Experimental setup for the cw nonlinear pump-probe measurements made on sample NMC22.....	77
FIGURE 4.8	NMC22 pump-probe transmission spectra with increasing pump power from a) to f). Included in each plot is a dashed reference transmission spectrum of the probe alone.....	79
FIGURE 4.9	a) Measured nonlinear absorption measurement of NMC21 at 4K. Arrow shows direction of increasing pump power. b) Nonlinear index spectrum calculated using the Kramers-Kronig transformation of the absorption curves of a). c) Calculated NMC transmission curves using the index curves of b) and transfer matrix method.....	81
FIGURE 5.1	Structure of the microcavity. Top and bottom mirrors are 10 and 12.5 periods of GaAs and AlAs quarter wave layers. The $3/2 \lambda$ cavity contains two $\text{In}_{0.03}\text{Ga}_{0.97}\text{As}$ QW's made with slightly different concentrations of indium.....	86
FIGURE 5.2	a) Anticrossing diagram of NMC27 with ≈ 5.2 nm between the heavy-hole excitons of the two QWs. Solid lines represent measured data while large circles represent calculated results. b) Reflectivity spectra of NMC27 corresponding to detunings of I) $y = +3.2$ mm, II) $y = +2.0$ mm, III) $y = +1.2$ mm, IV) $y = +0.4$ mm and V) $y = -0.8$ mm. The solid curves represent measured data while the dashed curves represent calculated results. The plots are separated for clarity.....	87

LIST OF ILLUSTRATIONS—*Continued*

		page
FIGURE 5.3	a) Anticrossing diagram of NMC30 with ≈ 2.6 nm between peaks. b) Reflectivity spectra of NMC30 corresponding to detunings of I) $y = +1.3$ nm, II) $y = -1.0$ nm, III) $y = -1.8$ nm, IV) $y = -2.4$ nm and V) $y = -4.7$ nm.	88
FIGURE 5.4	a) Anticrossing diagram of NMC23 with ≈ 1.4 nm between peaks. b) Reflectivity spectra of NMC23 corresponding to detunings of I) $y = +1.0$ nm, II) $y = +0.5$ nm, III) $y = 0.0$ nm, IV) $y = -0.5$ nm and V) $y = -0.8$ nm.	89
FIGURE 5.5	Reflectivity spectra of NMC27 corresponding to detunings of (I) -3.82 nm, (II) 0.0 nm, (III) 4.01 nm, and (IV) 7.14 nm. The solid curves represent measured data while the dashed curves represent calculated results from the simple dispersion model. The plots are separated for clarity.	93
FIGURE 5.6	Reflectivity spectra of NMC30 corresponding to detunings of (I) -5.42 nm, (II) -0.41 nm, (III) 0.0 nm, (IV) 0.56 nm, and (V) 3.27 nm.	94
FIGURE 5.7	Reflectivity spectra of NMC23 corresponding to detunings of (I) -4.69 nm, (II) -2.83 nm, (III) 0.0 nm, (IV) 2.32 nm, and (V) 3.30 nm.	95

LIST OF TABLES

	page
TABLE 3.1 Erbium concentrations, determined by SIMS, of the grown structures	31
TABLE 5.1 Parameters used in the calculations for the three different samples.....	92

ABSTRACT

This dissertation investigated two different types of semiconductor heterostructures grown by molecular beam epitaxy. The first were erbium-doped GaAs/AlGaAs quantum well structures with concentrations of Er in the range of 10^{17} - 2×10^{19} cm⁻³. Photoluminescence (PL) of Er³⁺ ions and Er-induced defects were studied at liquid helium and higher temperatures. A strong diffusion of erbium and interdiffusion of gallium and aluminum ions were observed at the boundary of the GaAs/AlGaAs quantum wells which led, at high erbium concentrations, to the degradation of the quantum wells and macroscopic (average) leveling of the erbium and aluminum concentrations over the whole semiconductor structure. From high-resolution PL spectra the existence of three types of Er centers was deduced that differ by the positions of fine structure lines, PL lifetimes, and PL temperature dependence. Our results indicate that these centers are accompanied by the appearance of three types of carrier traps. Our experiments give evidence that the carriers captured into these traps control the Auger excitation of Er ions. Besides erbium luminescence at 1.54 μ m, we have observed luminescence of erbium ions from upper excited states at 0.82 and 0.98 μ m which demonstrates the possibility of realizing a three-level scheme of light emission.

The second structures investigated were GaAs/AlAs microcavities containing different numbers of identical and non-identical quantum wells. The normal mode coupling behavior of these structures was studied, including the differences from the atomic case. For the identical quantum well structures we examined their linear and

nonlinear behavior and modeled this behavior using a transfer matrix method. For the non-identical quantum well case we measured three-dip reflectivity spectra characteristic of three coupled oscillators. A theoretical model based on a nonlocal dielectric response and a transfer matrix method was used to model the microcavities and yielded good agreement with experiment. A simpler model using dispersion theory was also described that gave good qualitative agreement to the measurements.

Chapter 1

Overall Introduction

This dissertation is the melding of two somewhat different topics. The first to be covered is the study of semiconductor crystals that have had various amounts of erbium put into them. The second topic is the study of semiconductor quantum wells inside of a microcavity and some of their collective effects. The glue holding these topics together is that all of the semiconductor heterostructures studied here were made in the same molecular beam epitaxy (MBE) machine in our lab in Tucson by Professors Galina Khitrova and Hyatt Gibbs, and also that we spent many hours in the lab measuring both types of samples.

MBE, invented in the 1960's, involves the deposition of very thin layers of material under ultra-high vacuum conditions [Wolf and Tauber (1986)]. The layer thicknesses are so precisely controlled that individual atomic layers can be deposited. The types of atoms that we deposit on our substrates are aluminum (Al), arsenic (As), erbium (Er), gallium (Ga), and indium (In).

The work described in this dissertation begins after the samples have been grown. Many types of measurements have been performed that have given numerous sorts of information: the exciting news that a breakthrough has occurred, strange information that is not understood until after much thought and argument, or even the not so nice report that the latest sample grown needs to be redone or improved.

The precise control provided by the MBE machine allows many different types of heterostructures to be grown including quantum wells (QW's), superlattices, mirrors, and vertical cavity surface emitting lasers (VCSEL's). A QW consists of a lower bandgap crystal, usually less than 100 Å thick sandwiched between higher bandgap crystals [Peyghambarian *et al.* (1993)]. Typically the well material is GaAs, with an energy gap of around 1.5 eV. $\text{Al}_x\text{Ga}_{1-x}\text{As}$ (aluminum gallium arsenide) is used for the barrier, where x can vary from 0 to 1. The bandgap of $\text{Al}_x\text{Ga}_{1-x}\text{As}$ can be varied from that of GaAs to approximately 2 eV (when $x=0.45$, and where the bandgap of $\text{Al}_x\text{Ga}_{1-x}\text{As}$ becomes indirect). The nice thing about the GaAs/ $\text{Al}_x\text{Ga}_{1-x}\text{As}$ system is that the lattice constants match throughout all of the values of x so almost no mechanical strain is introduced. The confinement caused by the QW lets the transition energy of the electrons within the well structure be tailored by the thickness of the well and the difference in bandgap of the well and barrier materials.

In chapters 2 and 3 we discuss QW's that have been doped with erbium. Chapter 2 gives background information, a motivation of why we put erbium in QW's, and what we hoped to see. Chapter 3 gives a detailed account of the samples that were grown, the measurements that were performed on them, and what we actually did see.

In chapters 4 and 5 we also examine samples that are QW's, but now the wells are InGaAs (indium gallium arsenide) and the barriers GaAs. These QW's rather than being doped with Er are instead sandwiched between mirrors made of alternating quarter-wave layers of crystal material. This structure is the VCSEL or microcavity, and we examine an interesting phenomenon found in them under certain conditions called normal mode

coupling (NMC). Chapter 4 introduces NMC and describes several measurements done on many different samples. Chapter 5 provides further measurements on more samples and a theoretical model that gives good agreement with what we found.

Chapter 2

Introduction to Erbium-Doped Semiconductors

Some History of the Rare Earth Erbium

These elements perplex us in our rearches [sic], baffle us in our speculations, and haunt us in our very dreams. They stretch like an unknown sea before us—mocking, mystifying, and murmuring strange revelations and possibilities.

Sir William Crookes (February 16, 1887)

This quote refers to the atomic elements known as the rare earths (RE's) or lanthanides and may have some relevance to our "rearches" today. The RE's are the sixteen elements from yttrium (atomic number $Z=39$) and lanthanum ($Z=57$) to lutetium ($Z=71$). Promethium ($Z=61$) is a product of fission reaction, and is not found in nature, however the remaining fifteen elements generally occur together in nature [Murthy and Gupta (1980)].

An earth was considered to be an alkaline substance that did not melt upon heating, did not produce gas bubbles when reacted with acids, and which was practically insoluble in water [Trifonov (1966)]. These properties were displayed by such well known compounds as magnesium, barium and calcium oxides which were at one time considered elements and were encountered almost everywhere. The same could not be said of the yttrium and cerium earths which were discovered at the end of the 18th and beginning of the 19th centuries. The minerals in which they were contained were at first exceedingly few and were thus called the rare earths. However, investigations in this

century have shown that the RE elements are actually more abundant on the earth's surface than such well know elements as lead, mercury, and gold [Trifonov (1963)].

In the summer of 1787 Carl Axel Arrhenius, a lieutenant in the Swedish Royal Army, discovered an unknown black mineral similar to coal called yttria in an open pit mine near the small town Ytterby, Sweden, three miles from Stockholm. Because of his discovery many elements bear variations on the name Ytterby: yttrium, ytterbium, terbium, and erbium. In 1841 Carl Gustav Mosander, a Swedish chemist, extracted three earths from yttria: a yellow earth erbia, a pink earth terbia, and finally yttria itself. Some confusion arose and the names for terbia and erbia were reversed because of mistakes in the interpretation of other workers' results [Callow (1967)]. Finally, the element erbium was separated from erbia in 1879 by Swedish chemist Per Teodor Cleve [Szabadvary (1988)]. Fig. 2.1 shows the periodic table of the elements with the location of the element erbium highlighted.

Many uses for the RE elements were found starting in the late 1800's including: gas mantles, flints; cast irons; high strength steels; metal alloys; high energy permanent magnet alloys; high-temperature superconductors; fertilizer; medicines; dyes and paints; glass and ceramics; and artificial gems [Murthy and Gupta (1980); and Trifonov (1963)].

With the advent of the laser in the 1960's the interest in unique laser gain materials arose. One of the most important types of lasers is the solid state laser which often uses RE's in either a glass or a crystal such as the neodymium:yttrium-aluminum garnet or Nd:YAG laser. In fact, there are many other lasers based on the RE's that emit in

1A 1 H 1.008																	8A 2 He 4.003
3 Li 6.941	4 Be 9.012											5 B 10.81	6 C 12.01	7 N 14.01	8 O 16.00	9 F 19.00	10 Ne 20.18
11 Na 23.00	12 Mg 24.31											13 Al 26.98	14 Si 28.09	15 P 30.97	16 S 32.06	17 Cl 35.45	18 Ar 39.95
		8B										1B		2B			
19 K 39.10	20 Ca 40.08	21 Sc 44.96	22 Ti 47.90	23 V 50.94	24 Cr 52.00	25 Mn 54.94	26 Fe 55.85	27 Co 58.93	28 Ni 58.70	29 Cu 63.55	30 Zn 65.38	31 Ga 69.72	32 Ge 72.59	33 As 74.92	34 Se 78.96	35 Br 79.90	36 Kr 83.80
37 Rb 85.47	38 Sr 87.62	39 Y 88.91	40 Zr 91.22	41 Nb 92.91	42 Mo 95.94	43 Tc (98)	44 Ru 101.1	45 Rh 102.9	46 Pd 106.4	47 Ag 107.9	48 Cd 112.4	49 In 114.8	50 Sn 118.7	51 Sb 121.8	52 Te 127.6	53 I 126.9	54 Xe 131.3
55 Cs 132.9	56 Ba 137.3	57 La 138.9	72 Hf 178.5	73 Ta 180.9	74 W 183.9	75 Re 186.2	76 Os 190.2	77 Ir 192.2	78 Pt 195.1	79 Au 197.0	80 Hg 200.6	81 Tl 204.4	82 Pb 207.2	83 Bi 209.0	84 Po (209)	85 At (210)	86 Rn (222)
87 Fr (223)	88 Ra 226.0	89 Ac 227.0	104 Rf (261)	105 Ha (262)	106 Unh (263)	107 Uns (262)			109 Une (267)								
		Lanthanides															
		58 Ce 140.1	59 Pr 140.9	60 Nd 144.2	61 Pm (145)	62 Sm 150.4	63 Eu 152.0	64 Gd 157.3	65 Tb 158.9	66 Dy 162.5	67 Ho 164.9	68 Er 167.3	69 Tm 168.9	70 Yb 173.0	71 Lu 175.0		
		Actinides															
		90 Th 232.0	91 Pa 231.0	92 U 238.0	93 Np 237.0	94 Pu (244)	95 Am (243)	96 Cm (247)	97 Bk (247)	98 Cf (251)	99 Es (252)	100 Fm (257)	101 Md (258)	102 No (259)	103 Lr (260)		

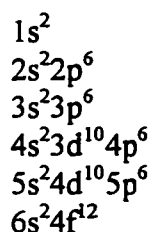
Erbium
↙

Figure 2.1 The periodic table of the elements with the lanthanides or rare earths in the second to the bottom row [Gelder (1994)].

wavelengths from 170 to 7000 nm [Payne and Krupke (1996)]. Of interest to this dissertation are light emitters using erbium.

Erbium in Semiconductors

In its metallic state, erbium has the following ground state electron configuration:



[Chang (1988)]. When erbium is introduced into semiconductor matrices, three electrons are used to form valence bonds (two electrons from the $6s^2$ shell and one from the 4f-shell). Therefore, the erbium ion exists in a three-valent Er^{3+} state with the ground $4f^{11}$ ($^4I_{15/2}$) state. The light emission at 1.54 μm arises from internal transitions in the 4f-shell of Er^{3+} from the first excited $^4I_{13/2}$ state to the ground $^4I_{15/2}$ state as is shown in Fig. 2.2.

The $^{2S+1}L_J$ notation used in the previous paragraph and in Fig. 2.2 is called the spectroscopic-term notation for the quantum numbers of a state. S is the net spin, J is the total angular momentum, and L is the net orbital angular momentum with its value indicated by an upper case letter, according to the scheme [Ohanian (1987)]:

$L =$	0	1	2	3	4	5	6	...
Letter	S	P	D	F	G	H	I	...

Radiative f-f transitions are dipole forbidden in bulk erbium but become partially allowed when RE ions are incorporated into a solid matrix. This is due to an admixture of other orbital momentum states with the f-wave function as a result of the interaction of the

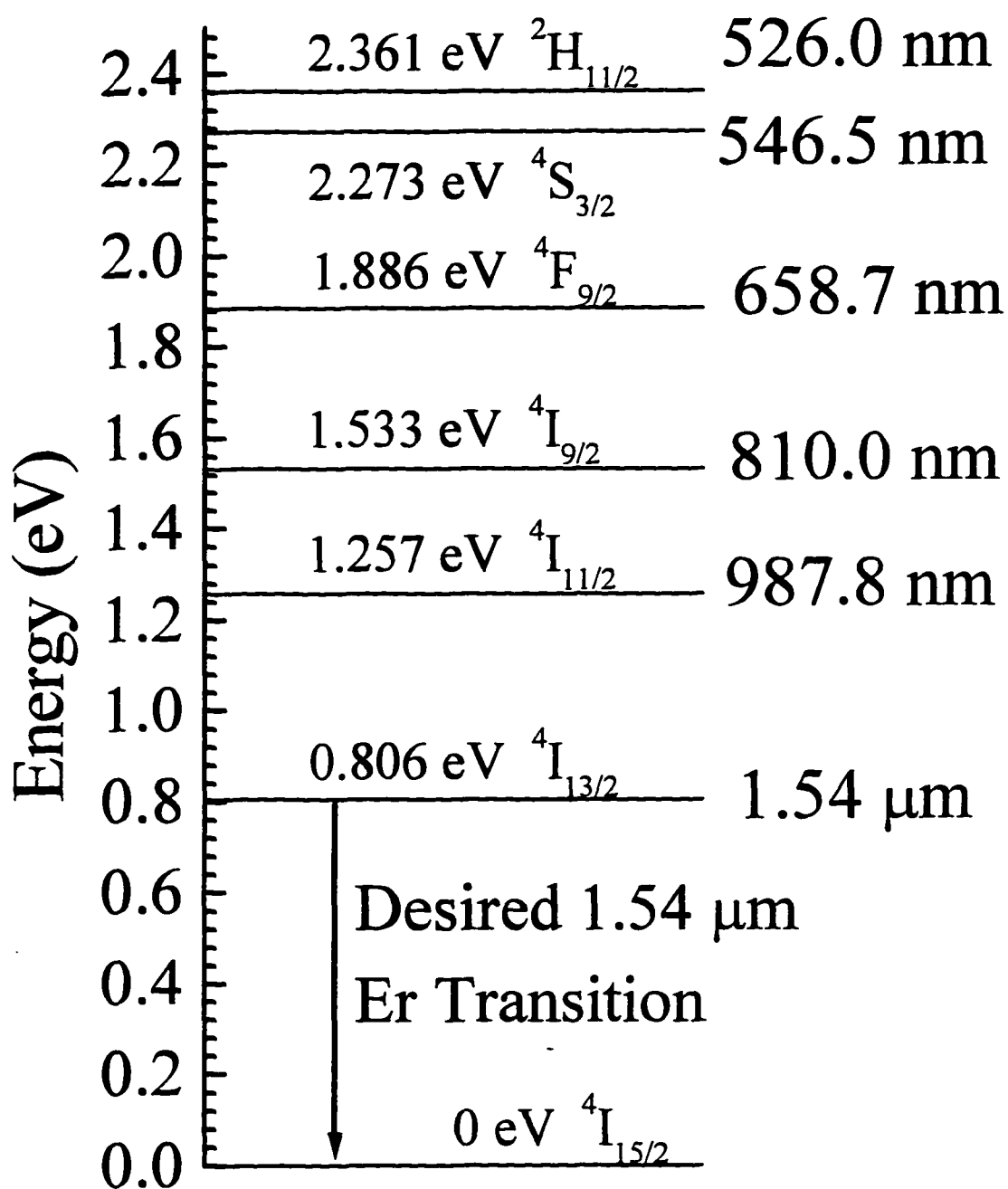


Figure 2.2 Some of the energy transitions in Er^{3+} [Dieke (1968)].

RE ion states with a crystalline field lacking an inversion center. The fact that the selection rule forbidding the f-f transitions is only partially lifted manifests itself in long lifetimes of the erbium ion in the excited state, usually about 1 ms at liquid helium temperatures.

Since the average radius of the incompletely populated 4f-shell is small, strong screening of the f-orbitals occurs because of the outer populated electronic shells with the $5s^25p^6$ configuration. Thus, the crystalline field of the semiconductor matrix has a comparatively weak effect on the f-f transitions. This leads to the almost independence of the position of the erbium luminescence lines with pump intensity, temperature, and nature of the matrix.

In the semiconductor matrix each level of the f-shell is weakly split by the crystalline field into several sublevels. Their number is determined by the point symmetry group of the crystal at the position of the RE ion. Therefore, in the luminescence spectra corresponding to transitions in the 4f-shell, several narrow lines are usually observed. The energy levels of the f-states of the RE ion are located well below the valence band edge of the semiconductor [Lanoo and Delerue (1993)].

In many cases, efficient excitation of erbium ions in semiconductor matrices occurs by Auger processes involving free or bound charge carriers [Pomrenke *et al.* (1993); Tsimperidis *et al.* (1995); Yassievich and Kimerling (1993)]. Since energy should be conserved in transitions induced by a Coulomb interaction, Auger pumping should be effective if a transition energy of the charge carriers is close to the energy difference between narrow f-levels. The excess energy released in electron transitions is transferred

to the phonon system and/or to the third particle. Electron-phonon coupling is stronger for localized states than for free carriers; therefore carriers captured by defects play an unusually more important part in the Auger excitation of RE ions.

The wider the bandgap of a semiconductor, the better, since thermal quenching of the erbium emission sets in at higher temperatures [Favennec *et al.* (1993)]. In addition, introduction of erbium ions into widegap semiconductors allows the excitation of erbium ions to higher excited states ($^4I_{11/2}$, $^4I_{9/2}$ *etc.*) resulting in a three-level system more effective for optoelectronic applications.

Light from Erbium-Doped Semiconductors

Recently there has been much interest in the luminescence of erbium ions inserted into semiconductor matrices [Coffa *et al.* (1996); Pomrenke *et al.* (1993); and Jantsch *et al.* (1996)]. This attention is caused by the well known application of RE's in laser active glasses as discussed previously and the hope of using semiconductors to achieve electrical pumping of RE centers rather than the familiar optical pumping. Erbium is especially promising because of its emission of light at 1.54 μm which corresponds to an absorption minimum of silica glass optical fibers. The insensitivity of the position of the erbium luminescence lines with temperature could be a great advantage compared to conventional laser diodes whose output wavelength can vary widely with temperature. In fact there are commercially available erbium-doped optical amplifiers that use about 3 m of doped silica fiber [Desurvire (1994)], as well as erbium-doped solid state and fiber lasers [Higgins (1995); and Kincade (1996)].

These systems are very bulky compared to a conventional laser diode which is actually a subsystem of these lasers, acting as the pump source. A much smaller system that can provide the same functionality is always desired, and that is why there is the interest in making an all-semiconductor Er light source.

Some success has been found in erbium-doped silicon (Si) by groups around the world. Priolo *et al.* (1996) have demonstrated room temperature luminescence from an electrically pumped light-emitting diode (LED) made with Er ion implantation of crystal Si with an internal quantum efficiency of 6×10^{-5} . Michel *et al.* (1996) have also reported making an electrically pumped Si LED with Er ion implantation that emits at $1.54 \mu\text{m}$. They demonstrated a CMOS (complementary metal oxide semiconductor) integrated LED operating at 120 K in an infrared free-space voice link with modulation frequencies up to 20 kHz.

Er-doped III-V semiconductors have been made by liquid phase epitaxy (LPE), ion implantation, metalorganic chemical vapor deposition (MOCVD), and MBE. Light emission of erbium has been seen at $1.54 \mu\text{m}$ at 77 K and room temperature by several research groups, but this emission has remained much weaker than conventional LED's. So there is a need to increase the transfer of energy from the optically pumped semiconductor to the Er ions. We proposed to do this by means of putting the Er ions inside of QW's via MBE and tuning the transition energy of the well, by varying the thickness and composition of the wells and barriers, to a higher energy transition of the Er. We also hoped that having the Er ions inside the QW would help with the energy transfer because of a better overlap of the wavefunctions of the ions with that of the excited

semiconductor. At first we decided to try and match the 980 transition of Er, but we had problems in making good doped InGaAs quantum wells, and although we saw emitted light at 1.54 μm , it was still weak. We then decided to try and resonate with the 810 transition of Er with GaAs wells and AlGaAs barriers. The approach we tried is pictured in Fig. 2.3. We made several samples using this design, and we discuss the results of our studies of these samples in the next chapter.

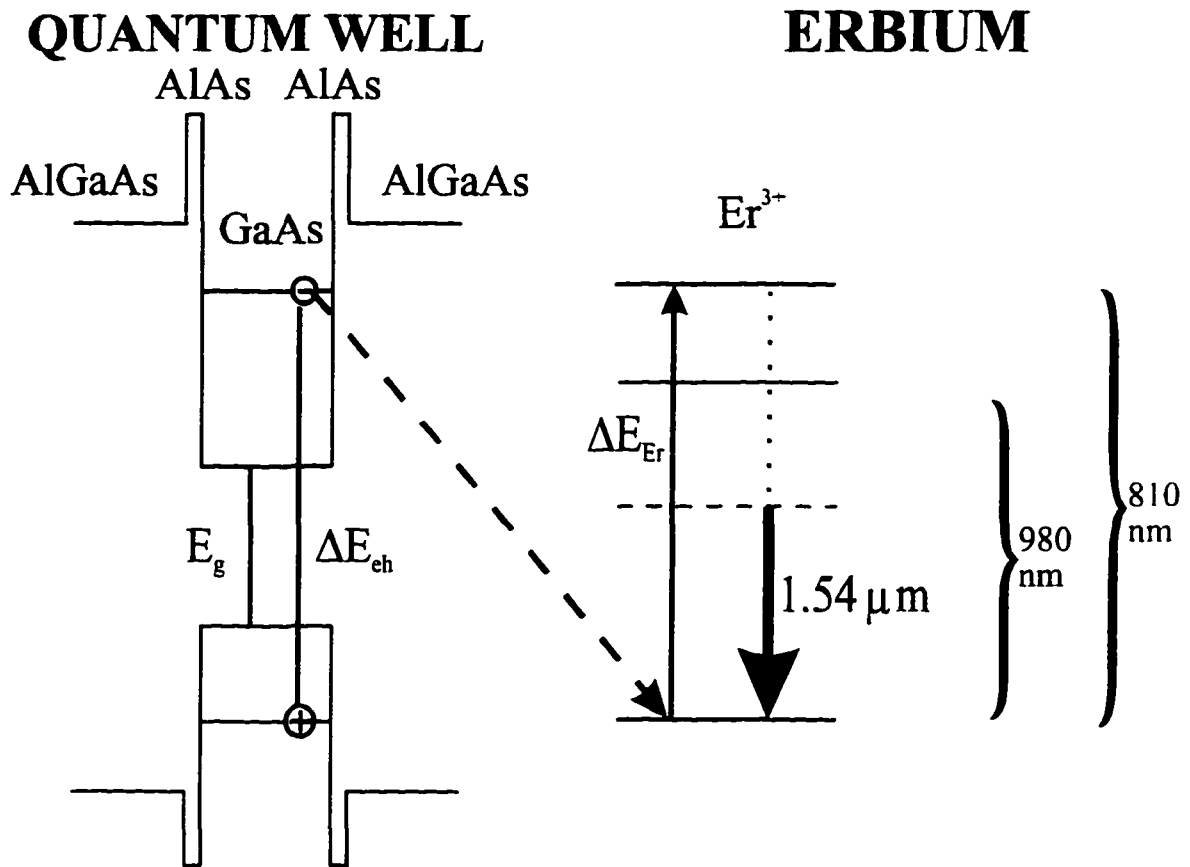


Figure 2.3 QW structure on the left used to try and match an erbium transition on the right. ΔE_{eh} is tuned to equal ΔE_{Er} by varying the thickness of the QW.

Chapter 3

Erbium Doped AlGaAs/GaAs Quantum Wells

Introduction

In this chapter we present the results of detailed studies of Er-doped GaAs/AlGaAs structures grown by MBE. Using secondary ion mass spectroscopy (SIMS) data, absorption measurements, and photoluminescence (PL) measurements, we show that the introduction of erbium into GaAs/AlGaAs quantum well structures in the process of growth by MBE leads to efficient diffusion of Er and interdiffusion of Ga and Al. In the limit of high concentrations of erbium inserted during MBE growth, we have observed the degradation of the quantum structures and practically homogeneous distribution of erbium, gallium, and aluminum over the bulk of the sample (within the measurement limits of our instruments). We show that the doping of our quantum structures with erbium leads to a formation of three defect levels in the AlGaAs bandgap and that charge carriers localized at these levels determine the processes that excite the erbium ions. We have actually succeeded in exciting erbium ions via high excited states. This process favors the development of lasers using radiative transitions in the f-shell of erbium ions inserted into semiconductor structures.

Experimental Procedure

Sample preparation

The erbium-doped structures examined here were grown in the group's Riber 32P MBE machine by Professors Galina Khitrova and Hyatt Gibbs on 625- μm GaAs substrates with a substrate temperature of $\sim 600^\circ\text{C}$. All of the samples in the Er series are described in Appendix A. The structures we label Er20 to Er23 consisted of an $\text{Al}_{0.3}\text{Ga}_{0.7}\text{As}$ etch stop layer 0.6 μm thick, then 50 quantum wells each consisting of a 10 nm GaAs:Er well and 21 nm AlGaAs barriers with the Er cell temperature at 450°C (and shutter closed), 900°C , 870°C , and 930°C , respectively (variation of the temperature of the erbium cell changes the erbium concentration). In all the samples there were also 0.9 nm AlAs spikes at each end of the barriers separating the GaAs:Er and AlGaAs. On top of the 50 QW's there was another identical 0.6 μm AlGaAs window to symmetrize the strain. Finally about 7 nm of GaAs was grown on top to prevent the AlGaAs from oxidizing. This QW structure is schematically shown in Fig. 3.1.

The structure Er26 consisted of 8 nm GaAs:Er (900°C) layers separated by 22 nm of undoped GaAs repeated 50 times with 300 nm of GaAs on top. Er25 and Er34 are like Er20 except that they have no AlAs spikes. They also vary from Er20 in that Er25 had Er (900°C) in the GaAs well only and Er34 in the AlGaAs barrier only. Sample Er29 consisted of Er (900°C) homogeneously doped into 1.7 μm of $\text{Al}_{0.3}\text{Ga}_{0.7}\text{As}$. The Er concentrations measured by SIMS of these samples are presented in Table 3.1.

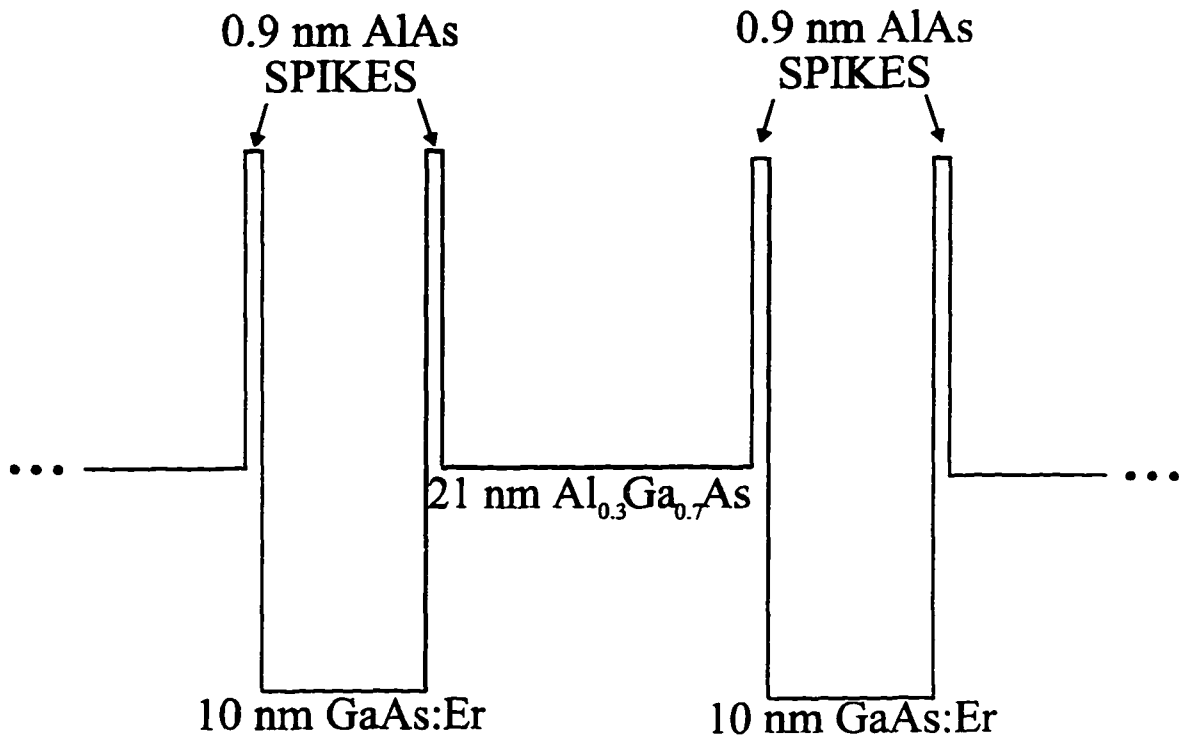


Figure 3.1 Conduction band structure for Er20, 21, 22, and 23.

The dependence of the erbium concentration on the temperature of the source during growth (deduced from our measurements) can be summarized approximately by the formula:

$$N_{Er} = N \exp\left(-\frac{E_b}{\kappa T}\right) \quad (3.1)$$

where $N = 2.85 \times 10^{34} \text{ cm}^{-3}$ and $E_b = 3.6 \text{ eV}$ which is similar to the activation energy $E_b = 3.3 \text{ eV}$ of erbium evaporation from the metal source (see Fig. 3.2).

Experimental measurements

SIMS measurements were made at the facilities in St. Petersburg and gave a depth resolution of 5 nm. Low temperature (1.8K) photoluminescence spectra of the structures

Sample number	Temperature of erbium source (°C)	Erbium concentration from SIMS (cm ⁻³)	Comments
Er20	No erbium		
Er21	900	9×10^{18}	Er in QW
Er22	870	3×10^{18}	Er in QW
Er23	930	2.2×10^{19}	Er in QW
Er25	900	7×10^{18}	Er in QW
Er26	900	4×10^{18}	GaAs:Er
Er29	900	9×10^{18}	AlGaAs:Er
Er34	900	6×10^{18}	Er in barrier

Table 3.1. Erbium concentrations, determined by SIMS, of the grown structures

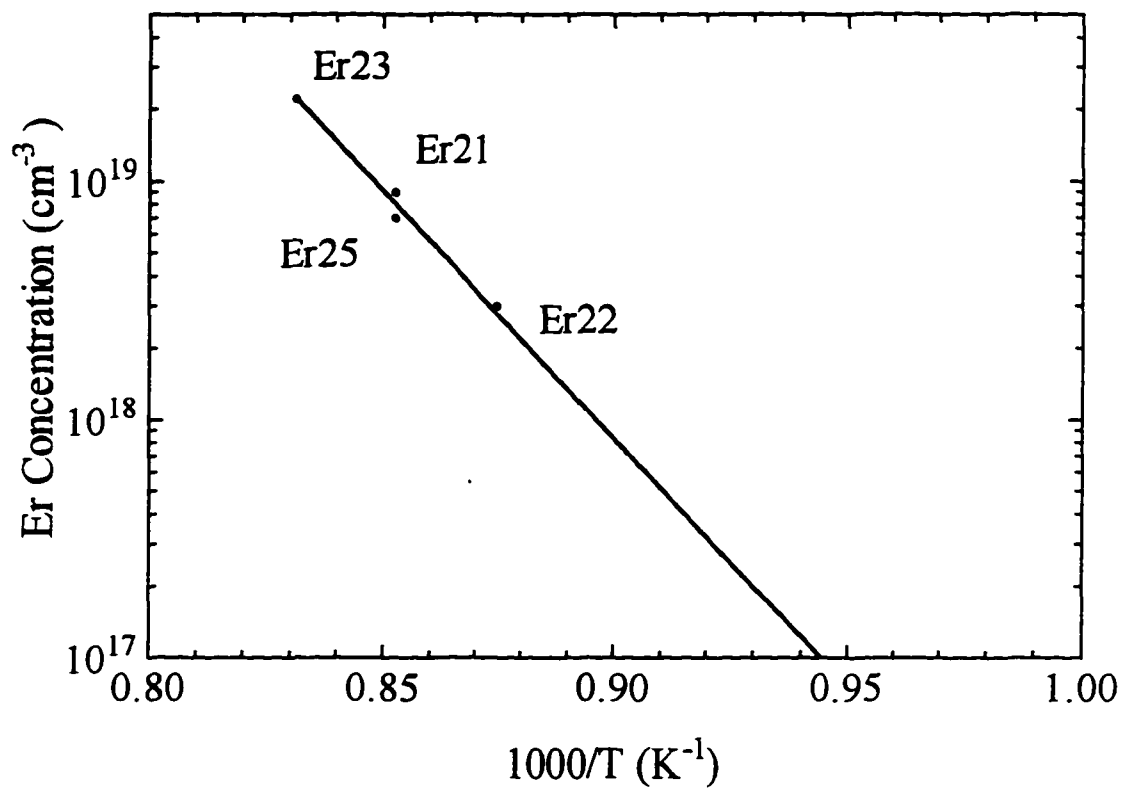


Figure 3.2 Erbium concentration as a function of Er cell temperature.

were measured immersed in liquid helium. The spectra were analyzed with an 822 mm double grating spectrometer and detected by a liquid-nitrogen-cooled germanium photodetector. Excitation was provided by an argon cw laser using the 488 nm line with pump powers up to 40 mW. PL lifetimes were determined by a phase shift method in which a phase sensitive detector was used to measure the phase difference between the PL and pump light signals.

Absorption spectra of the structures were performed with the GaAs substrate chemically etched away to prevent absorption of the transmitted light that was below the bandedge of GaAs. The techniques that we used to accomplish this etching are described by LePore (1981). The spectra were measured with the samples at 4K in a liquid-helium open-cycle cryostat and were resolved by a 1/8th meter scanning spectrometer and detected by a liquid nitrogen-cooled germanium photodiode. This setup is shown in Fig. 3.3.

Temperature dependencies of the intensities of different spectral lines were studied using two slightly different measurement setups, one in transmission and the other in reflection. Both setups used a closed-cycle helium cryostat with temperature control from 10K to above room temperature. Excitation was provided by an argon cw laser running on multiple lines with pump powers up to 100 mW. This laser beam was modulated by a chopper blade rotating at ~22 Hz. This slow speed was necessary because of the long lifetime of the erbium PL. The spectra were resolved in a scanning 3/4 m spectrometer with a liquid-nitrogen-cooled germanium photodiode at the output slit. The electrical output of the detector was sent to a preamplifier and then to a lock-in amplifier

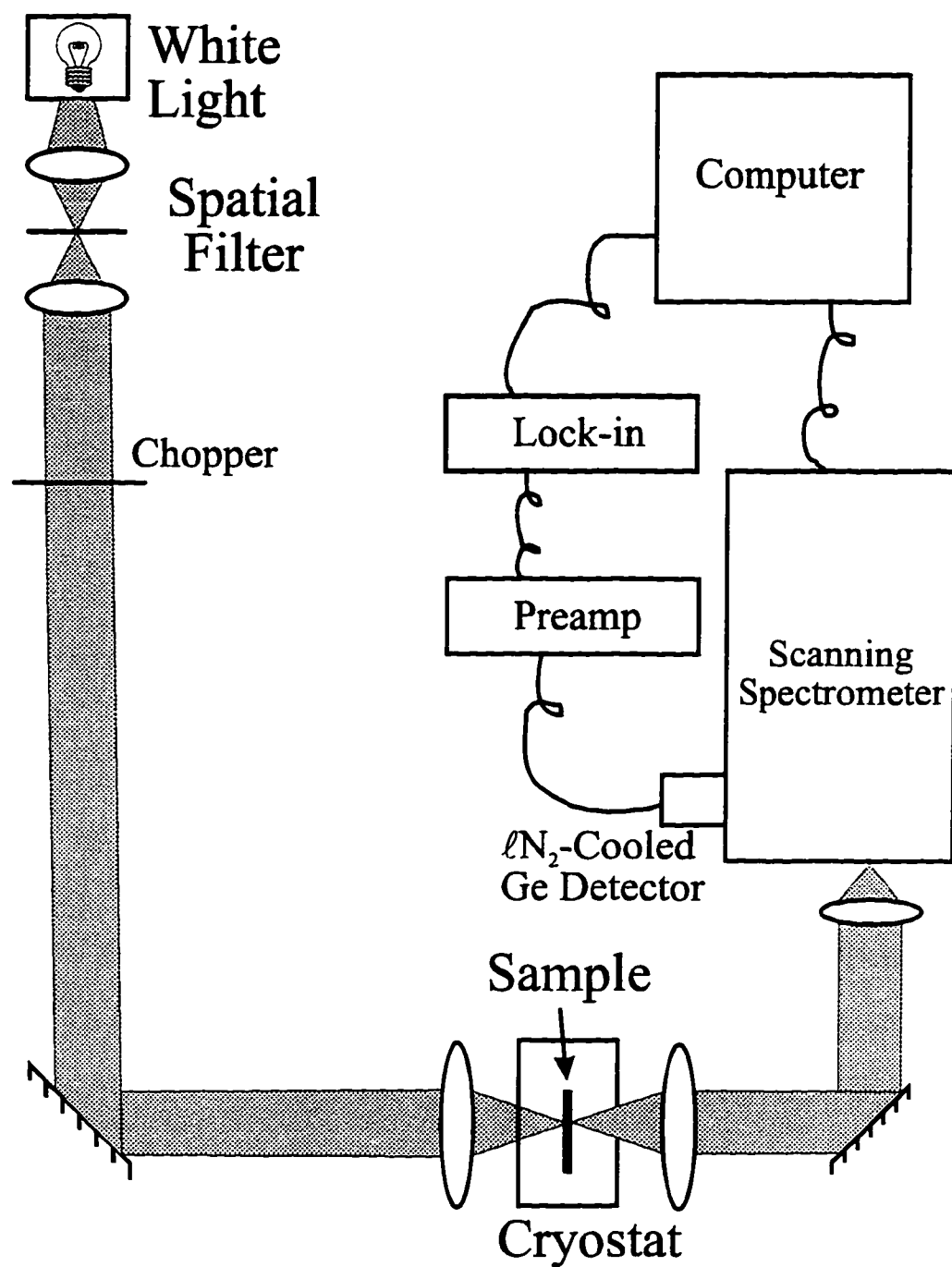


Figure 3.3 Absorption measurement setup.

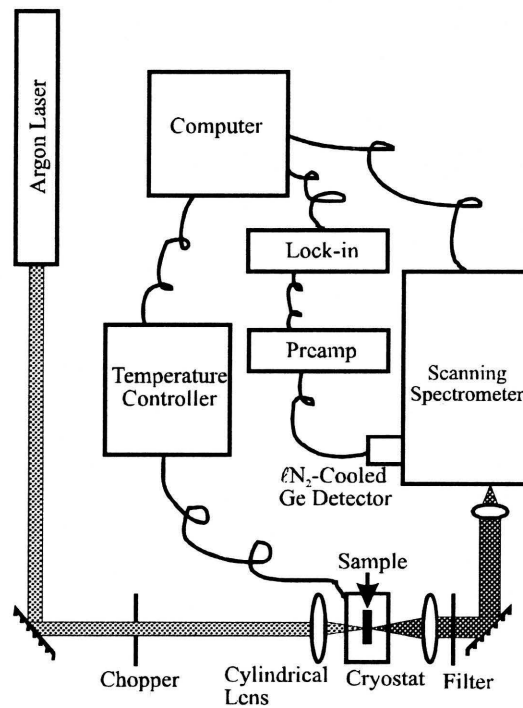
where the PL signal was extracted. Various colored filters were placed in the PL beam to prevent any laser light from entering the spectrometer, as well as to prevent any second order light from the spectrometer's grating giving false results.

The temperature controller, spectrometer, and lock-in amplifier were all interfaced to a computer program that allowed the taking of multiple spectra scans at different temperatures. To reduce the noise of the weaker signals, many scans at the same temperature were added together. Some of the temperature data series presented here took more than a non-interrupted 24-hour period to complete. The only restriction on the length of the measurement was determined by the need of refilling the liquid-nitrogen dewar of the photodiode every seven hours. This measurement time could be extended by pausing the measurement program, refilling the nitrogen, and then continuing.

Because the PL from the Er in our samples remained weak, many different strategies were tried to increase the measured signal. We finally used a cylindrical focusing lens for the argon pump laser to create a linear focus on the input slit of the spectrometer rather than a spot. Collecting the PL from the polished back side of the sample was then needed to gather as much light as possible to send into the spectrometer. This required the transmission type geometry that is pictured in Fig. 3.4a.

For all of the PL-versus-temperature measurements we left the substrate on to reduce heating. When we needed to look at PL that was below the bandedge of GaAs we used the reflection geometry shown in Fig. 3.4b. Reflection was required because, in the transmission geometry, all of the light of interest would have been absorbed by the GaAs substrate.

a) Transmission PL Setup



b) Reflected PL Setup

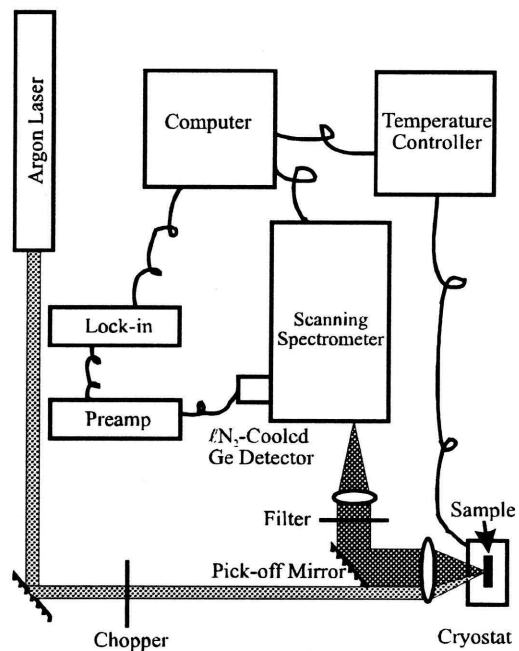


Figure 3.4 Temperature dependent PL measurement setups for a) transmission geometry and b) reflection geometry.

Experimental Results

Er-induced Ga-Al interdiffusion and Er diffusion

The SIMS profile for the Er26 sample (GaAs:Er), shown in Fig. 3.5, shows a concentration of $4 \times 10^{18} \text{ cm}^{-3}$ completely independent of position, contrary to opening and closing of the Er shutter during growth. It is clear that no erbium layers exist in the structure; complete leveling of the erbium concentration occurred indicating a high diffusion coefficient of erbium in bulk GaAs grown by MBE in contrast to the case of introduction of erbium by diffusion techniques.

In Fig. 3.6 the SIMS profiles are presented for three samples in the order of increasing erbium concentration which was introduced only into the GaAs QW layers. While for Er20 (no Er) distinct QW's are seen in the SIMS picture, for Er21 they are less pronounced, and in Er23 QW's are no longer seen with our SIMS resolution. In Er23 ($N_{\text{Er}} = 2.2 \times 10^{19} \text{ cm}^{-3}$) no SIMS modulation is seen for either Ga, Al or Er. Thus, the interdiffusion of gallium and aluminum and diffusion of erbium depends directly on the concentration of erbium ions. Since SIMS has a limited spatial resolution there is also the possibility that Er causes the growth to become so wavy or rough that no modulation of the average density is seen even though QW's still exist to some extent. However, PL spectra independently indicate that the Er and Al end up together.

In Fig. 3.7a the PL spectrum of the Er26 sample is presented in the spectral region of erbium PL (1.5 - 1.6 μm). This sample is erbium-doped bulk GaAs, erbium being inserted into the semiconductor during MBE growth of the GaAs layer every 8 nm

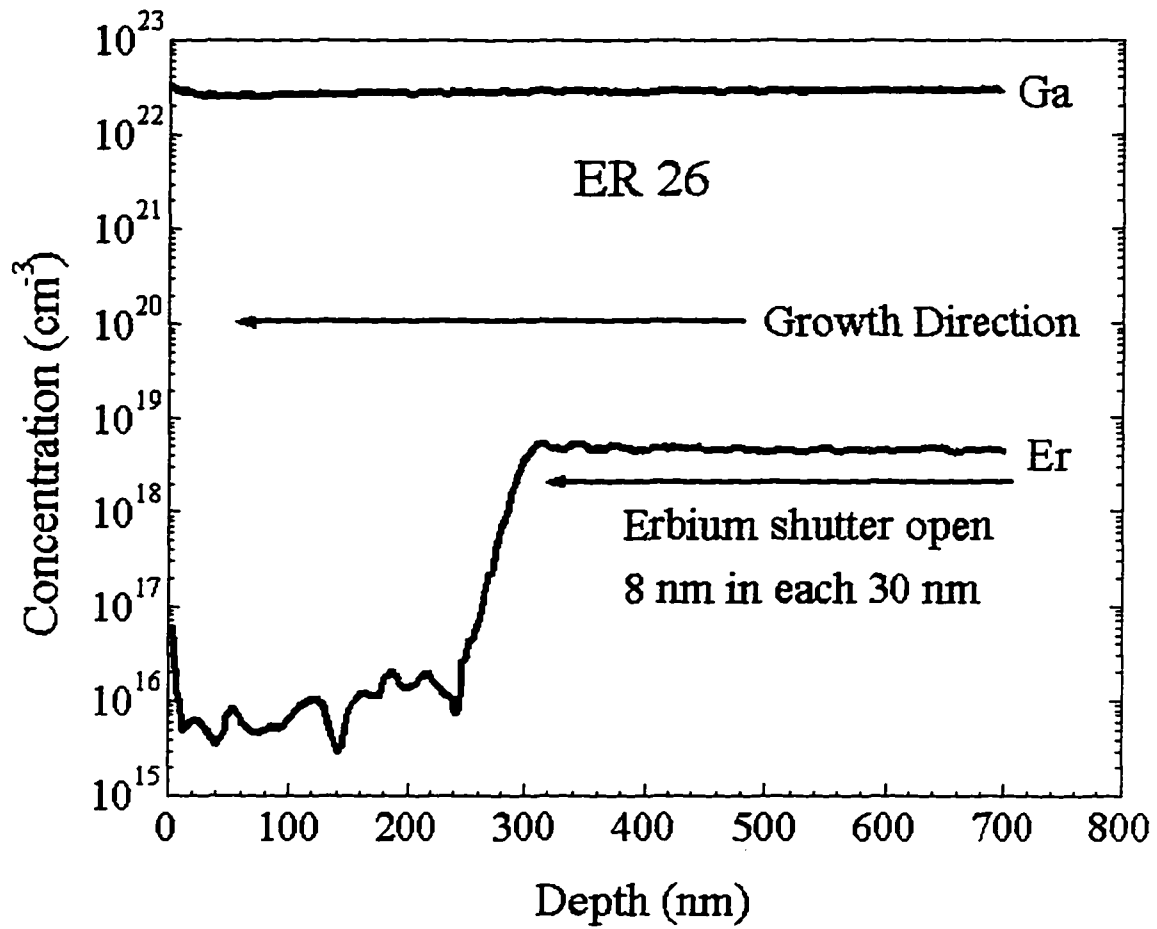


Figure 3.5 SIMS profile for Er26.

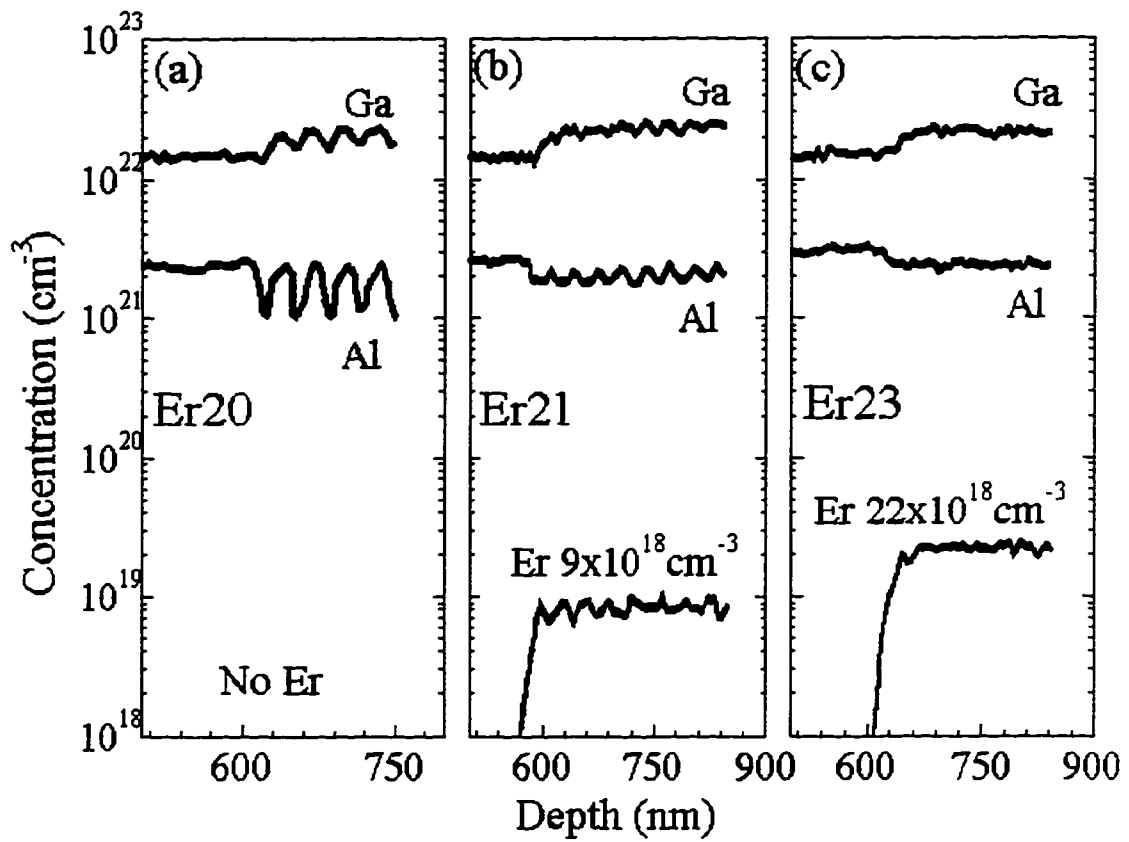


Figure 3.6 SIMS profiles for a) Er 20, b) Er21, and c) Er23.

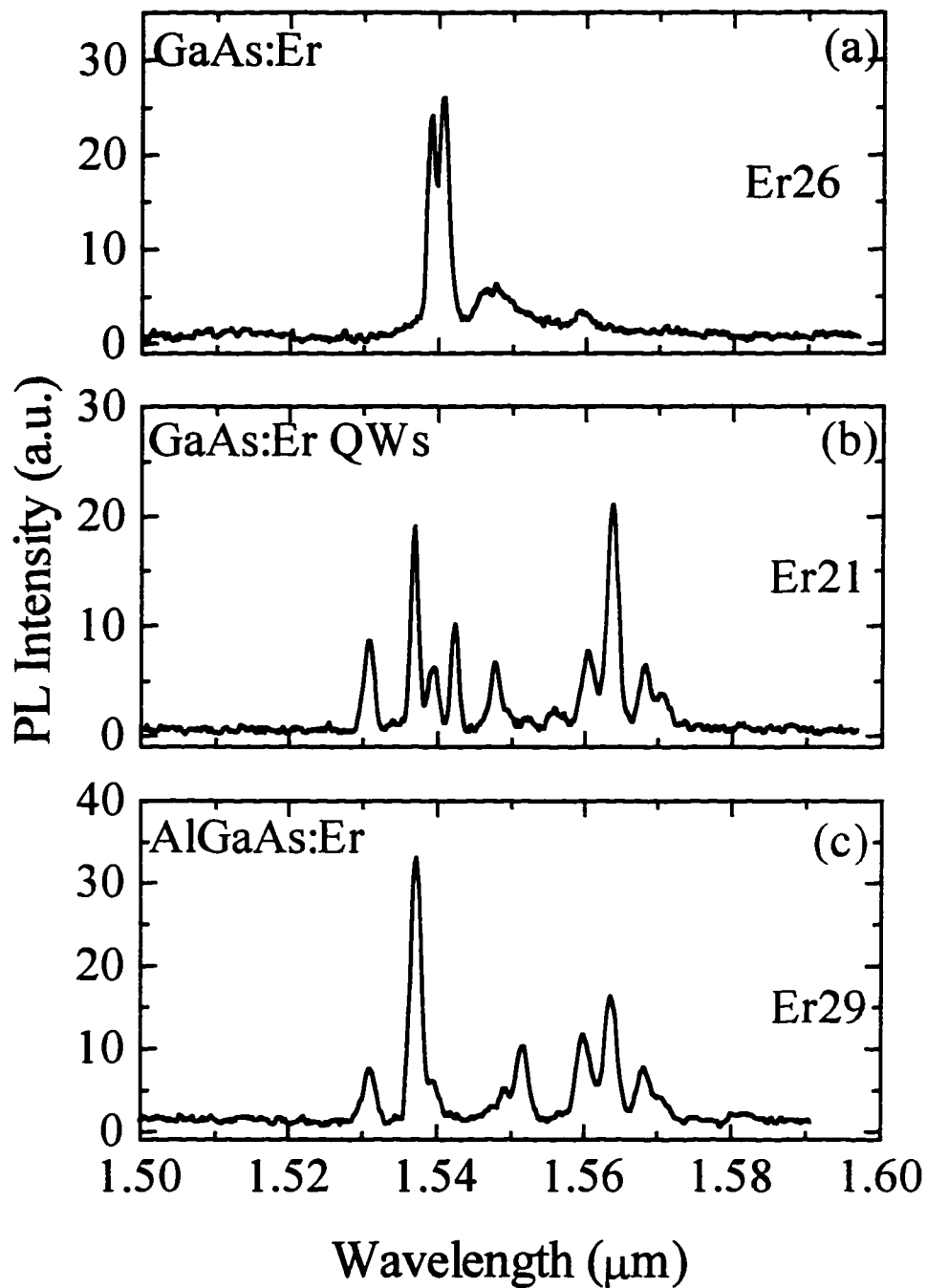


Figure 3.7 High resolution PL spectra of a) Er26, b) Er21, and c) Er29.

in each 30 nm. The positions of erbium PL lines corresponding to the $^4I_{13/2} \rightarrow ^4I_{15/2}$ transition in the f-shell of the erbium ion are in good agreement with the literature data for GaAs without additional doping [Elsaesser *et al.* (1993)].

In Fig. 3.7b the PL spectrum of the Er21 sample is shown. In this case erbium was introduced into the QW's only (into GaAs). Obviously this spectrum differs significantly from the GaAs:Er PL spectrum, but strongly resembles the PL spectrum of the Er29 sample (Fig. 3.7c) where erbium was introduced into bulk AlGaAs (PL of MBE-grown Er-doped $Al_xGa_{1-x}As$ was first observed by Zhang *et al.* (1993)). This point corroborates the previously drawn conclusion that upon the introduction of erbium into the GaAs QW's only, interdiffusion of gallium and aluminum takes place.

There seems to exist an interaction between erbium and aluminum ions that drives erbium into aluminum-rich regions and aluminum into the erbium-doped part of the structure. The evidence for erbium's preference to have an Al environment instead of a Ga environment can be seen by comparing the SIMS of Er21 (Al spikes around GaAs:Er well, showing weak Er SIMS modulation), Er25 (no AlAs spikes between AlGaAs barriers and GaAs:Er well, showing no Er SIMS modulation), and Er34 (no AlAs spikes between AlGaAs:Er barriers and GaAs well, showing stronger Er SIMS modulation) shown in Figs. 3.6b and 3.8. Qualitatively this shows that if the Er is placed in AlGaAs, it does not leave it to go into GaAs; if placed in GaAs, some of it ends up in AlGaAs also. These data show that Er binds more strongly to Al than Ga.

The absorption spectra of Fig. 3.9 give further support to the picture of an erbium-aluminum interaction. The spectrum of Er20 clearly shows the 2-dimensional staircase-

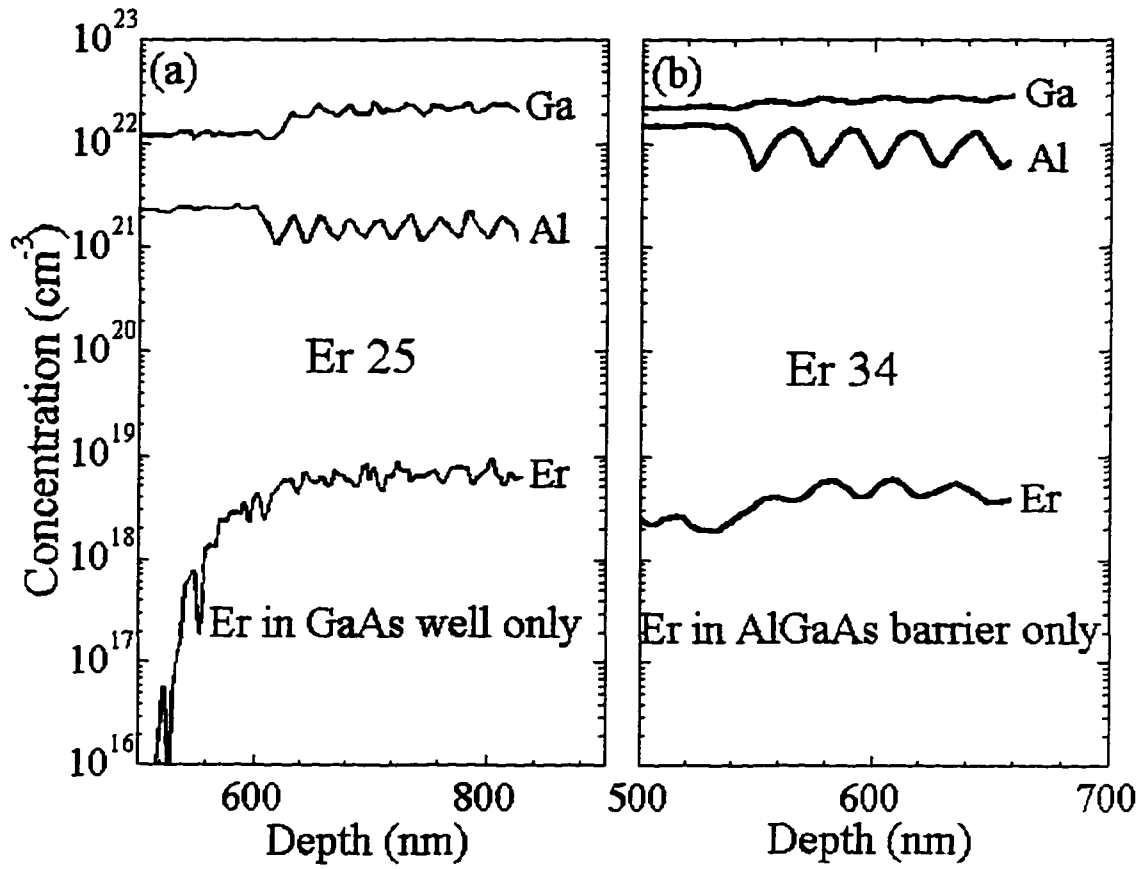


Figure 3.8 SIMS profiles for a) Er25 and b) Er34.

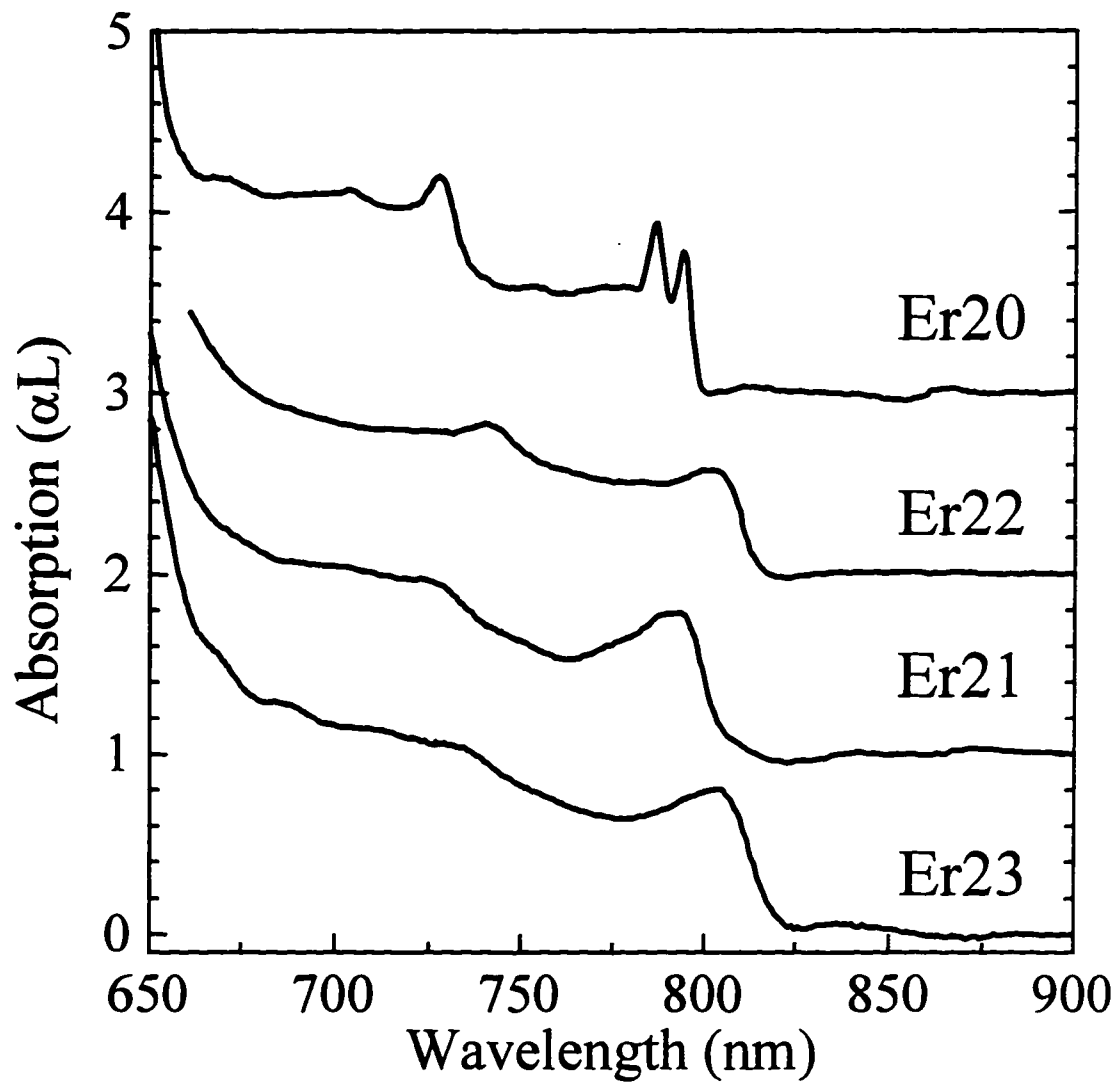


Figure 3.9 Absorption spectra for Er20, Er22, Er21, and Er23. Curves are separated vertically by 1.0 for clarity.

like density of states for $n = 1, 2$. As the erbium concentration increases in Er22 and Er21, the staircase absorption becomes less apparent. In Er23, which has the highest erbium concentration, the absorption begins to follow the 3-dimensional density of states, close to that of bulk GaAs, but slightly higher in bandgap. This is consistent with Er-Al clusters in almost bulk GaAs, rather than $\text{Al}_{0.25}\text{Ga}_{0.75}\text{As}$ which would result from a homogeneous interdiffusion of the Al. If Al diffusion into the GaAs wells did not form clusters, the band edge energy would go up dramatically with Al concentration but Fig. 3.9 shows it does not.

Further evidence for an Er-Al interaction comes from the PL spectra of Fig. 3.7. As observed earlier, even though Er was introduced only into the GaAs layers in structure Er21, the Er PL spectrum at $1.54 \mu\text{m}$ (Fig. 3.7b) is characteristic of AlGaAs (Fig. 3.7c) which is much more complex than that of Er in GaAs (Fig. 3.7a). It should be noted that we have observed erbium PL spectra resembling the spectra of AlGaAs:Er even in the samples with very small erbium concentrations ($< 10^{17} \text{ cm}^{-3}$) inserted into the GaAs QW's so that the quantum well structure was well preserved. These facts clearly indicate an Al-Er interaction.

The phenomenon of impurity-induced layer disordering during the doping of structures with electrically active impurities (donors or acceptors) is well known in the technology of GaAs/AlGaAs quantum structures and has been extensively studied [Deppe and Holonyak (1988); and Laidig *et al.* (1981)]. This phenomenon is connected with the Fermi-level dependence of the formation of excess lattice vacancies or interstitials in the semiconductor crystal lattice which in turn control the disordering [Deppe and Holonyak

(1988)]. However, it is believed that the predominant position of Er^{3+} ions in the crystal lattice of a III-V semiconductor is the substitutional cation position [Taguchi and Ohno (1995)]. In this case, erbium behaves as an isovalent impurity, i.e. it does not supply (or trap) an additional charge. Therefore we cannot expect that the concentration of erbium ions will influence directly the Fermi level position of the semiconductor, and the explanation of high diffusion coefficients discussed in Deppe and Holonyak (1988) cannot be applied to our results. It should be noted that in our case impurity-induced layer disordering due to the interdiffusion of Ga and Al is observed at a substrate temperature lower by 100-200 K compared to the studies described in Deppe and Holonyak (1988).

The strong diffusion of erbium and interdiffusion of gallium and aluminum may be due to the large difference between the ionic radii of Er and the Ga and Al cations. Er^{3+} has a radius of 0.881 Å, while the ions of Ga and Al have radii of 0.62 Å and 0.51 Å respectively [Weast (1974)]. This difference leads to the formation of a significant number of additional cation vacancies and a corresponding increase in the diffusion coefficients of the cations. It is known that the local shear strain induced by the introduction of impurities reduces the energy of the formation of vacancies in the vicinity of an alien atom. This reduction is stronger the greater the difference between the ionic radii of the alien and host ions [Boltaks (1972); and Frenkel (1955)].

The diffusion coefficient is small when erbium is introduced into GaAs by diffusion because the radius of the erbium ion is larger than the gallium radius. The diffusion coefficient of impurities depends also on the concentration of cation or anion vacancies, but since the concentration of vacancies in the equilibrium condition is constant at

constant temperature, it is the size of the impurity atom that determines the diffusion rate. The situation is different in the case when the vacancies are created in the process of growth, and this is what happens in the MBE growth of Er-doped GaAs/AlGaAs structures. As shown in Alves *et al.* (1993) in the case of $\text{Al}_{0.5}\text{Ga}_{0.5}\text{As}$ prepared by MBE for concentrations up to 10^{18} cm^{-3} , 88 percent of erbium ions occupy substitutional positions (the cation site). For higher erbium concentration the fraction of erbium ions in interstitial positions increases, and for $N_{\text{Er}} = 5 \times 10^{19} \text{ cm}^{-3}$ only 30 percent of erbium is in substitutional positions. (Still we can expect that the deformation induced by an erbium ion in the interstitial position is even larger).

The tendency of erbium to have aluminum nearby is probably due to their chemical interaction since it is known that there exists several intermetallic compounds of erbium and aluminum [Wallace (1973)]. On these grounds we can expect the formation of different erbium-aluminum complexes in our samples.

Er- photoluminescence and defects induced by Er

The PL spectrum of the Er21 sample consists of some ten lines. However, having compared the spectra measured at $T = 5 \text{ K}$ and $T = 40 \text{ K}$ (Fig. 3.10) we have observed a sharp difference in the behavior of the intensities of the lines. Some of the lines have dramatically decreased in intensity with increased temperature while others have had almost no change in intensity. We have determined that there are three series of these lines (*a*, *b*, and *c*) according to their temperature quenching.

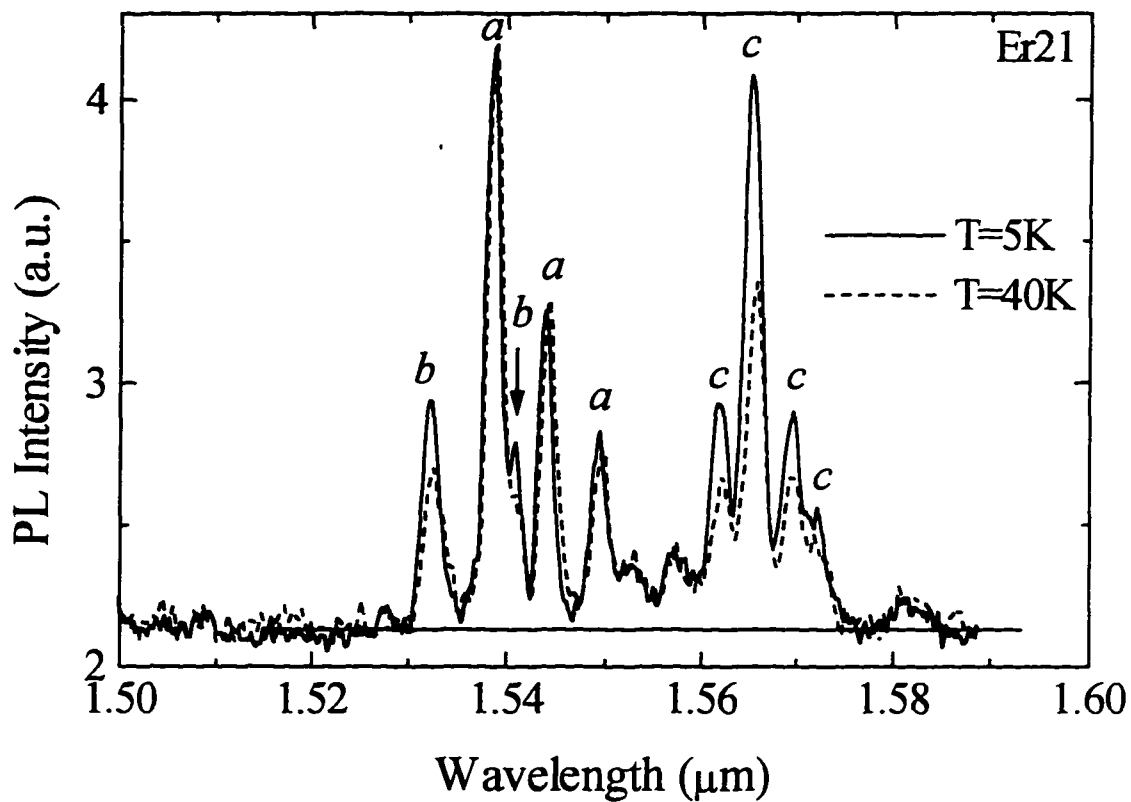


Figure 3.10 High resolution PL spectra of Er21 at $T_1=5\text{K}$ (solid line) and $T_2 = 40\text{K}$ (dashed line).

Our measurements of the lifetimes of the erbium ions in the excited state have demonstrated that the lifetime corresponding to the a line was about 0.5 ms while those for the b and c lines were only 0.05-0.07 ms.

In Fig. 3.11 the PL spectra of two samples with two different concentrations of erbium inserted into their QW's are shown. It is clear that besides the differences in temperature dependence and lifetimes, the a , b , and c series of lines differ also by their linewidths. The linewidths of the b and c series are 15 Å while those in the a series are less than 7 Å. Also, the ratio of the intensities within each series is constant and independent of the concentration of erbium inserted into the GaAs QW's.

Thus, from the temperature quenching, lifetimes, linewidths of the PL, and the ratios of the lines' intensities in each series we have concluded that the introduction of erbium into AlGaAs leads to the formation of three groups of erbium centers. We propose that the existence of these centers is accompanied by an appearance of three defect levels in the semiconductor bandgap involved in the Auger excitation of the erbium ions. We have labeled these defect levels as Da , Db , and Dc . It follows from the temperature dependence measurements that Da is a deep level while Db and Dc are shallow ones.

It is known that the introduction of erbium into a GaAs semiconductor matrix induces the appearance of an impurity potential in the crystal lattice [Elsaesser *et al.* (1995)]. The nature of this isovalent impurity potential is determined both by a difference in the internal (short-range) potentials of the matrix atom and by a difference in their atomic sizes. However, it is generally believed that the differences of the atomic radii

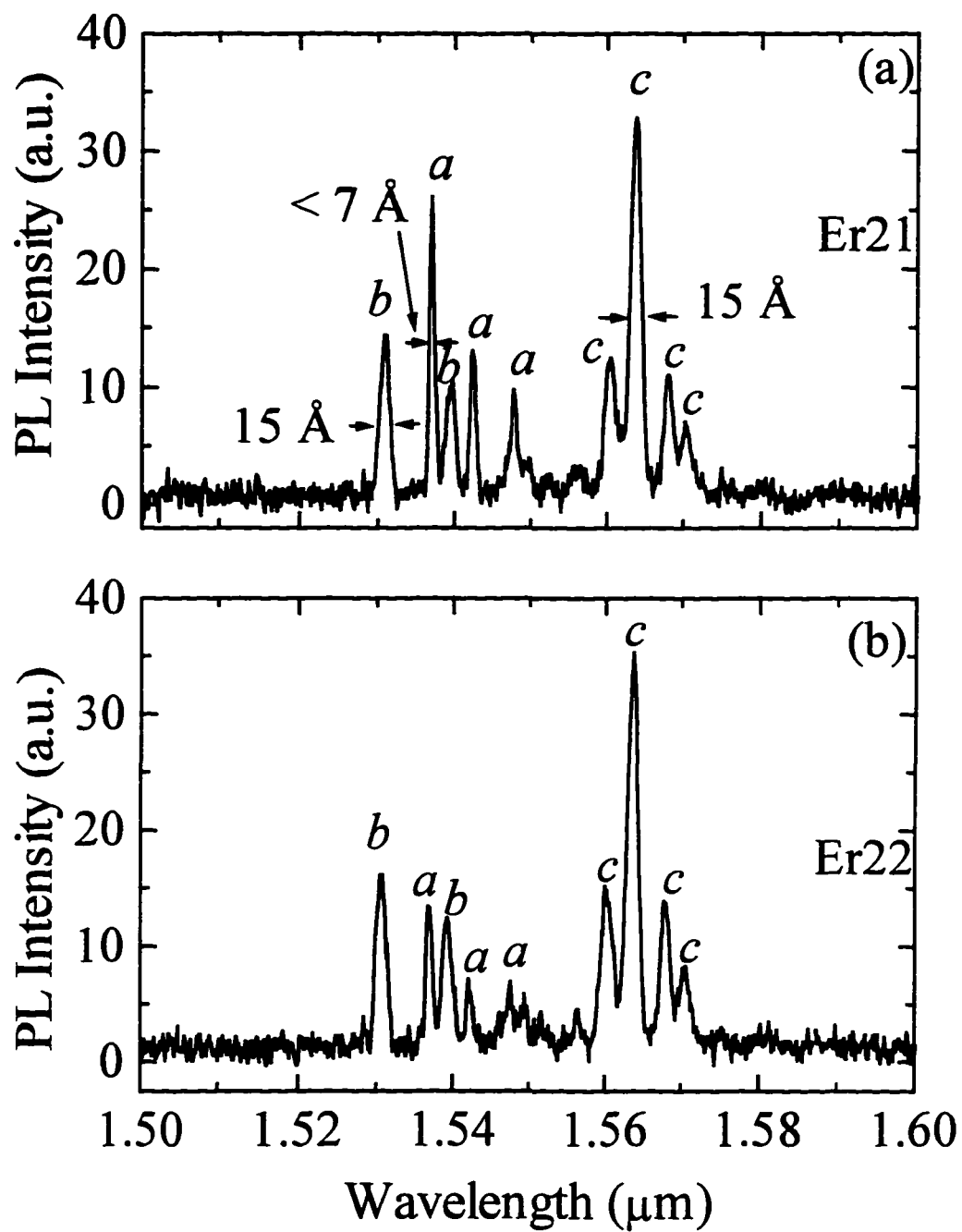


Figure 3.11 High resolution PL spectra taken at 1.8 K of a) Er21 and b) Er22.

predominates. This fact leads to shear deformation of the lattice resulting in the splitting of the degenerate GaAs valence band. As a result, a potential that attracts holes appears. The origin of the shallow hole trap, with a binding energy of 35 meV in GaAs, which is induced by an introduction of erbium is presumably due to just this reason. If the erbium concentration exceeds $5 \times 10^{17} \text{ cm}^{-3}$ (the limiting solubility of erbium in GaAs), erbium begins to occupy interstitial positions within the crystal which leads to a formation of a deep defect hole trap with an energy of 350 meV [Elsaesser *et al.* (1993); Elsaesser *et al.* (1995); and Taguchi and Ohno (1995)].

We assume that similar hole traps should also be formed in AlGaAs upon the introduction of erbium, and that their binding energies should be close to those observed in GaAs. In fact, we have found two defect PL lines in the 640-680 nm range at high pump rates, when the intrinsic erbium PL tends towards saturation (Figs. 3.12 and 3.13).

In the spectrum of Fig. 3.12 we can see two fairly wide lines with maxima at $Db = 1.87 \text{ eV}$ and $Dc = 1.90 \text{ eV}$ and a narrow exciton line at $Ex = 1.92 \text{ eV}$. Using similar reasoning as in the case of GaAs, we can assume that erbium ions in the substitutional positions in AlGaAs induce two shallow defect-levels with binding energies of 20 and 50 meV (calculated from the differences in the positions of the exciton line Ex and the defect PL lines Db and Dc). The existence of two types of shallow traps in AlGaAs instead of only one in GaAs is probably due to the different surroundings of erbium ions in the AlGaAs matrix. It should be noted that we cannot ascribe these defect states unambiguously to hole traps. This point actually requires further study.

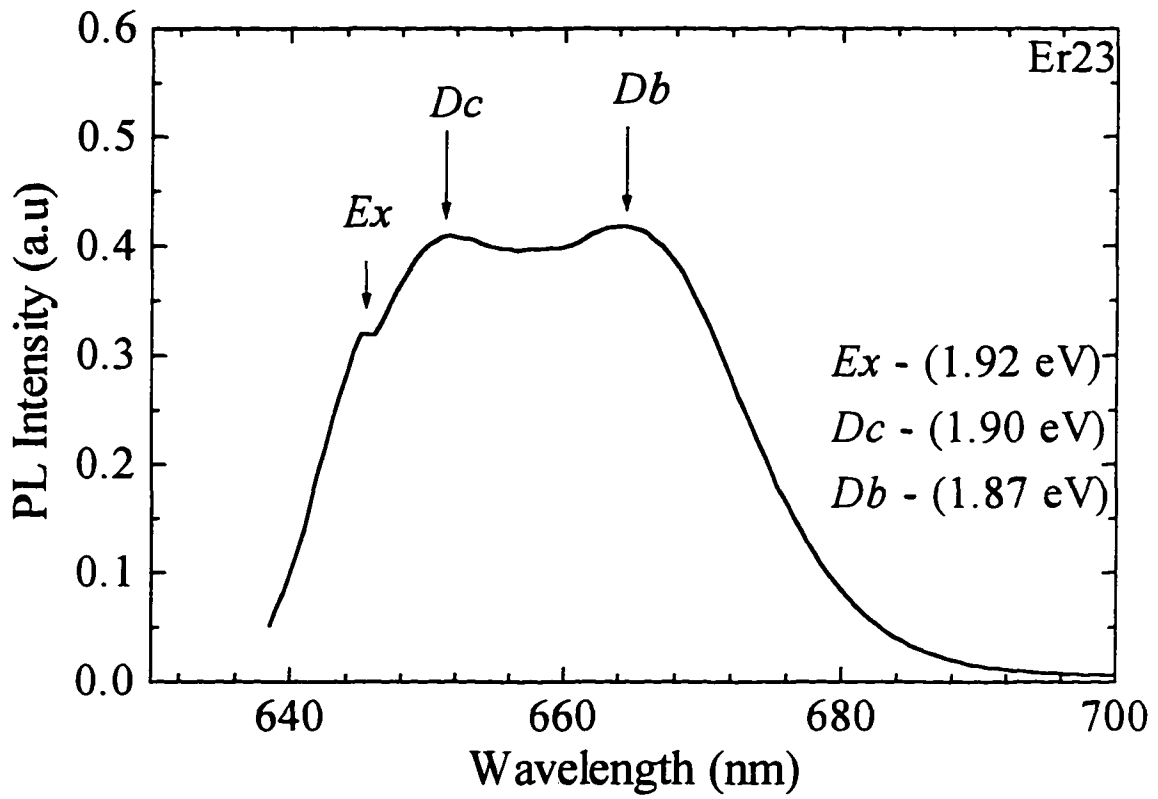


Figure 3.12 PL spectrum of Er23 taken at 10.5 K demonstrating the presence of shallow defect states in Er-doped GaAs/AlGaAs.

The results of temperature quenching studies of the *Db* and *Dc* defect lines and *a*, *b*, and *c* erbium series are given in Figs. 3.13, 3.14, and 3.15. The quenching of the defect *Dc* line is significantly stronger than that of the *Db* line (Fig. 3.13). The activation energy of 65 meV found from the temperature dependence of the *Db* line (Fig. 3.15a) is in fair agreement with the binding energy of the *Db* level deduced from the PL data: $1.92 - 1.87 = 0.05$ eV. The temperature quenching of the erbium PL *c* line occurs with an activation energy of 25 meV (Fig. 3.15a) corresponding to the binding energy of the *Dc* level found from the PL data: $1.92 - 1.90 = 0.02$ eV.

Thus, the quenching of the erbium PL connected with the most shallow trap *Dc* is controlled by depopulation of this state with rising temperature. As can be seen from Figs. 3.15a and 3.15b, the temperature quenching of the *b* and *a* lines of the erbium PL is weaker than that of the *c* line. The effective drop of the line *a* intensity starts only at about 50 K for Er23, and starts at above ~ 100 K for Er29 (AlGaAs). The line *a* can be observed practically up to room temperature. Note, that the temperature quenching of the *b* and *a* lines occurs earlier than we should expect from depopulation of the corresponding defect levels.

It should be noted that the position of the exciton line at $E_x = 1.92$ eV corresponds to the composition of the alloy $\text{Al}_x\text{Ga}_{1-x}\text{As}$ with $x = 0.32$. However, as we stated earlier, the average composition of $\text{Al}_x\text{Ga}_{1-x}\text{As}$ that would be obtained as a result of the complete leveling of the gallium and aluminum concentrations over the QW region due to cation interdiffusion could not exceed $x = 0.25$. This difference also indicates that there exist erbium-containing clusters enriched by aluminum.

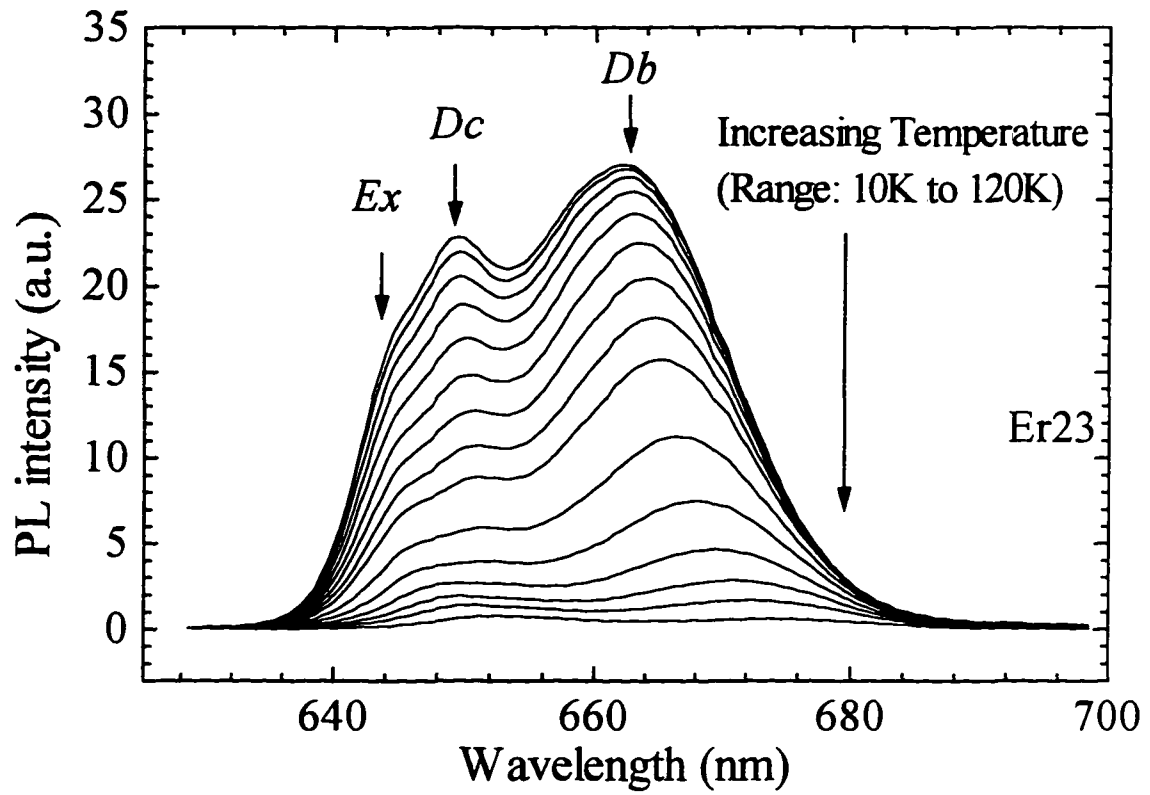


Figure 3.13 Temperature evolution of the PL spectra of Er23 demonstrating the temperature quenching of the *Db* and *Dc* defect lines.

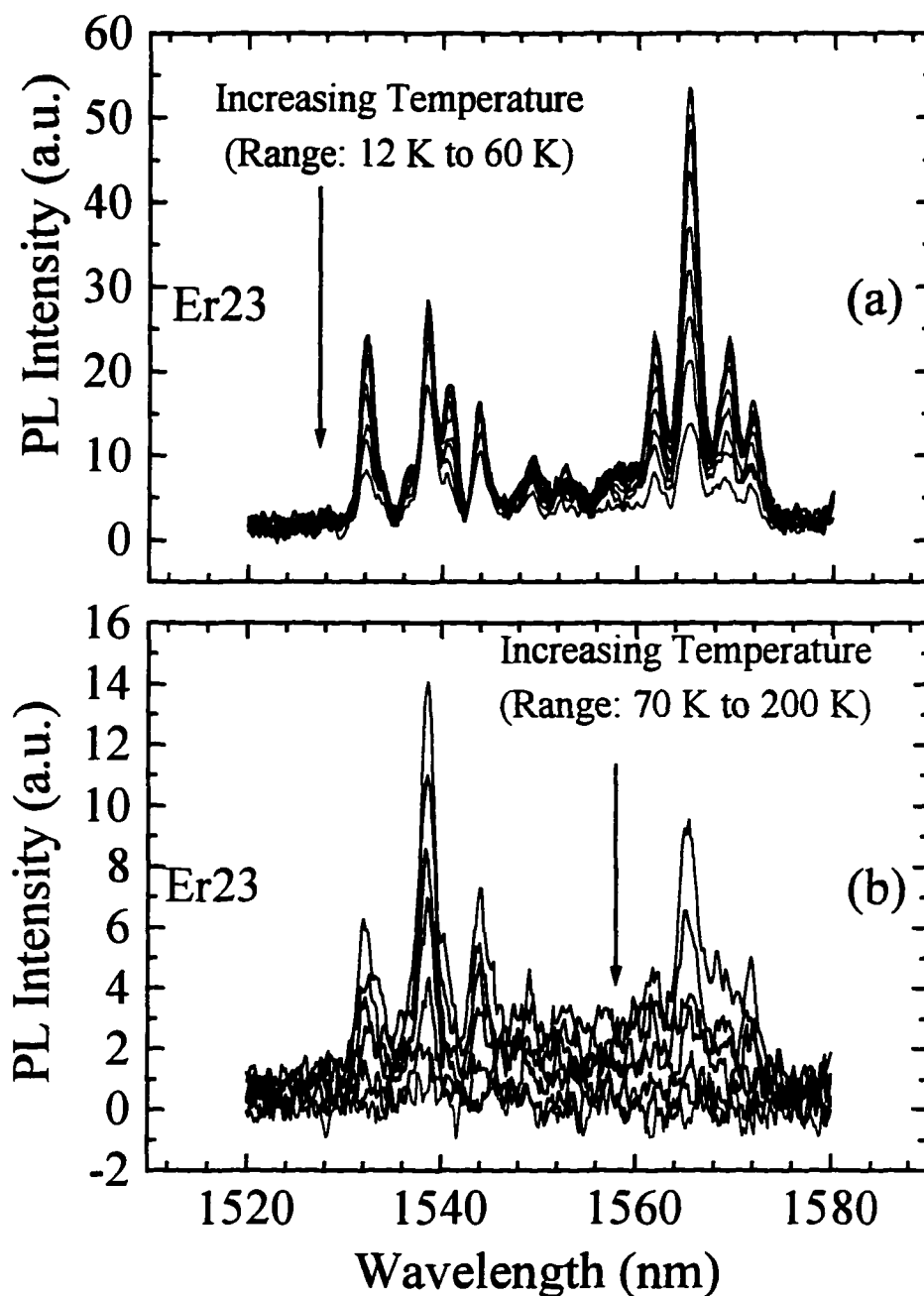


Figure 3.14 Temperature evolution of the PL spectra of Er₂₃ demonstrating the temperature quenching of the *a*, *b*, and *c* lines for the ranges a) 12 K to 60 K and b) 70 K to 200 K.

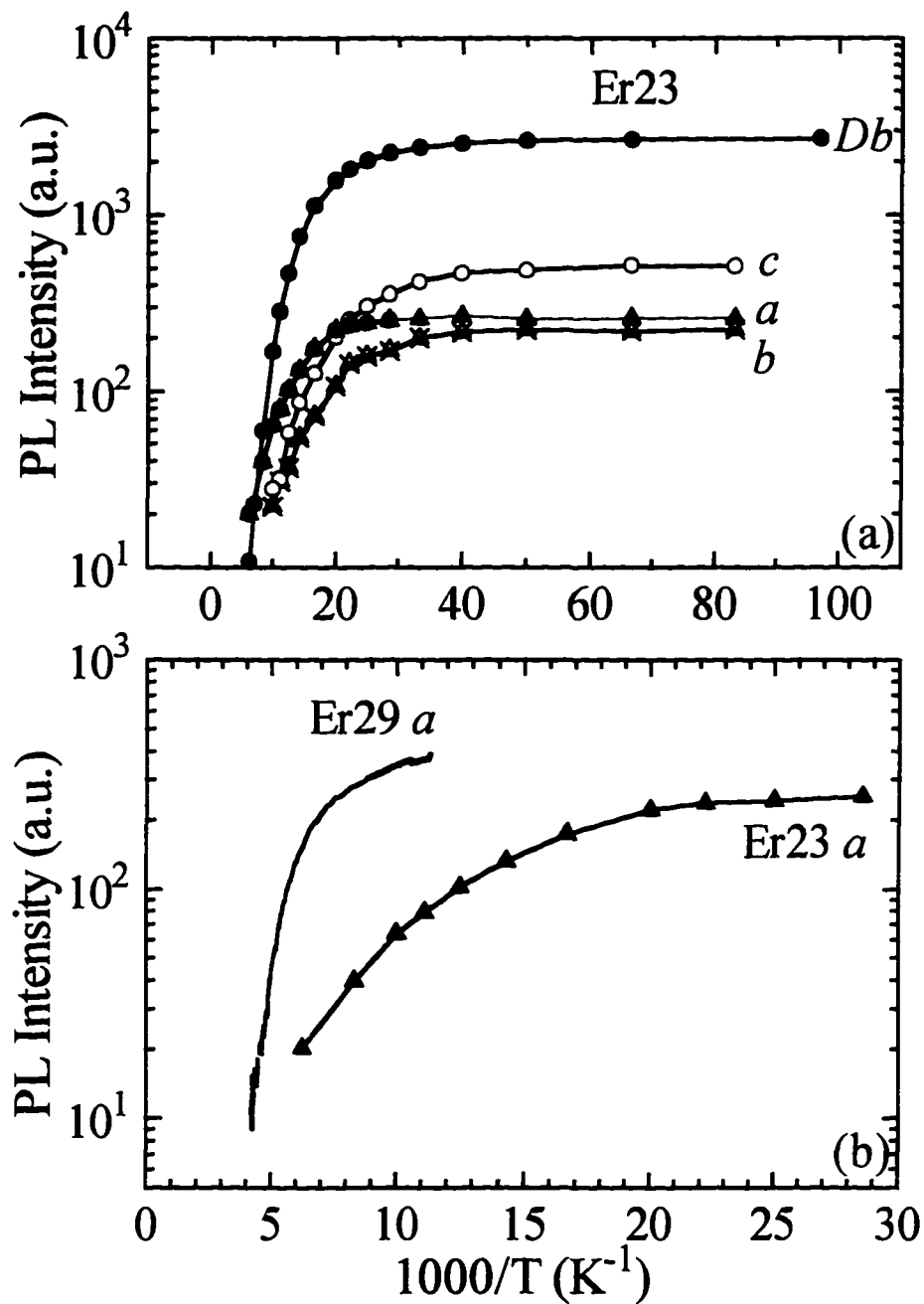


Figure 3.15 a) Temperature dependence of the intensities of the *Db* defect line and the erbium *a*, *b*, and *c* lines for Er23.
 b) Temperature dependence of the intensities of the erbium *a* lines for Er29 and Er23.

In Fig. 3.16 we show a complete PL spectrum for Er23 in the 800-1800 nm range. Series of narrow lines are distinctly seen at wavelengths of 810, 980, and 1550 nm which correspond to transitions of the Er^{3+} ion from three lowest excited states: ${}^4\text{I}_{9/2} \rightarrow {}^4\text{I}_{15/2}$ (1.53 eV), ${}^4\text{I}_{11/2} \rightarrow {}^4\text{I}_{15/2}$ (1.26 eV), and ${}^4\text{I}_{13/2} \rightarrow {}^4\text{I}_{15/2}$ (0.81 eV). Besides the PL band at 640 - 690 nm determined by transitions to the shallow defect traps *Db* and *Dc* and the exciton line discussed above, a wide PL band is observed that peaks around 1000 nm. We believe that this band is caused by optical transitions to the deep hole states *Da*. The observation of a wide band probably indicates the existence of a strong electron-phonon interaction for the deep state.

Thus, we have actually found three types of erbium-induced traps in AlGaAs and PL from the upper excited states, ${}^4\text{I}_{9/2}$ and ${}^4\text{I}_{11/2}$, of the Er^{3+} ions.

Discussion of Er-Luminescence Excitation and De-Excitation Mechanism

Excitation and de-excitation processes of erbium luminescence

Based on our experimental results, we propose the following model for the excitation of the erbium ion 4f-shell. The pump radiation generates electron-hole pairs in the erbium-containing AlGaAs region. Holes are quickly captured by the hole traps *Da*, *Db*, and *Dc* that were induced by erbium being at the cation sites and interstitials (Fig. 3.17). Recombination of a free electron and a hole captured by the trap can be: 1) radiative (i.e. the defect PL that was observed by us at high pump rates), 2) nonradiative multiphonon capture of a free electron, or 3) Auger capture of an electron with excitation of the 4f-shell of an erbium ion (Auger excitation). In the latter case the majority of the

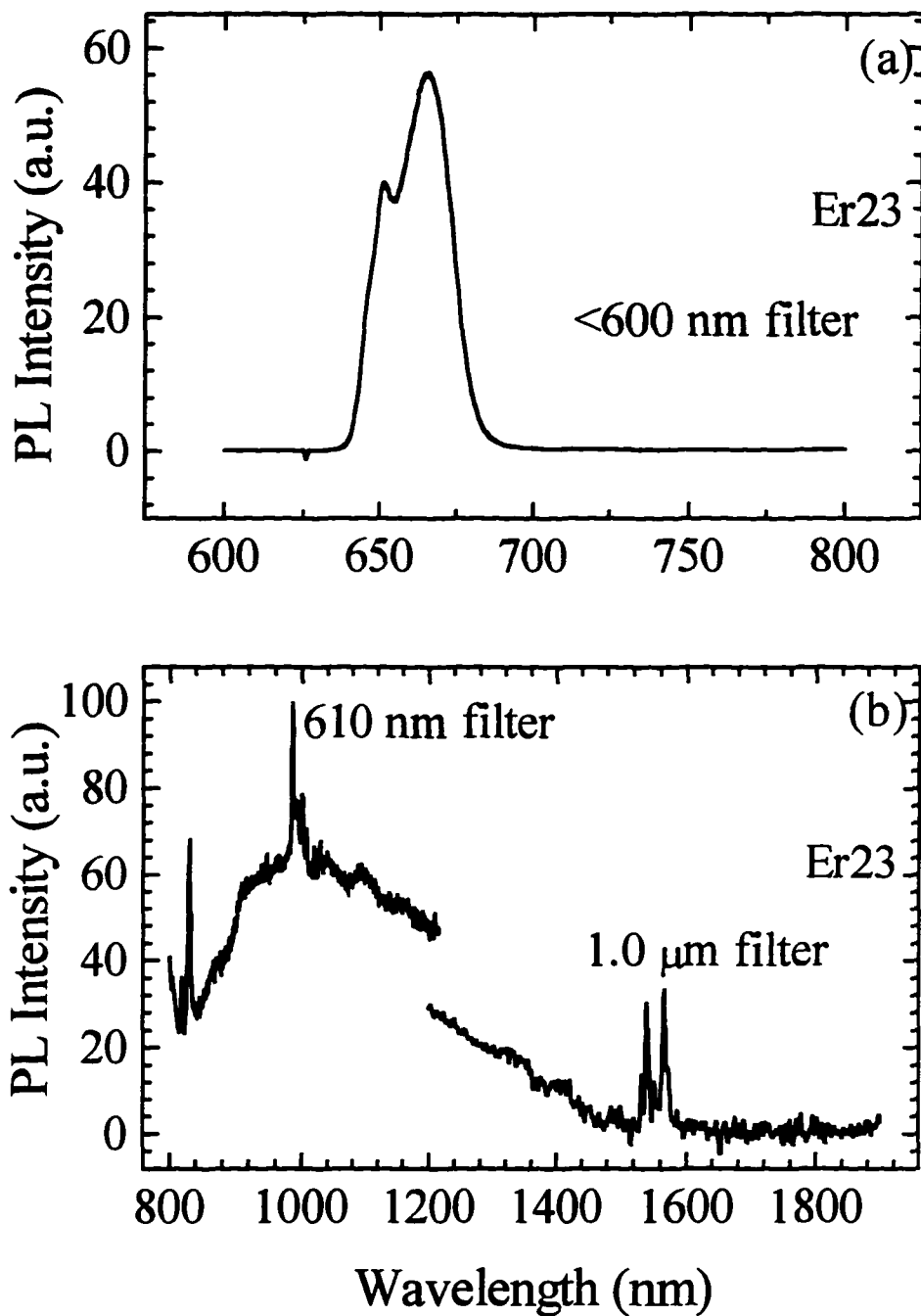


Figure 3.16 PL spectrum taken at 10 K of Er₂₃ in a wide spectral range (800-1800 nm).

recombination energy is transferred to the erbium ion to excite the f-shell via a Coulomb interaction.

The probability of the radiative process (process 1) is only slightly temperature dependent. The main contribution to the temperature dependence of the probabilities of processes 2 and 3 is the existence of energy barriers which control the multiphonon processes required to achieve equilibrium. The probability of Auger excitation increases as the energy of the defect PL approaches the excitation energy of the f-f transition (resonance condition).

In the wide-gap AlGaAs alloy the excitation process proceeds via upper states. In this case the reverse process of de-excitation of the erbium ions from the lowest excited state $^4I_{13/2}$ (the initial state of the 1.54 μm radiative transition) should be negligible. However, de-excitation processes from the upper excited states to which the f-electron is excited in the Auger process can be important. The corresponding probability increases drastically in the resonance condition. The de-excitation process consists of a transition of an f-electron of the erbium ion from the excited to the ground state and a simultaneous generation of an electron-hole pair: a free electron appears in the conduction band while the hole is localized at the defect. If the energy of the electron-hole pair generation exceeds the energy of the f-f transition the energy deficit is compensated by the lattice playing the role of a thermostat.

When the resonance condition is favorable for the excitation process, de-excitation is also enhanced. The fact that the resonance condition is optimal at low temperatures

leads to a sharp temperature quenching of the erbium PL due to de-excitation processes which increase drastically as the temperature rises.

Analysis of experimental data

In Fig. 3.17 a possible diagram for Auger excitation of the erbium ions via deep Da and shallow Db and Dc local states is presented. Since the energies of the defect PL connected with the shallow traps (Db and Dc lines) are close to the energy of the ${}^4F_{9/2} \rightarrow {}^4I_{15/2}$ transition, it is reasonable to propose that the excitation occurs via the ${}^4F_{9/2}$ level. For excitation via the deep trap Da we can expect excitation via the ${}^4I_{11/2}$ and ${}^4I_{13/2}$ levels. This assumption is confirmed by the observation of erbium PL corresponding to the ${}^4I_{9/2} \rightarrow {}^4I_{15/2}$ and ${}^4I_{11/2} \rightarrow {}^4I_{15/2}$ transitions shown in Fig. 3.16.

The fact that the defect PL (Da , Db , Dc) can be observed only for high excitations, when the erbium PL is saturated, indicates that the probability of Auger excitation is greater than that of the radiative transition.

In the case of the excitation of erbium via shallow traps, the temperature quenching of the erbium PL could be controlled by the thermal depopulation of shallow defect levels. We have actually observed this situation for the c line of erbium PL.

In the case of excitation via deep defects Da the temperature quenching is no longer determined by the thermal depopulation of the Da level. We assume that in this case the temperature quenching of the erbium PL is controlled by competition between the Auger-excitation and multiphonon nonradiative capture. This reason is why we can see a line PL to almost room temperature.

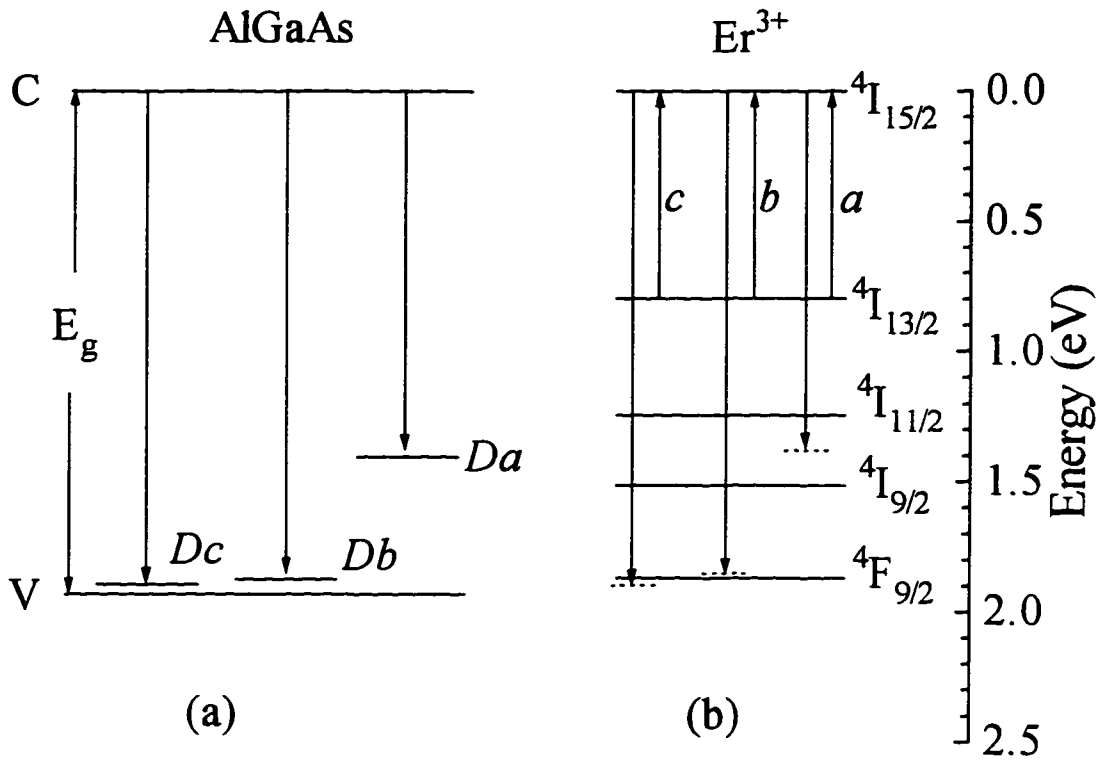


Figure 3.17 Energy level diagram and transition scheme for the Auger excitation of erbium ions via Da , Db , and Dc defect centers. For comparison of the defect and f-f transition energies, the positive direction of the energy axis for the Er^{3+} ion levels is reversed.

Conclusions

In this chapter we have demonstrated that the introduction of erbium into GaAs QW's with AlGaAs barriers during MBE growth leads to strong diffusion of erbium and interdiffusion of gallium and aluminum resulting in leveling of the QW's. These erbium impurities form three types of hole traps in the bandgap of AlGaAs (one of them being deep with a binding energy of about 400 meV, and two shallow ones with energies of 25 and 50 meV). Excitation of the f-shell of the erbium ions in the AlGaAs is determined by an Auger process with the participation of holes captured by the traps, accompanied by excess energy being transferred to local phonons. The temperature quenching of the erbium PL excited via the shallow traps is caused by a thermal depopulation of the defect levels. The temperature quenching of the erbium PL excited via the deep traps is due to an increase in the probability of multiphonon thermally activated capture of free electrons competing with the Auger excitation process. Erbium PL at 1.54 μm excited via a deep trap can be observed nearly up to room temperature. The observation of erbium PL corresponding to the transitions from the $^4I_{9/2}$ and $^4I_{11/2}$ levels indicates that a three-level excitation scheme for the PL at 1.54 μm can be realized in erbium-doped AlGaAs.

Chapter 4

Normal Mode Coupling

Introduction

We now switch from erbium inside quantum wells to quantum wells inside microcavities.

Recently there has been a lot of theoretical and experimental interest [Berman (1994); and Haroche (1992)] in the phenomenon of vacuum Rabi splitting (VRS) in high finesse optical cavities with a strong atom-photon interaction. Sanchez-Mondragon *et al.* (1983) predicted that a single excited atom inside of an optical cavity can lead to a two peak emission spectra, rather than the one peak that would be expected for a bare atom without the cavity. This predicted behavior was experimentally seen several years later by Thompson *et al.* (1992) in a cesium atomic beam with an average number of one atom inside a cavity with a finesse of 8×10^4 .

This phenomenon is a manifestation of the quantization of the electromagnetic field within the cavity and occurs when the system is said to be in the strong coupling regime. This regime is achieved when the coupling between the single atom and the cavity mode, g_0 , dominates over the irreversible losses of the spontaneous emission, γ , and the cavity losses, κ (i.e., $g_0 \gg \kappa, \gamma$ where $\hbar g_0$ is the single-atom vacuum Rabi splitting energy, κ is the cavity mode linewidth, and γ is the atomic spontaneous emission linewidth). This

condition can be realized in very high finesse cavities with the cavity mode in resonance with an atomic energy transition. This situation results in a Rabi splitting of the degenerate energy levels into symmetric and anti-symmetric states for the combined cavity-atom system.

For small numbers of atoms this atom-cavity system must be described using the theories of cavity quantum electrodynamics. When the number of excited atoms, N , is large compared to the number of cavity photons, an entirely classical treatment can be applied [Zhu *et al.* (1990)]. VRS can still be seen in these systems even though the strong-coupling condition, $g_0 \gg \kappa, \gamma$, is not satisfied. The system is said to now be in the nonperturbative regime with $g_0 \sqrt{N} \gg \kappa, \gamma$. This splitting energy, $\Omega_0 = g_0 \sqrt{N}$, thus increases as the square-root of the number of excited atoms, as shown by Agarwal (1984). This result is analogous to the normal mode coupling (NMC) of classical oscillators. In this regime, the reflectivity and transmission properties of the system can be explained by dispersion theory.

Recently this interest in NMC in atomic systems has led attention to be focused on planar semiconductor systems that have a QW heterostructure inside of a distributed Bragg reflector (DBR) cavity [Burstein and Weisbuch (1994); Pau *et al.* (1995); Rarity and Weisbuch (1996); and Yokoyama and Ujihara (1995)]. NMC was first observed in a semiconductor microcavity with a measured finesse of 100-300 by Weisbuch *et al.* (1992). This finesse is orders of magnitude smaller than that for the previously mentioned cavity with a single atom.

A DBR cavity consists of alternating layers of low and high index material; each layer being a quarter of a wavelength of light (in the material) in thickness, with a spacer containing the QW's between one-half and a few wavelengths thick in the middle. An example of a DBR microcavity structure is shown in Fig. 4.1. This structure is also referred to as a vertical cavity surface emitting laser or VCSEL.

The NMC splitting is related to the oscillator strength of the QW transition which is proportional to the peak absorption times the absorption linewidth [Berger *et al.* (1996)]. Enhanced QW exciton absorption will therefore increase the coupling strength between the exciton and cavity mode. The linewidths of the peaks, however, depend on the mirror reflectivities and the absorption homogeneous linewidth. To get a large splitting to linewidth ratio, the mirror reflectivities and the QW exciton oscillator strength need to be high, and the QW exciton linewidth needs to be small.

The nonperturbative regime (often referred to as the strong coupling regime in the semiconductor NMC literature) can be achieved in these microcavities by tuning the cavity mode into resonance with the excitonic resonances of the QW. As the cavity resonance is changed from that of the exciton's resonance, the splitting changes. If one plots the wavelength of these two peaks of the transmission spectra (or dips of the reflectivity spectra) as a function of detuning of the resonances, an anticrossing diagram is created. The point where the exciton resonance is equal to the cavity resonance is the point of minimum splitting, and is at the waist of the anticrossing diagram.

As said before, Zhu *et al.* (1990) have shown how linear dispersion theory is able to explain the splitting, linewidths, and lineshapes of the two NMC peaks in atomic

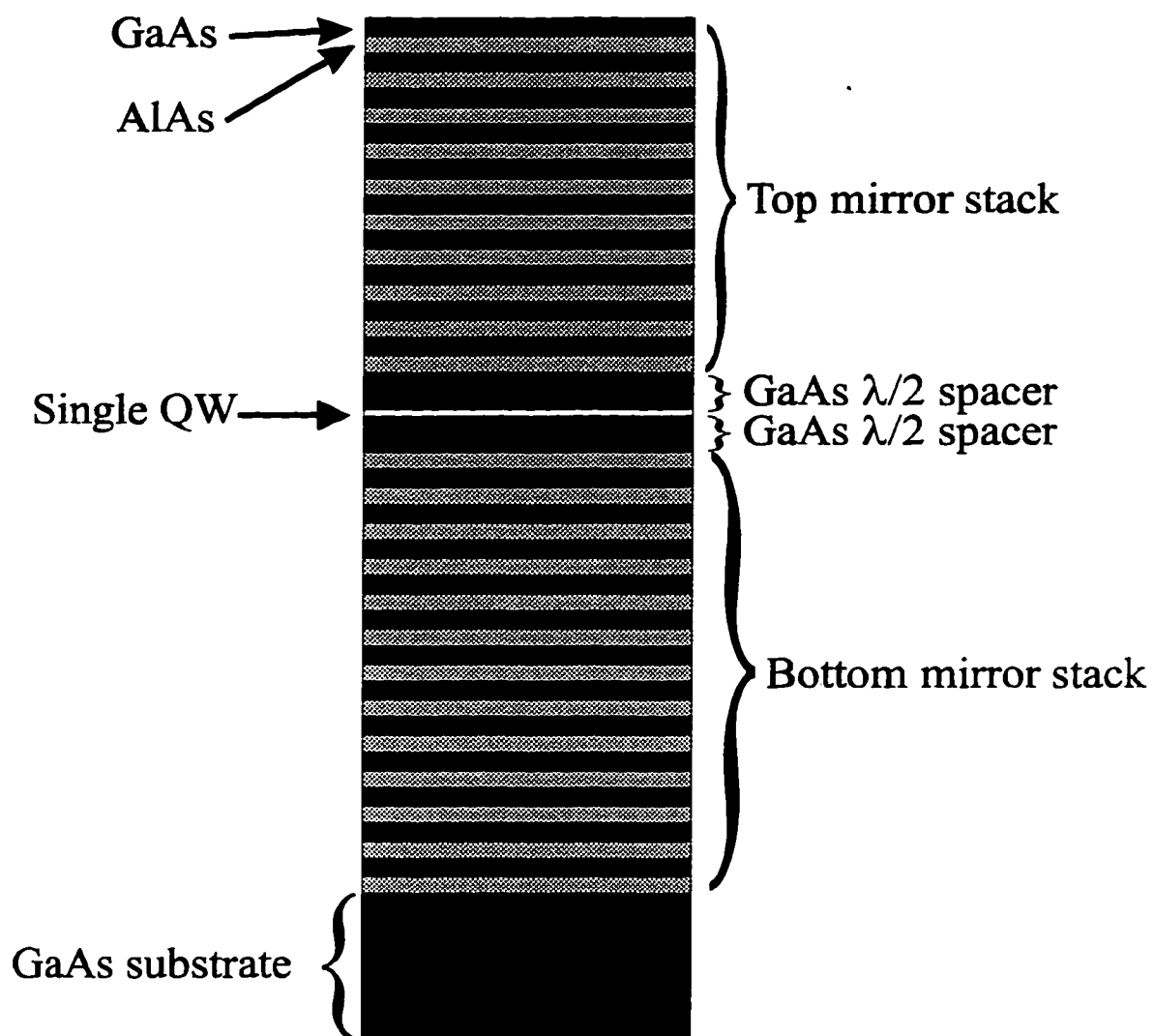


Figure 4.1 Structure of a DBR microcavity. Top and bottom mirrors are 10 and 12.5 periods of GaAs and AlAs quarter wave layers. The λ cavity contains an $\text{In}_{0.03}\text{Ga}_{0.97}\text{As}$ QW.

systems. A similar approach has been taken by Houdre *et al.* (1994) for the semiconductor case in the linear regime.

The main difference between the atomic and semiconductor cases is that nonlinear experiments can be performed on the atomic systems with a known fixed number of atoms, while for the semiconductor case, the exciton number increases with excitation. This makes a theoretical description of the nonlinear dynamics of the exciton-microcavity system much more complex than that of the atom-cavity system.

Our Samples

Our research group started research on NMC in the spring of 1995 with a series of sample growths. The first 30 samples of our NMC series are described in Appendix B. Like the erbium sample series, these were grown in the group's Riber 32P MBE machine by Professors Galina Khitrova and Hyatt Gibbs on undoped GaAs substrates. The samples that are of main interest here are the ones from NMC20 to NMC30 which includes QW samples as well as full microcavity samples. Inside the microcavity of our NMC samples was one or two InGaAs QW's with around 3% In. The QW consisted of an 80 Å InGaAs well and a 920 Å GaAs barrier. An absorption curve taken at 4K of 20 of these QW's (sample NMC21) is depicted in Fig. 4.2a. The figure shows the prominent light-hole resonance below (in wavelength) the strong and narrow heavy-hole resonance as well as the GaAs bandedge going up to the left.

The microcavity or etalon structure that we used consisted of alternating quarter wave layers of GaAs (high index material) and AlAs (low index material) with varying

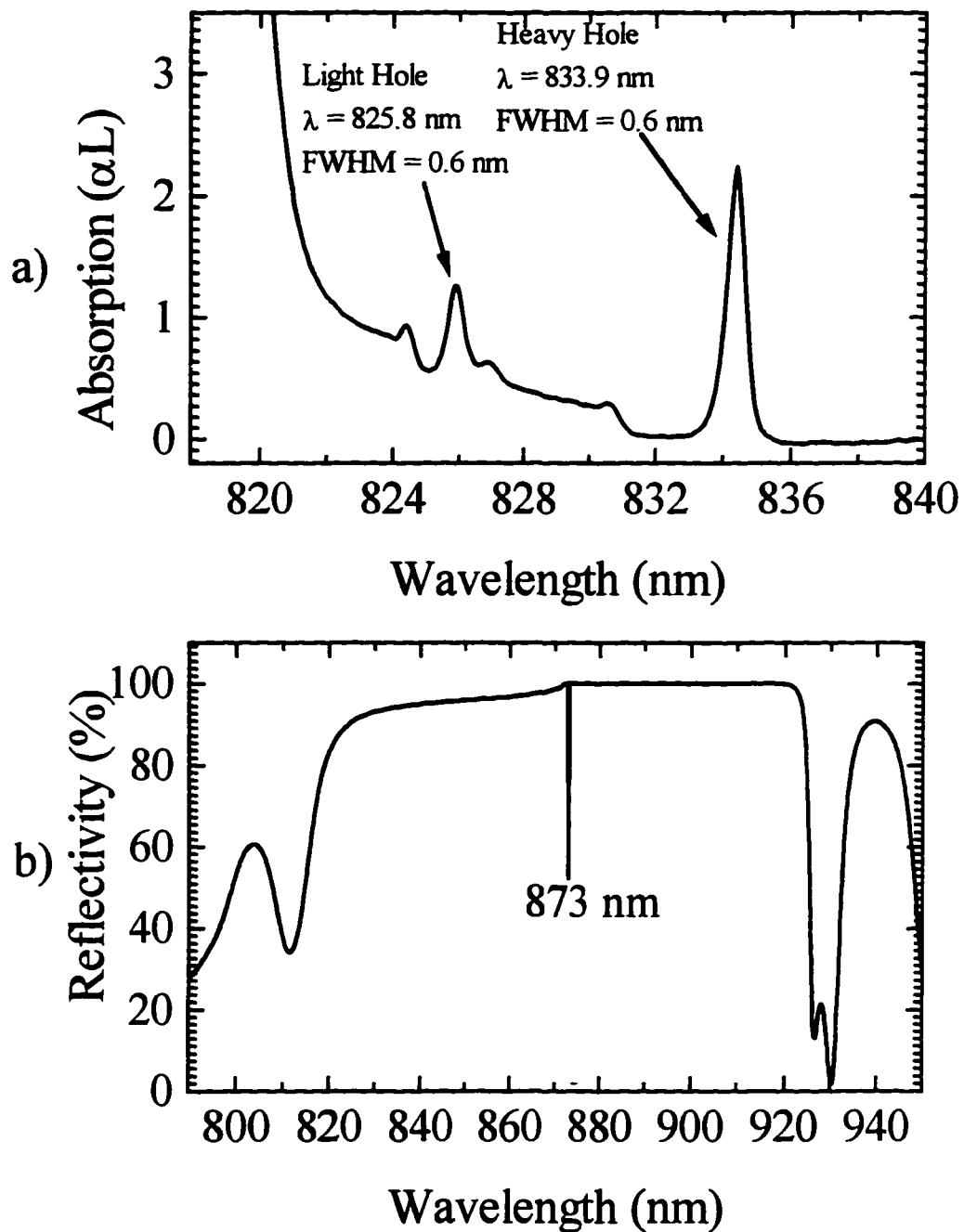


Figure 4.2 a) Absorption spectrum of 20 InGaAs QW's (NMC21) used in our NMC samples. Spectrum taken at 4K.
b) Calculated reflectivity spectrum of NMC20 showing Fabry-Perot dip at 873 nm.

numbers of periods depending on the sample. The top mirror of the microcavity requires less periods to get the same reflectivity as the bottom mirror because of the large refractive index difference at the air-GaAs interface. A calculated reflectivity spectrum of NMC20, which consisted of 19 quarter wave periods on top and 21.5 periods on the bottom, is shown in Fig. 4.2b. This spectrum clearly shows the stop band (wavelengths where transmission is low) as well as the Fabry-Perot resonance.

MBE grown layers vary in thickness across the wafer they are deposited on; the layers are thickest in the center and become thinner towards the edges in a radial manner if the substrate center is concentric with the flux maxima. In our case, the Fabry-Perot resonance of the distributed Bragg reflector cavity is more sensitive to this thickness variation than the QW resonances. One can use this thickness variation to scan the Fabry-Perot resonance in wavelength through the QW resonances by changing sample position because the Fabry-Perot shifts to lower wavelength as one moves out from sample center. The NMC samples were thus grown with the Fabry-Perot resonance at a higher wavelength than that of the QW resonance at the center of the sample.

Experimental Setup

Absorption measurements, such as Fig. 4.2a, were made using a white-light source imaged through a pinhole and onto the sample with a probe spot size on the sample of approximately 50 μm . The sample was contained in a Heli-Tran liquid-helium open-cycle cryostat which allowed sample temperatures down to 4K. The probe spot was then imaged into a 3/4m spectrometer equipped with an optical multichannel analyzer (OMA)

linear charge-coupled device (CCD) array which allowed time averaging of the measured signal. This absorption setup is shown in Fig. 4.3a.

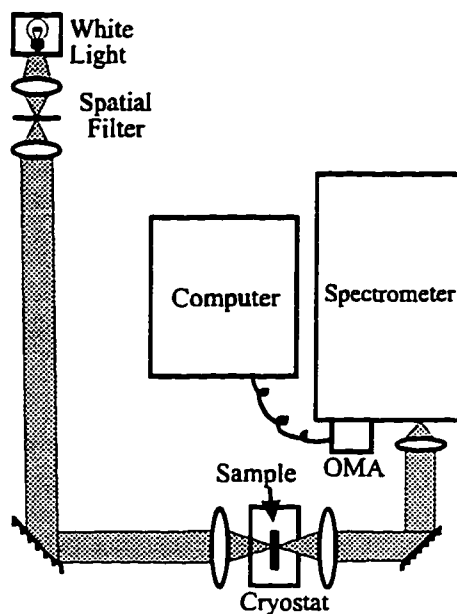
Reflectivity and anticrossing diagrams were made with a similar setup, but using a beam splitter as depicted in Fig. 4.3b. The cryostat was mounted on a motorized-xyz micrometer with sub-micron resolution which allowed tuning of the Fabry-Perot resonance by scanning the probe spot position. A reference mirror was needed to normalize the reflectivity spectrum of the non-uniform white light to a 100% scale. The reference mirrors that were used was first a silver mirror, then a gold mirror, and finally the stop band of the NMC sample itself far from the Fabry-Perot resonance. This last mirror gave the best normalization.

NMC20 Measurement

Our first sample that we witnessed exhibiting NMC was NMC20. It consisted of a microcavity with 19 periods of alternating quarter-wave layers of GaAs and AlAs for the top mirror and 21.5 periods of the same material for the bottom mirror. This number of periods gives a fairly high calculated reflectivity of 99.93% and 99.92% for the top and bottom mirrors respectively. The cavity was $3/2\lambda$ thick GaAs with two QW's like that of NMC21 inside, each at an antinode of the cavity's intensity profile. A reflectivity measurement made of this sample near minimum splitting is pictured in Fig. 4.4 which shows the two dips due to NMC.

The FWHM linewidth of the narrower right dip of the reflectivity spectrum of NMC20 is approximately 0.158 nm. The splitting between the two dips of 2.6 nm gives

a) Absorption Setup



b) Reflectivity Setup

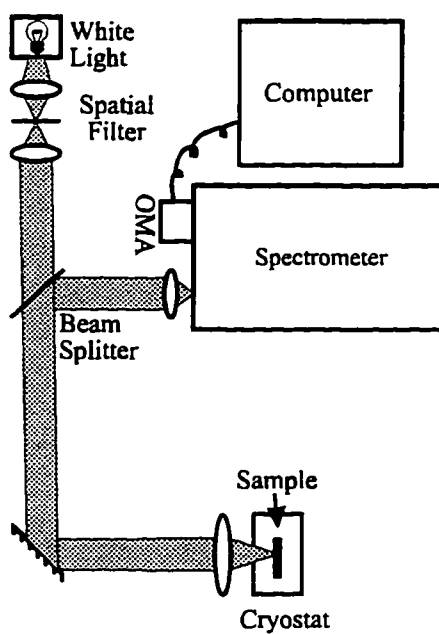


Figure 4.3 a) White light absorption setup.
b) White light reflectivity setup.

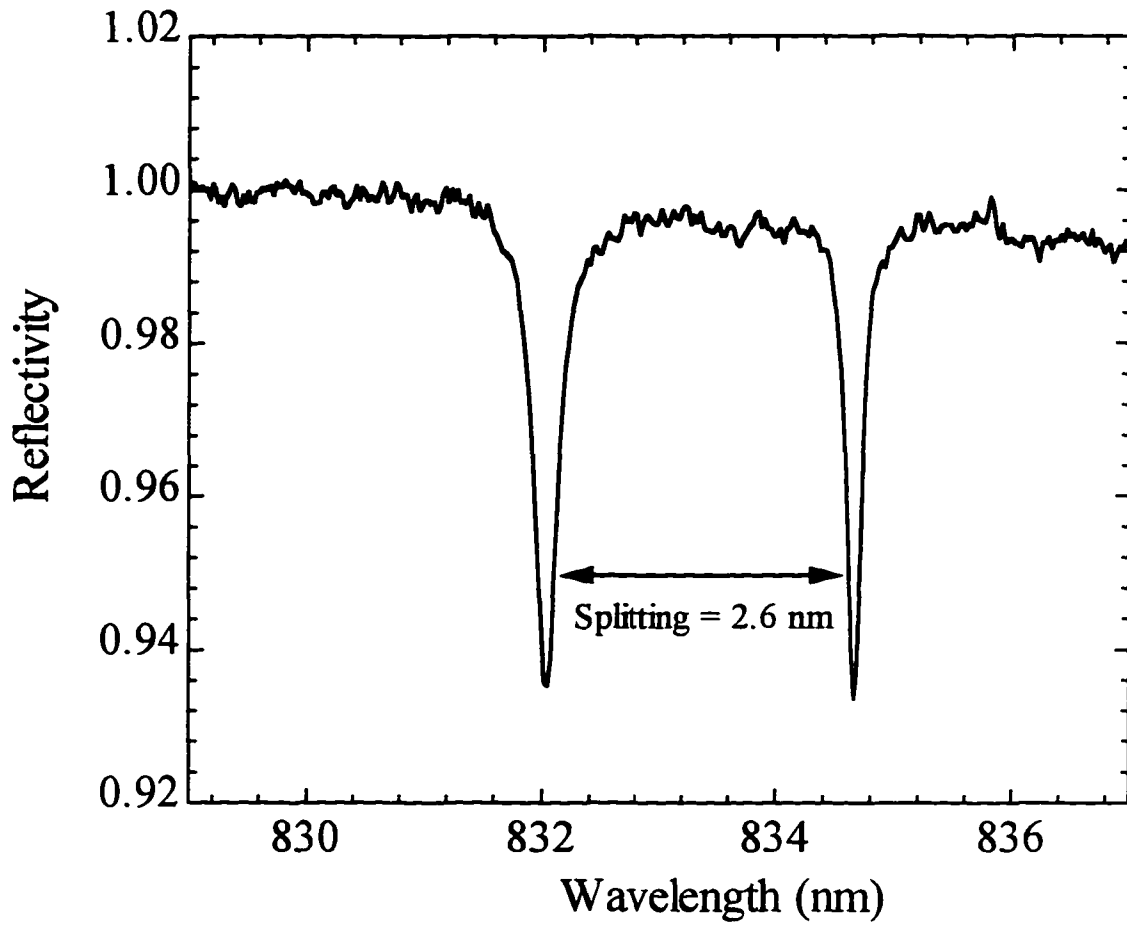


Figure 4.4 Reflectivity spectrum of NMC20 taken at 4K near minimum splitting.

a 16.5 splitting to linewidth ratio. We believe this to be the highest splitting to linewidth ratio to be reported. We achieved this large ratio because of our high reflectivity mirrors and narrow linewidth and high absorption of the two QW's.

NMC22 Measurements

The next sample to be considered is NMC 22. It consisted of a similar structure to that of NMC20 except that it had 14 quarter-wave layer periods for the top mirror and 16.5 periods for the bottom mirror. This number of periods gives a slightly lower calculated reflectivity than NMC20 of 99.5% and 99.44% for the top and bottom mirrors respectively, and therefore slightly wider NMC reflectivity dips. The cavity was also $3/2\lambda$ thick GaAs with two QW's, like that of NMC21, at the antinodes of the cavity. Five reflectivity measurements made of this sample at different detunings are pictured in Fig. 4.5a.

The wavelength locations of the two reflectivity dips were taken from many such reflectivity measurements with different detunings between the cavity and the exciton. This detuning was again accomplished by moving the white-light probe spot to different positions on the sample thus changing at which wavelength the Fabry-Perot resonance occurred. The resulting anticrossing diagram of dip wavelengths versus detuning is pictured in Fig 4.5b.

As can be seen in Fig. 4.5a, the top spectrum has the more Fabry-Perot-like dip on the left, and the more exciton-like dip on the right. As we tune the Fabry-Perot resonance towards a minimum splitting of about 2.55 nm, the two dips become very much like each

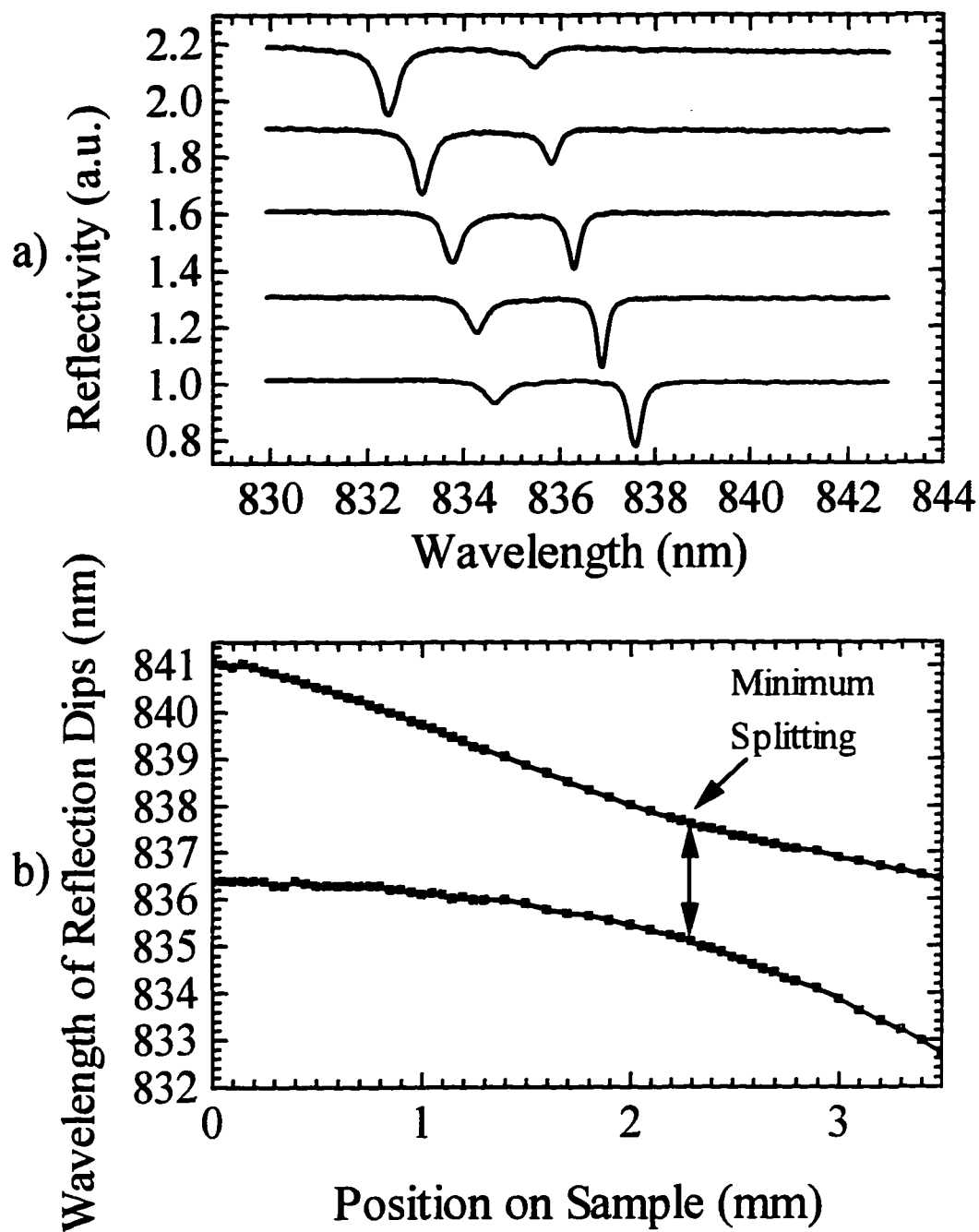


Figure 4.5 a) Reflectivity spectra for different detunings on sample NMC22 at 4K. Spectra are separated for clarity.
 b) Anticrossing diagram for NMC22 taken at 4K. The beam spot positions are not the same as a), but are taken from the same sample.

other, as in the third spectrum, because of the maximum coupling between the Fabry-Perot and the exciton. Further tuning of the Fabry-Perot makes the right-hand dip look more like the cavity resonance, while the left-hand dip has the character of the exciton. As can be seen in Fig 4.5a the Fabry-Perot-like dip is not the same width on either side of the resonance because of the GaAs bandedge absorption.

These changes are reflected in the anticrossing diagram of Fig. 4.5b. As can be seen in this figure, the upper Fabry-Perot-like curve starts in the upper left-hand corner and descends towards the flatter exciton-like curve as the cavity is tuned. Past minimum splitting, the character of the curves is reversed; the lower curve is now more cavity-like, and the upper curve is the flatter exciton-like curve.

NMC28 Measurements

We now consider sample NMC 28. It also consisted of a similar structure to that of NMC20 except that it had 10 quarter-wave layer periods for the top mirror and 12.5 periods for the bottom mirror. This number of periods gives a lower calculated reflectivity of 97.69% and 97.41% for the top and bottom mirrors respectively. The cavity was different in that it was a one λ thick GaAs spacer with only a single QW like that of NMC21 at the antinode of the cavity's intensity profile.

Three reflectivity spectra of this sample are shown in Fig. 4.6. These spectra were not normalized as well as the previous measurements as can be seen by their strange tilting, but the main features are still easily seen. In this Fig. 4.6a we can see NMC between the HH exciton and the cavity with a smaller splitting than the previous

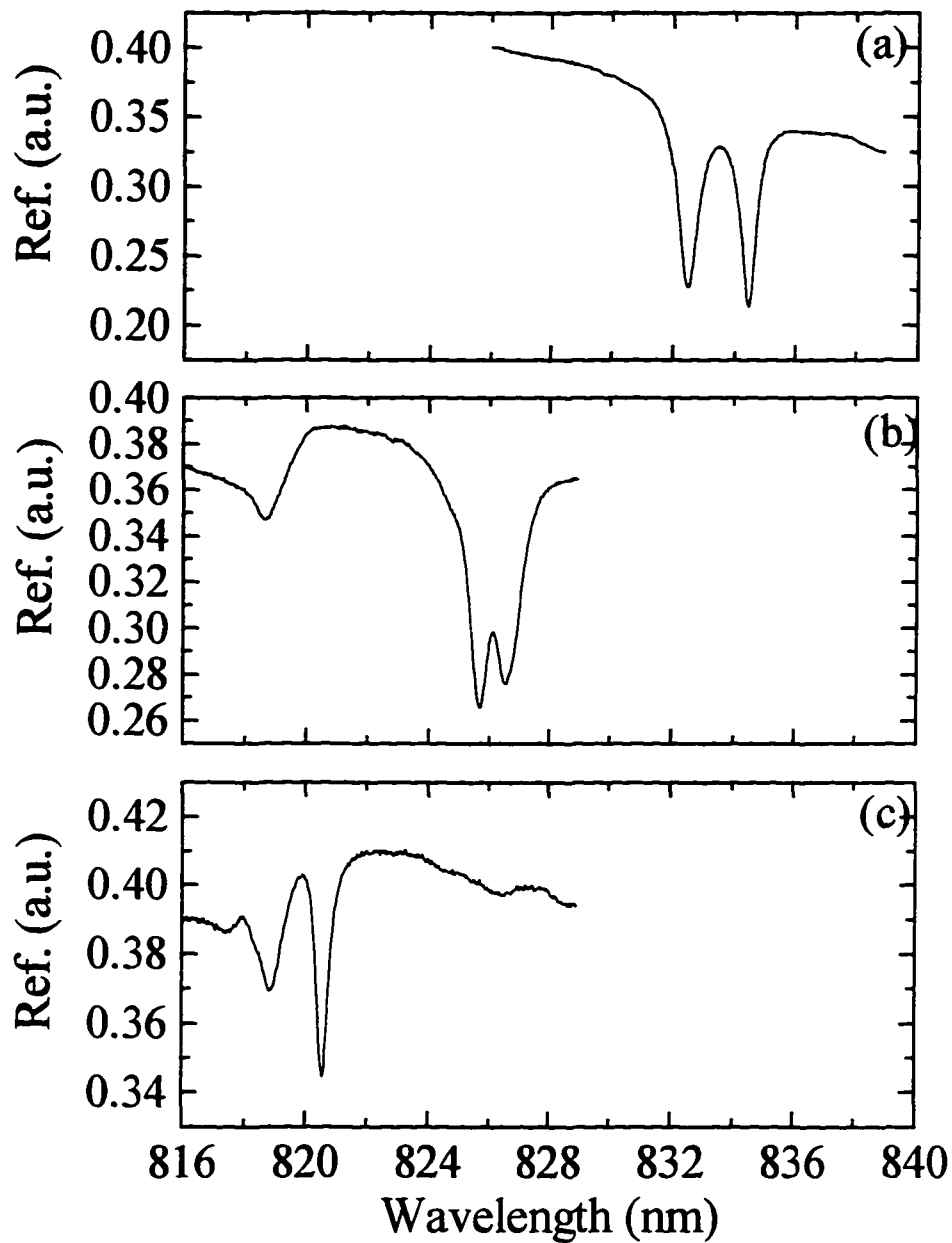


Figure 4.6 a) Reflectivity spectrum for NMC28 at 4K showing NMC with the quantum well HH exciton.
 b) Reflectivity spectrum for NMC28 at 4K showing NMC with the quantum well LH exciton.
 c) Reflectivity spectrum for NMC28 at 4K showing NMC with the GaAs exciton of the cavity spacer and mirror layers.

two samples of 2.0 nm. The dips are also not as well defined as before; the spectrum between the dips does not return to maximum reflectivity. However, with this sample we can see NMC with not only the LH exciton of the QW as shown in Fig 4.6b, but also with the HH exciton of the GaAs in the spacer and mirrors layers. Because of the lower oscillator strength of the LH as compared to the HH, the NMC splitting is smaller for the LH, but the splitting then increases for the interaction with the stronger GaAs exciton. This sample shows that a single narrow-linewidth quantum well can be sufficient for NMC.

Nonlinear Experiment

We will now discuss a nonlinear pump-probe measurement that we performed on sample NMC22. We will return to more linear measurements of NMC samples in the next chapter.

NMC nonlinear measurements have been performed previously by Houdre *et al.* (1995) and Rhee *et al.* (1996). The first group performed their measurements with a quasi-cw pump laser and looked only at the emitted PL. The second group performed their measurements using femtosecond laser excitation pulses and saw a reduction of the splitting with increased pump powers.

In this series of measurements, sample NMC22, which was described earlier, was investigated by the experimental setup shown in Fig. 4.7. An infrared light-emitting diode (LED) with a peak wavelength of 855 nm and a spectral FWHM of 50 nm was used as a broadband probe, replacing the white light source of earlier experiments because of the

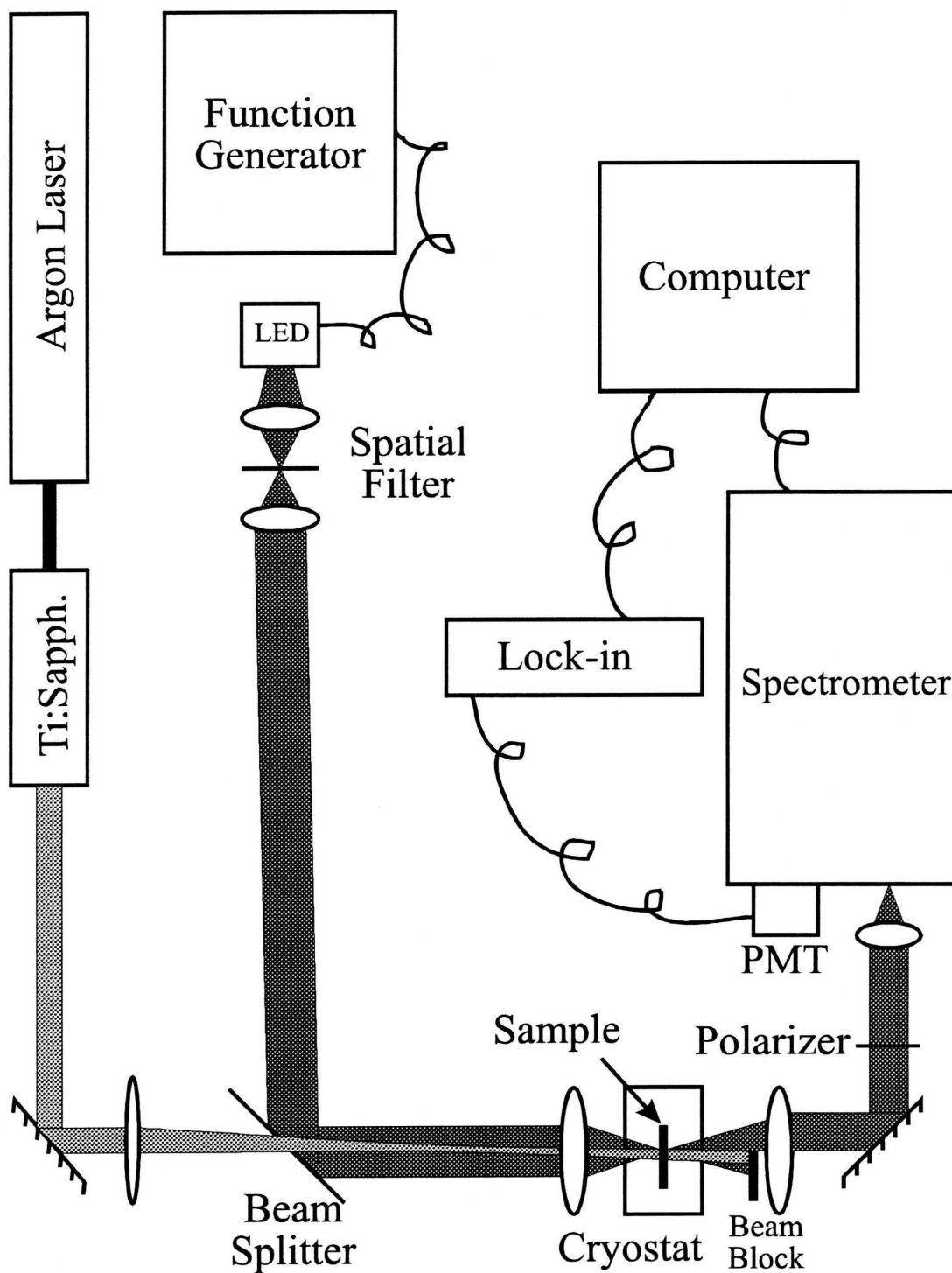


Figure 4.7 Experimental setup for the cw nonlinear pump-probe measurements made on sample NMC22.

LED's much higher spectral power at these wavelengths. The LED was modulated by a 6 kHz square wave to allow the use of a lock-in amplifier for signal detection. The LED was imaged through a pinhole to clean up the beam and then imaged onto the sample with a spot size on the sample of 30 μm . The transmitted light was then focused on a scanning spectrometer with 0.2 nm resolution and detected by an R943-02 photomultiplier tube (PMT). The signal from the PMT was then sent to a lock-in amplifier to extract the desired LED transmission signal. The lock-in amplifier and spectrometer were interfaced to a computer to allow data collection of the transmission spectra.

The pump was a cw tunable Ti:sapphire laser itself pumped by an argon-ion laser. The pump beam was focused to a 46 μm spot concentric with the LED probe spot on the sample. The pump was at an incident angle of 3 degrees to allow blocking of the non-absorbed pump by a beam block on the other side of the sample to prevent flooding of the PMT by the pump signal. In addition a linear polarizer was placed in the probe beam entering the spectrometer crosswise to the polarization of the Ti:sapphire to further prevent any stray laser light from entering the spectrometer. The wavelength of the laser was set to 787 nm which corresponds to a reflection minimum of the NMC22 microcavity structure. At the same time the pump-probe measurements were collected, PL from the sample was detected using a spectrometer outfitted with an OMA linear array detector. All the measurements were taken at 4K.

Fig 4.8 shows the nonlinear pump-probe measurement of sample NMC22 near minimum splitting with increasing pump powers from top to bottom. Repeated in each of

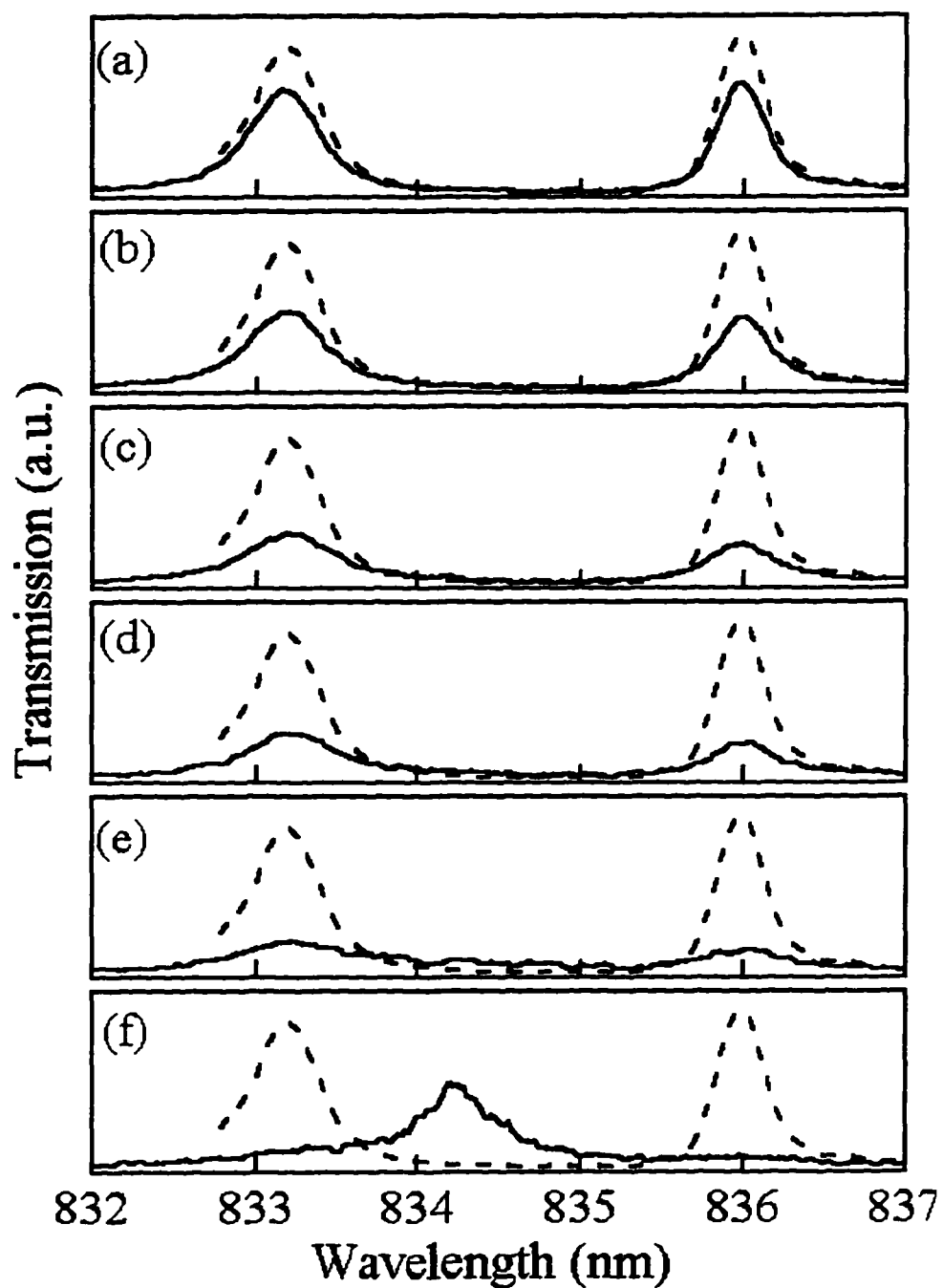


Figure 4.8 NMC22 pump-probe transmission spectra with increasing pump power from a) to f). Included in each plot is a dashed reference transmission spectrum of the probe alone.

these plots is the transmission of the LED through the sample without any pump and is depicted as a darker dashed line.

There are several interesting features of this figure. With the increasing pump intensity there is a corresponding decrease in the probe signal in both peaks, however there is no change in NMC splitting. At high enough intensity, the transmission opens up near the center, with the transmission spectra giving evidence for a collapse of the splitting.

This transmission behavior can be qualitatively modeled using linear dispersion theory along with a transfer matrix procedure [Zhu *et al.* (1990); and Houdre *et al.* (1994)]. Absorption spectra of the 20 QW sample, NMC21, was taken with different pump powers of Ti:sapphire laser light shining upon the sample. The technique used was similar to the earlier nonlinear measurement, except that absorption was measured, and not transmission. The absorption could not be seen to completely saturate because the PL of the sample saturated the PMT preventing detection of the weaker probe signal. These pump-probe absorption measurements are shown in Fig. 4.9a.

Using the Kramers-Kronig transformation as described in Kittel (1986), this series of absorption curves were transformed into a series of differential index curves as shown in Fig. 4.9b. The dashed line in this figure is the “load line” from the Fabry-Perot equation. Where the load line intersects an index profile is a solution to the Fabry-Perot equation, and transmission should be at a maximum. The two outside intersections do correspond to the NMC peaks seen in Fig. 4.9c. The center solution is masked by

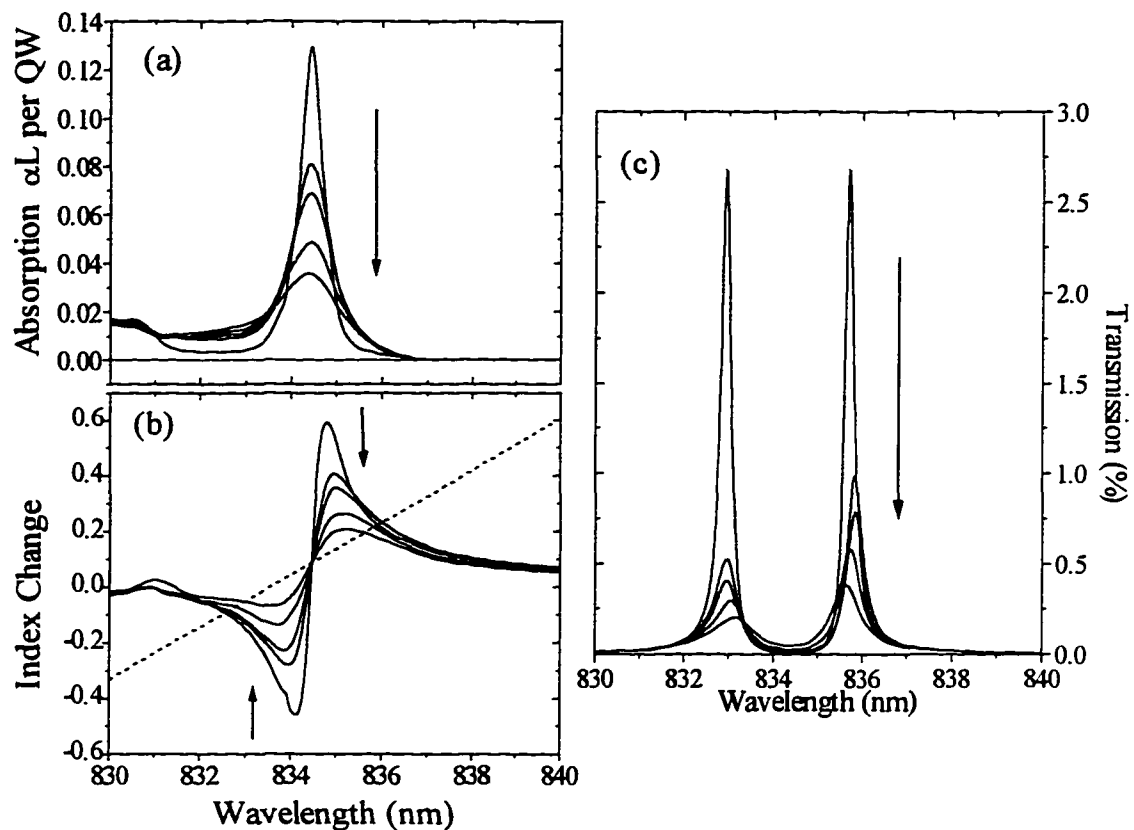


Figure 4.9 a) Measured nonlinear absorption measurement of NMC21 at 4K. Arrow shows direction of increasing pump power.
 b) Nonlinear index spectrum calculated using the Kramers-Kronig transformation of the absorption curves of a).
 c) Calculated NMC transmission curves using the index curves of b) and transfer matrix method.

absorption and transmission only becomes high when the absorption has been saturated as seen in Fig. 4.8f.

Using the techniques described in Born and Wolf (1980), a transfer matrix calculation of our sample structure was made using each of these index changes. These calculations are shown in Fig. 4.9c. As can be seen, these calculations match the characteristics of the experimental curves quite well. The height of the transmission peaks drops while retaining an almost constant splitting as the power increases.

As seen in Fig. 4.9a the exciton peak broadens as it is bleached leaving about the same amount of area underneath it. Thus the oscillator strength of the exciton remains almost unchanged, and therefore the NMC splitting remains almost constant. When the exciton is totally bleached, there is no oscillator strength left, there are no longer the conditions for NMC, and the transmission peak comes up in the center.

The reduced transmission with increased pump can be explained also as a consequence of the broadening of the exciton peak. This broadening increases the absorption of the NMC peaks, thus decreasing the transmission at the peak wavelengths. With very high pumping the QW's exhibit gain and lasing occurs near the midpoint of the original NMC peaks.

To see a more rigorous theoretical examination of this nonlinear behavior of our sample using a microscopic theory for excitonic nonlinearities and light propagation in semiconductor microcavities, see Jahnke *et al.* (1996).

Other NMC Work We Have Done

There are some other papers the groups of Professor Khitrova and Professor Gibbs have published on NMC including Berger *et al.* (1996) which discusses the enhancement of NMC in our samples when subjected to a high magnetic field. The exciton oscillator strength is enhanced by magnetic field confinement. This increase in oscillator strength thus increases the NMC splitting.

Another paper is Nelson *et al.* (1996b) which describes NMC coupling in microcavities with oxidized AlAs layers replacing the normal AlAs layers in the DBR mirrors. Because of the much smaller refractive index of the oxidized AlAs (1.5 as compared to 2.934 for AlAs) fewer mirror layers can be used to get an equivalent reflectivity for an AlAs/GaAs system. The fewer number of layers there are for the same reflectivity, the higher the confinement of the field to the inside of the cavity. The NMC splitting is proportional to the square root of the inverse confinement length of the cavity mode [Stanley *et al.* (1996)]. Decreasing the confinement length increased the NMC splitting. In fact, in the sample described in this paper, we saw NMC at room temperature with a splitting of 6.72 nm.

Some results that were described earlier in this chapter are also discussed in Wick *et al.* (1996) and Nelson *et al.* (1996a). In the next chapter we continue with more linear measurements of NMC.

Chapter 5

Normal Mode Coupling in a Microcavity With Two Different Quantum Wells

Introduction

Most semiconductor microcavity NMC samples have contained several, presumably identical, quantum wells giving rise to reflectivity spectra with two dips in the nonperturbative regime such as those described in the previous chapter. In this chapter we describe NMC samples in which we grew the QW's with transition energy differences much larger than the linewidth in order to study NMC of three coupled oscillators, one the cavity and the other two the nonidentical QW's. Related three coupled oscillator results were reported by Stanley *et al.* (1994) who studied two coupled cavities containing three identical QW's in each.

Experimental Discussion

The three GaAs/AlAs VCSEL's, or microcavities, used here were again grown by MBE upon GaAs substrates and were designed to operate at 4K. The samples were similar and only differed by the indium concentration in the QW's. The top and bottom mirrors consisted of 10 and 12.5 periods respectively of 61.2 nm GaAs and 74.1 nm AlAs layers. The calculated reflectivity at the design wavelength of 860 nm was 97.69 % for the top mirror and 97.41 % for the bottom mirror. The $3/2 \lambda$ GaAs cavity contained two 8.0 nm $\text{In}_{(x)}\text{Ga}_{(1-x)}\text{As}$ QW's of slightly different indium concentration ($x \approx 0.03$) created by

a slight change in the indium cell temperature for the growth of the second well. These QW's were placed at intracavity field maxima positions ($\lambda/2$ points) in the cavity. We referred to our three samples as NMC23, NMC27 and NMC30 after their growth order, and their structure is depicted in Fig. 5.1.

As described in the previous chapter, MBE grown layers vary in thickness across the wafer they are deposited on. We again used this fact to scan the Fabry-Perot resonance, in wavelength, through the QW resonances by changing sample position. Reflectivity and anticrossing diagrams were made at liquid-helium temperatures with a white-light probe imaged into a spectrometer as depicted in the reflectivity setup in the previous chapter. Experimental anticrossing plots were made for each of the three samples and are represented in Figs. 5.2a, 5.3a, and 5.4a by the solid curves. Individual measured reflectivity plots are pictured in Figs. 5.2b, 5.3b and 5.4b and are represented by the solid curves.

Theory

Theoretically, double QW's in a microcavity have been considered recently by Panzarini and Andreani (1995) and Ivchenko *et al.* (1996). In Panzarini and Andreani (1995) the possibility of observing three peaks in optical spectra when the two QW excitons have different resonance energies was predicted, whereas in Ivchenko *et al.* (1996) it was shown that the triplet can appear in the spectra even if the two QW's are identical. Our samples were originally modeled in collaboration with Alexei Kavokin and Mikhail Kaliteevski of the A.F. Ioffe Physico-Technical Institute. They modeled them by

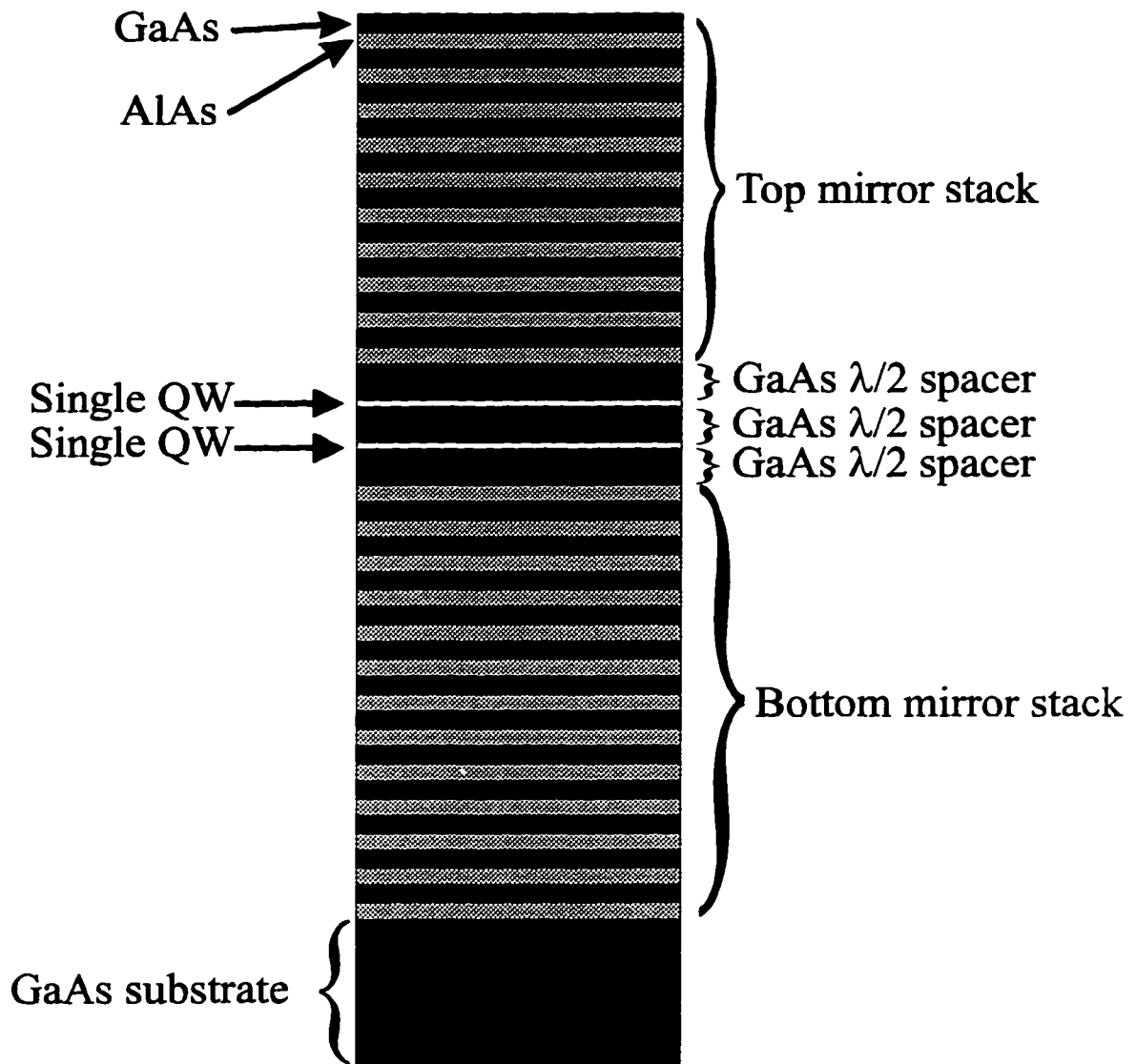


Figure 5.1 Structure of the microcavity. Top and bottom mirrors are 10 and 12.5 periods of GaAs and AlAs quarter wave layers. The $3/2 \lambda$ cavity contains two $\text{In}_{0.03}\text{Ga}_{0.97}\text{As}$ QW's made with slightly different concentrations of indium.

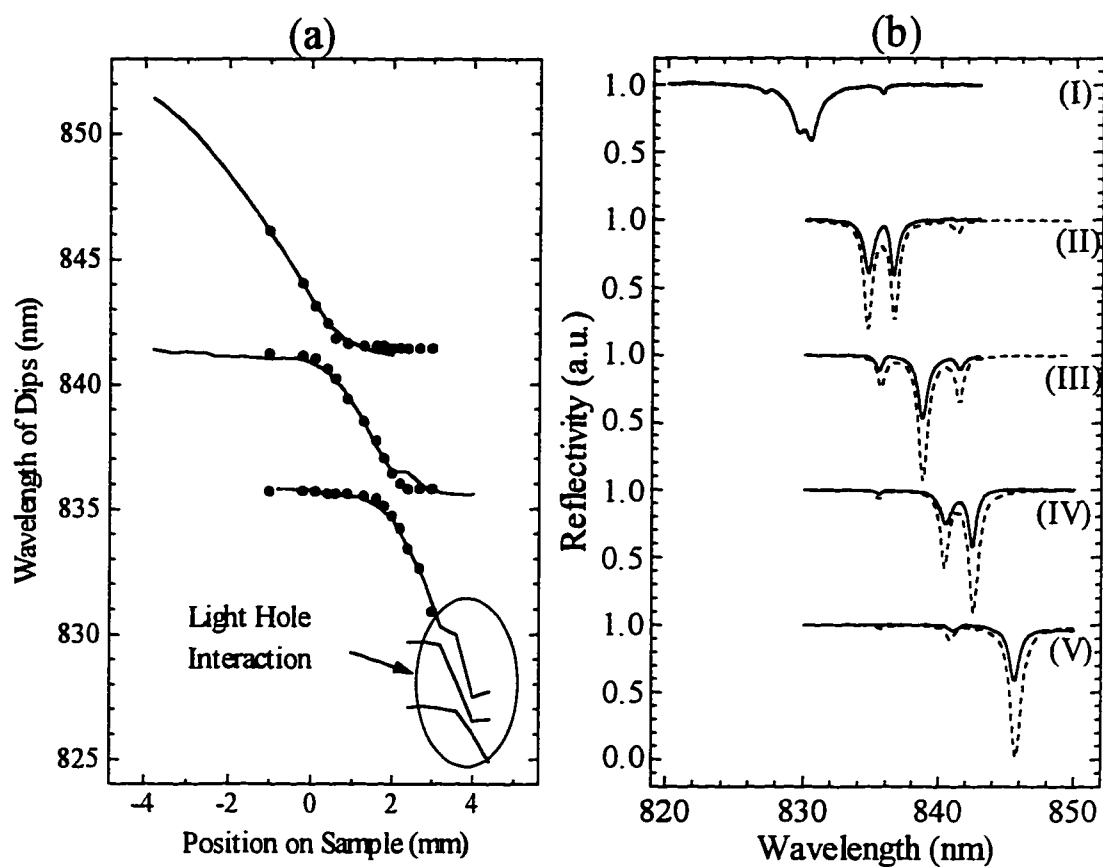


Figure 5.2 a) Anticrossing diagram of NMC27 with ≈ 5.2 nm between the heavy-hole excitons of the two QWs. Solid lines represent measured data while large circles represent calculated results.

b) Reflectivity spectra of NMC27 corresponding to detunings of I) $y = +3.2$ mm, II) $y = +2.0$ mm, III) $y = +1.2$ mm, IV) $y = +0.4$ mm and V) $y = -0.8$ mm. The solid curves represent measured data while the dashed curves represent calculated results. The plots are separated for clarity.

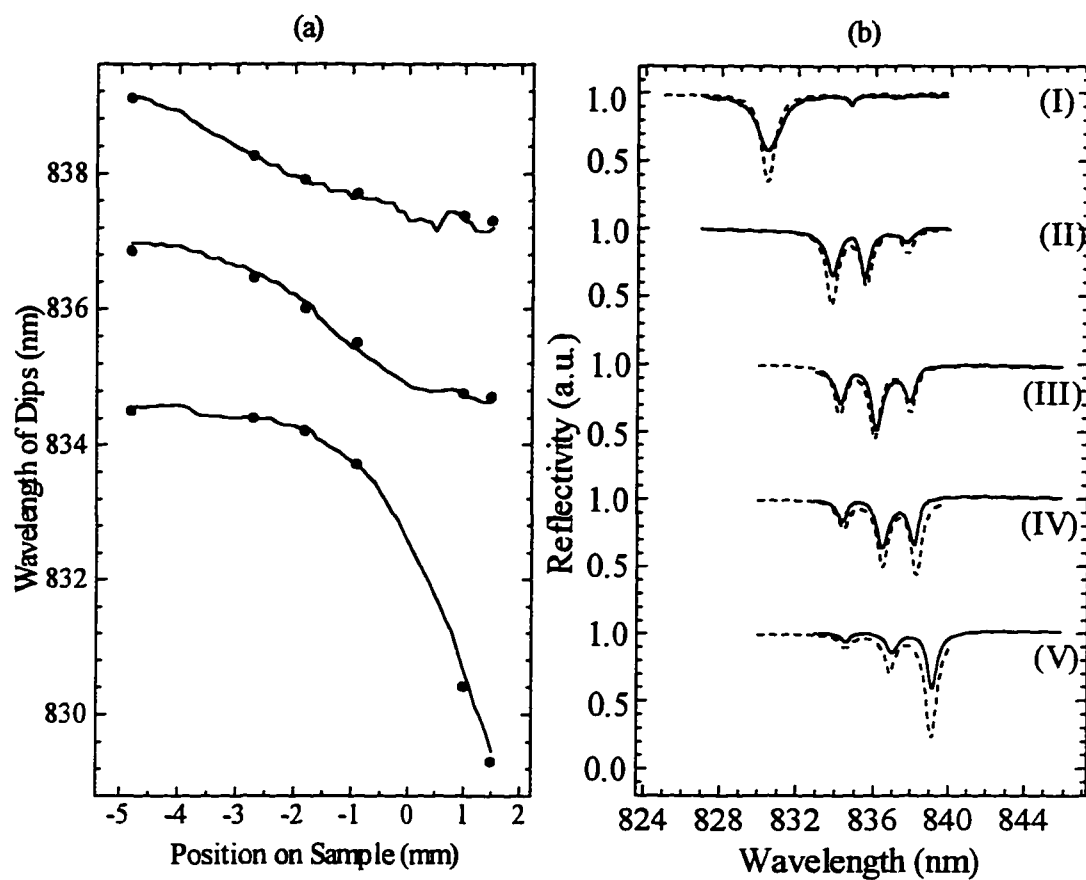


Figure 5.3 a) Anticrossing diagram of NMC30 with ≈ 2.6 nm between peaks.

b) Reflectivity spectra of NMC30 corresponding to detunings of I) $y = +1.3$ mm, II) $y = -1.0$ mm, III) $y = -1.8$ mm, IV) $y = -2.4$ mm and V) $y = -4.7$ mm.

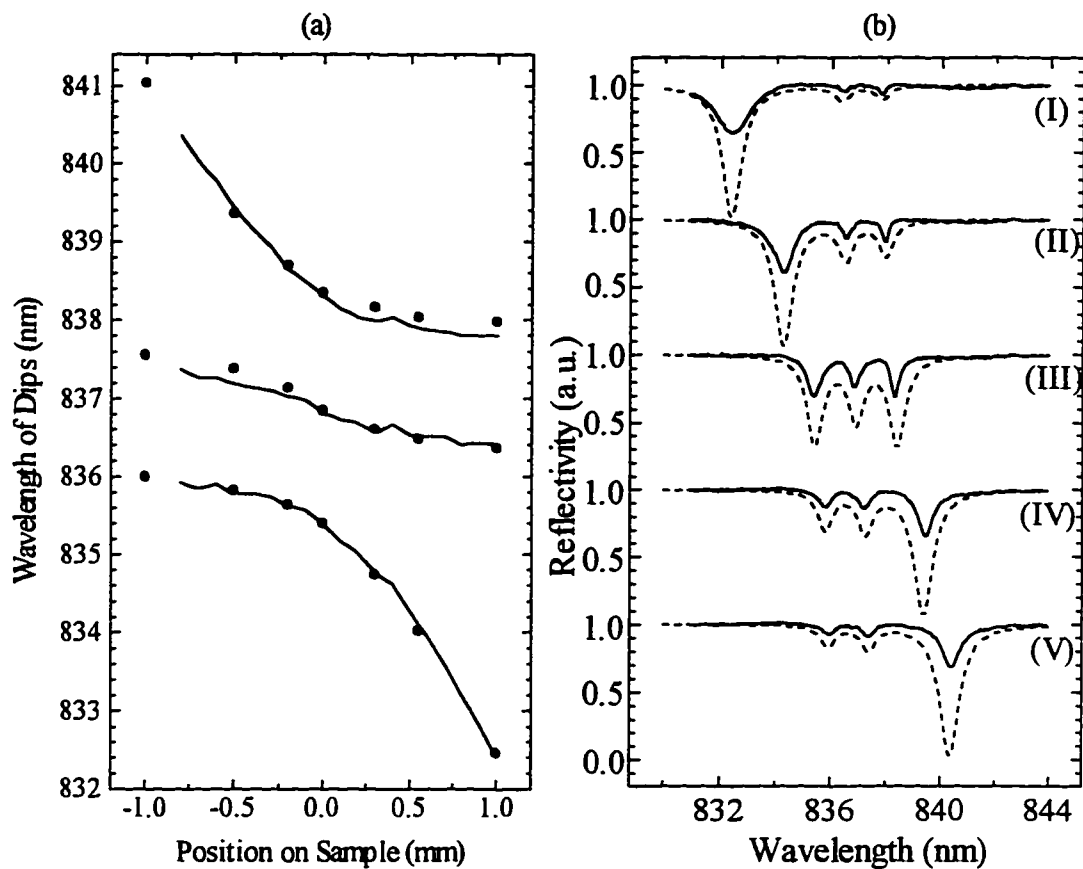


Figure 5.4 a) Anticrossing diagram of NMC23 with ≈ 1.4 nm between peaks.
 b) Reflectivity spectra of NMC23 corresponding to detunings of I) $y = +1.0$ mm, II) $y = +0.5$ mm, III) $y = 0.0$ mm, IV) $y = -0.5$ mm and V) $y = -0.8$ mm.

using the theory of nonlocal dielectric response and transfer matrix method which provides exact solutions of linear-optics reflectivity problems.

They calculated reflectivity spectra using these techniques and our measured parameters. In Figs. 5.2b, 5.3b and 5.4b their calculated reflectivity data are represented by the dashed lines. Overall the calculated reflectivity spectra show good agreement, both in spectral positioning of the reflectivity dips and relative height and linewidths, to the measured spectra. The calculated anticrossing curves are taken from the calculated reflectivity data and are displayed in Figs. 5.2a, 5.3a and 5.4a as large unconnected filled circles. A thorough discussion of these theoretical calculations can be seen in our Optics Letter [Lindmark *et al.* (1996)].

A more simplified method for modeling the essential features of our NMC measurements can be performed by the techniques used by Lyngnes (1997). In this case dispersion theory is used to model NMC. Two mirrors of reflectivity R spaced a distance L apart form an optical cavity, with an index $n(\omega)$ and absorption $\alpha(\omega)$ inside the cavity. This optical etalon has a reflection spectrum given by [Yariv (1985) and Lyngnes (1997)]:

$$\mathfrak{R} = R \left| \frac{1 - e^{2i\Delta(\omega)} e^{-\alpha(\omega)L}}{1 - R e^{2i\Delta(\omega)} e^{-\alpha(\omega)L}} \right|^2 \quad (5.1)$$

where the phase change in a single pass through the etalon $\Delta(\omega) = \frac{\omega}{c} n(\omega)L$, and the

frequency $\omega = 2\pi \frac{c}{\lambda}$.

Our excitonic transitions can be modeled with a Lorentzian lineshape. The absorption and index of refraction for this type of transition are given by [Milonni and Eberly (1988) and Lyngnes (1997)]:

$$\alpha(\omega) = \alpha_0 \frac{\gamma^2}{(\omega_0 - \omega)^2 + \gamma^2} \quad (5.2)$$

$$n(\omega) = \frac{\alpha_0 c}{2\omega} \frac{\gamma(\omega_0 - \omega)}{(\omega_0 - \omega)^2 + \gamma^2} \quad (5.3)$$

where ω_0 is the resonance frequency, α_0 is the absorption coefficient at the resonance frequency, and γ is the half-width half-maximum (HWHM) of the absorption linewidth.

Equation 5.1 can be modified for two single different QW's such that

$$\alpha(\omega)L = \alpha_{QW1}(\omega)L_{QW1} + \alpha_{QW2}(\omega)L_{QW2} \quad (5.4)$$

where $\alpha_{QW1}(\omega)$ and $\alpha_{QW2}(\omega)$ are the absorption coefficients for the two QW's, and L_{QW1} and L_{QW2} are their thicknesses. We also have to set

$$\Delta(\omega) = \frac{\omega}{c} \left(n_b L + n_{QW1} L_{QW1} + n_{QW2} L_{QW2} \right) \quad (5.5)$$

where n_b and L are the index and thickness, respectively of the spacer material, and $n_{QW1}(\omega)$ and $n_{QW2}(\omega)$ are the indices of the QW's.

These formulas were put into the computer program Mathcad for computation. We used the measurements of QW sample NMC21 for the basic QW parameters. We used $\alpha_0 = 16.2 \mu\text{m}^{-1}$, $\gamma = 0.31 \text{ nm}$, and $L_{QW1} = L_{QW2} = 8 \text{ nm}$ for both QW's. The resonances of the two QW's were determined from the measured data and are given for each sample in

Table 5.1. The thickness of the of the etalon was determined by:

$$n_b L + n_{QW1}(\omega_0)L_{QW1} + n_{QW2}(\omega_0)L_{QW2} = 3\frac{\lambda_0}{2} \quad (5.6)$$

where ω_0 and λ_0 are the resonance frequency and wavelength, respectively of the etalon.

This resonance was determined by the average of the two exciton resonance wavelengths.

Detuning was done by changing the thickness of the etalon, and the values that were used, determined from our measurements, are in Table 5.1.

The calculations using these techniques are presented in Figs. 5.5, 5.6, and 5.7 as dashed lines. The original measured results are depicted as solid lines for comparison. We can see that there is some qualitative agreement between the measured and calculated results, but quantitatively there are large differences. One of the major problems with our

Sample	λ_{QW1} (nm)	λ_{QW2} (nm)	Detunings (nm)
NMC27	835.82	841.09	-3.82
			0.0
			4.01
			7.14
NMC30	834.55	837.15	-5.42
			-0.41
			0.0
			0.56
NMC23	836.40	837.80	3.27
			-4.69
			-2.83
			0.0
			2.32
			3.30

Table 5.1. Parameters used in the calculations for the three different samples.

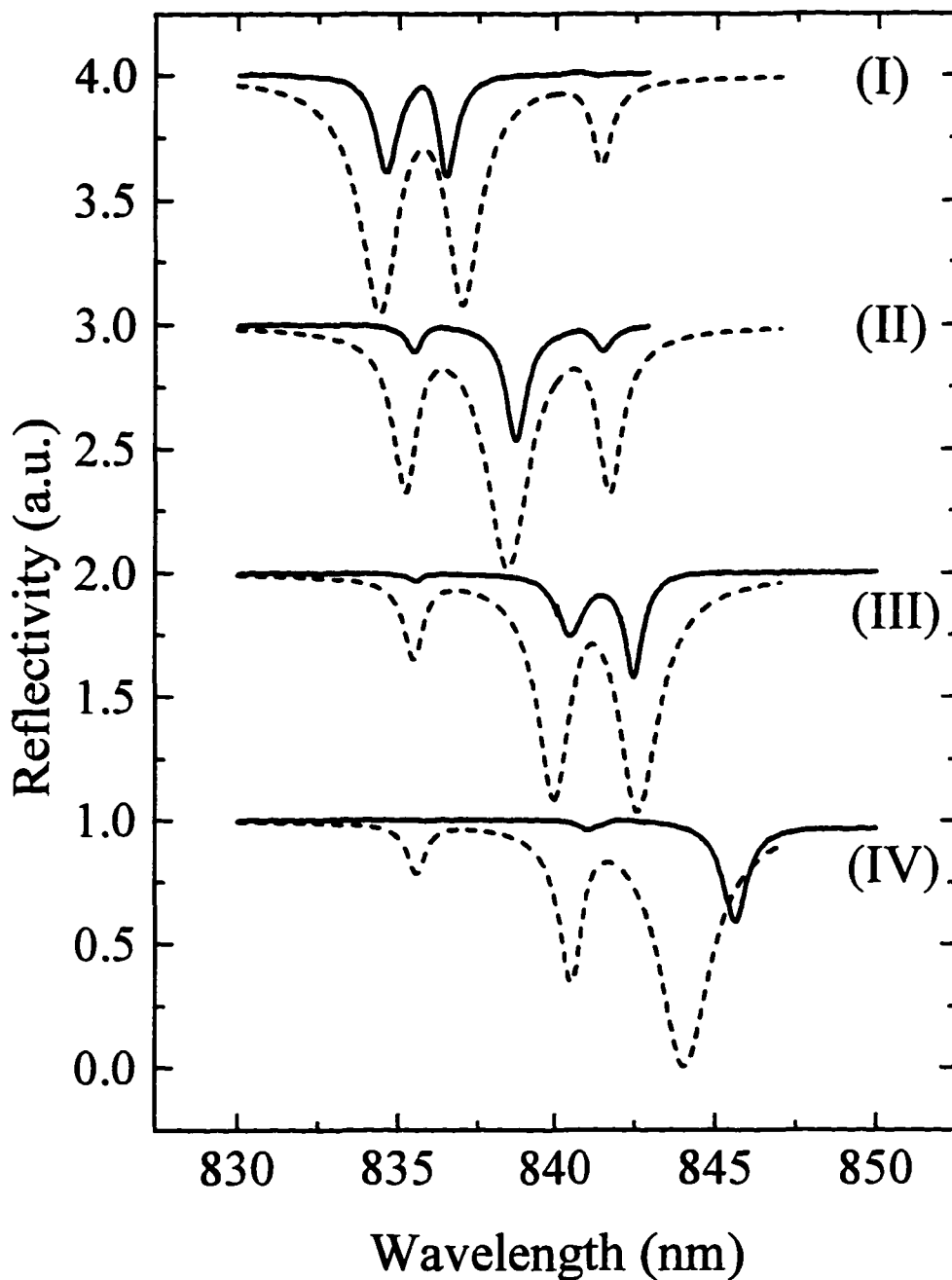


Figure 5.5 Reflectivity spectra of NMC27 corresponding to detunings of (I) -3.82 nm, (II) 0.0 nm, (III) 4.01 nm, and (IV) 7.14 nm. The solid curves represent measured data while the dashed curves represent calculated results from the simple dispersion model. The plots are separated for clarity.

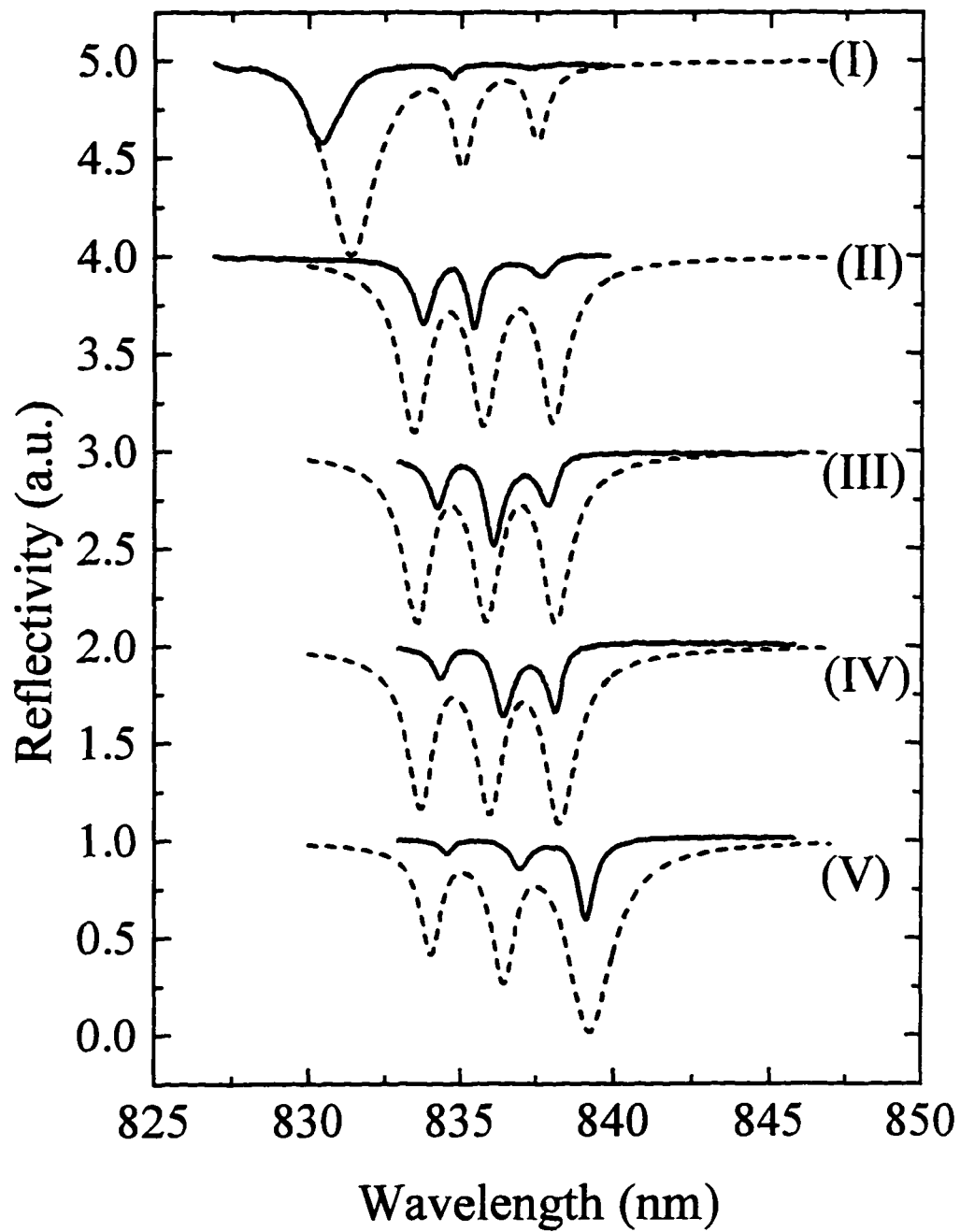


Figure 5.6 Reflectivity spectra of NMC30 corresponding to detunings of (I) -5.42 nm, (II) -0.41 nm, (III) 0.0 nm, (IV) 0.56 nm, and (V) 3.27 nm.

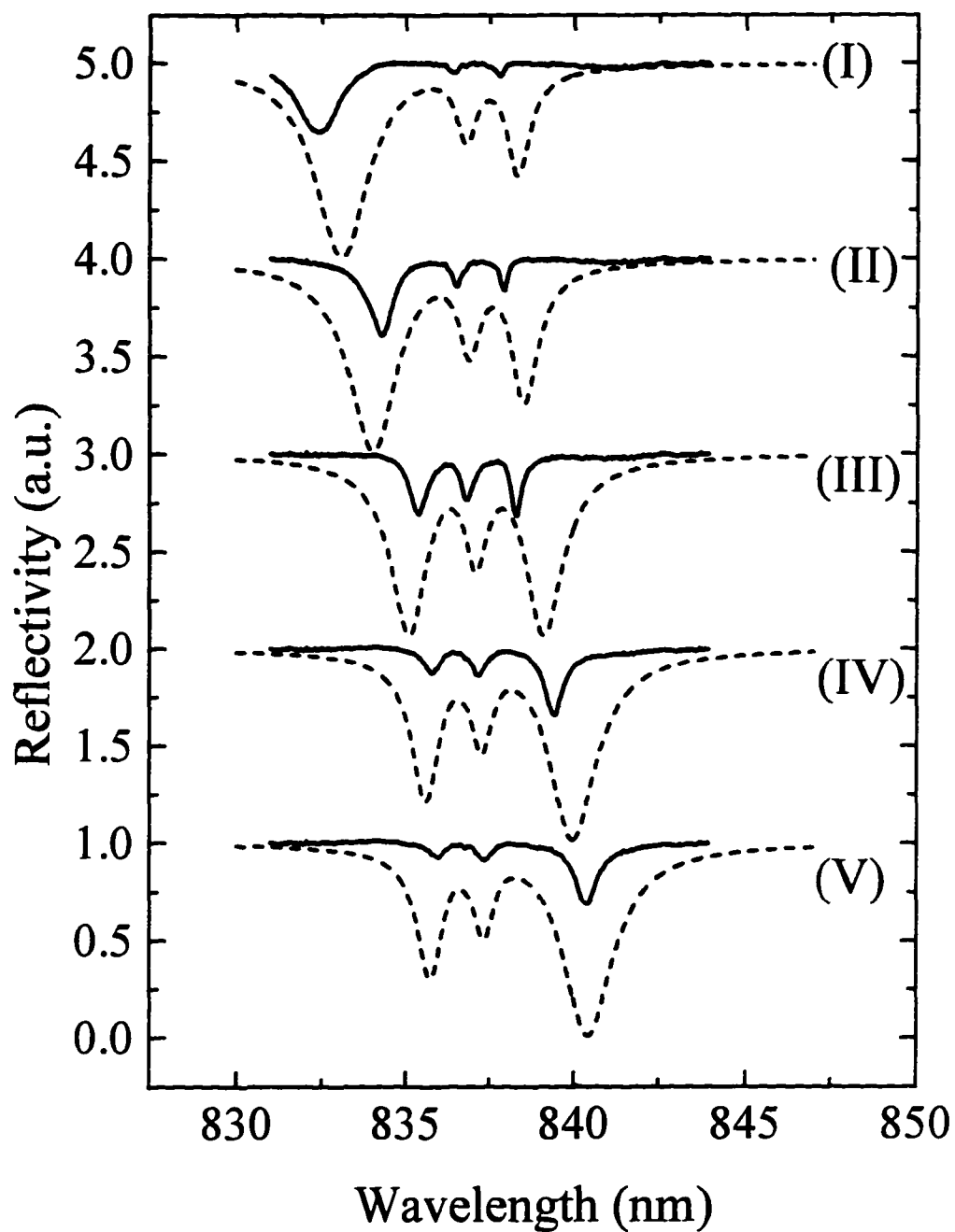


Figure 5.7 Reflectivity spectra of NMC23 corresponding to detunings of (I) -4.69 nm, (II) -2.83 nm, (III) 0.0 nm, (IV) 2.32 nm, and (V) 3.30 nm.

model is that our mirrors are actually made up of quarter-wave stacks of alternating GaAs and AlAs layers. This means that the structure is more complicated than we assumed for our model because the cavity field extends into the mirrors.

Another problem with our model is that it assumes that the QW absorption and index are distributed throughout the spacer. In our samples the QW's are actually placed at antinodes of the standing-wave electromagnetic-field mode within the cavity. The strength of the interaction changes depending on the location of the QW and is strongest when the QW's are at the antinodes. Our model ignores this problem, but it still gives a good qualitative description of NMC in our samples as can be seen in these figures. Our samples are better modeled with the transfer matrix method as can be seen by a comparison with the calculated results in Figs. 5.2, 5.3, and 5.4.

Discussion of Results

Of the three samples, NMC27 has the largest difference between the two exciton energies. In Fig. 5.2b. the larger Fabry-Perot dip can be seen tuning through the excitons, becoming intermixed with each one individually. As expected when the exciton energies are sufficiently far apart, scanning the cavity mode results in two independent two-coupled-oscillator anticrossings. Strain separates the light-hole and heavy-hole transitions by 8 nm, and the narrow linewidth makes the light-hole peak stand out prominently above the heavy-hole continuum; consequently, NMC (Fig. 5.2b(*J*)) and anticrossings (Fig. 5.2a) with the light-hole excitons are also seen.

Sample NMC30 has a smaller difference between the exciton energies than does NMC27. It has similar reflectivity spectra (pictured in Fig. 5.3b) to those of NMC27 except that the Fabry-Perot-like dip is not so pronounced between the excitons (Fig. 5.3b(III)). The anticrossing diagram in Fig. 5.3a shows this, where the center line does not vary as much as the corresponding line for the NMC27 anticrossing diagram. For intermediate exciton energy differences one has three coupled oscillators; Fig. 5.3b(III) shows pushing of the two exciton-like dips by the cavity-like dip between them.

Sample NMC23 has an even smaller energy difference between the excitons. In the series of spectra in Fig. 5.4b the Fabry-Perot-like feature can be seen almost to “hop across” the exciton-like features in the sense that the center dip is never the deepest. The anticrossing diagram in Fig. 5.4a demonstrates this by the almost-flat center line. For small exciton energy differences the two exciton oscillators behave more and more like a single oscillator. When the two quantum wells are grown identically, indeed there is a single anticrossing and the splitting is larger (2.6 nm) as seen in the previous chapter.

Conclusions

In this dissertation we have discussed two different types of semiconductor heterostructures grown by molecular beam epitaxy: QW's doped with erbium and QW's inside a microcavity. In this chapter we have displayed the coupling between a microcavity and two different QW resonances. The simple dispersion theory model gave good qualitative results, but the theoretical model using nonlocal dielectric response and

transfer matrix method gave a much better quantitative correspondence with our measured reflectivity and anticrossing data.

The previous chapter started with a discussion of normal mode coupling in atomic systems and in semiconductors. We considered some of the linear measurements we had made on our samples including absorption and reflectivity. We then discussed experimental linear results of several of our samples. We finished with a nonlinear pump-probe experiment along with a theoretical discussion of the results using Kramers-Kronig transformation and a transfer matrix method.

Chapter 2 gave an historical overview of the origins of the rare earth element erbium. We talked about some of the behavior of erbium when it is placed into semiconductors. We contemplated some of the reasons people are very interested in producing light sources using erbium. We also discussed some of the work that has been done by other scientists in the field of erbium-doped semiconductors and what we planned to do to improve luminescence of erbium doped semiconductors.

Chapter 3 discussed the experimental results of our erbium-doped GaAs/AlGaAs quantum well structures with concentrations of Er in the range of 10^{17} - 2×10^{19} cm⁻³. Photoluminescence (PL) of Er³⁺ ions and Er-induced defects were studied at liquid helium and higher temperatures. A strong diffusion of erbium and interdiffusion of gallium and aluminum ions were observed at the boundary of the GaAs/AlGaAs quantum wells which led, at high erbium concentrations, to the apparent destruction of the quantum wells and macroscopic (average) leveling of the erbium and aluminum concentrations over the whole semiconductor structure. From PL spectra at high resolution, the existence of three types

of Er centers was deduced that differ by the positions of fine structure lines, PL lifetimes, and PL temperature dependence. Our results indicate that these centers are accompanied by the appearance of three types of carrier traps. Our experiments give evidence that the carriers captured into these traps control the Auger excitation of Er ions. Besides erbium luminescence at 1.54 μm , we observed luminescence of erbium ions from upper excited states at 0.82 and 0.98 μm which demonstrates the possibility of realizing a three-level scheme of light emission. So, even though our hoped for break-through of making the erbium luminescence really light up did not occur, we did see some interesting phenomena.

Appendix A
Summary of Erbium Sample Growth

Er Sample #	Growth Date	In Temp	Er Temp	Structure and Comments
1	11-30-94	750 °C	?	GaAs substrate + 30x(3 Å AlAs + 3 Å GaAs + 16 sec InGaAs:Er + 3 Å GaAs + 3 Å AlAs + 210 Å GaAs). No exciton peak at 300K. Broad shoulder beginning at about 935 nm. GaAs bandedge at about 890 nm.
2	12-7-94	750 °C	No Er	Same as 1 except no Er and 17 sec InGaAs. No exciton peak or shoulder at 300K.
3	12-9-94	730 °C	No Er	GaAs substrate + 30x(17 sec InGaAs + 270 Å GaAs). Exciton at 962 nm at 300K.
4	12-11-94	730 °C	750 °C	Same as 3 except InGaAs:Er. Exciton at 926 nm at 300K.
5	12-11-94	730 °C	750 °C	Same as 3 except 19 sec of InGaAs:Er. Exciton at 935 nm at 300K.
6	12-12-94	740 °C	750 °C	Same as 3 except 21 sec of InGaAs:Er. Exciton at 965 nm at 300K.
7	12-12-94	740 °C	750 °C	Same as 3 except 24 sec of InGaAs:Er. Exciton at 970 nm at 300K.
8	12-14-94	750 °C	650 °C	Same as 3 except 24 sec of InGaAs:Er. Exciton at 986.7 nm at 300K.
9	12-14-94	750 °C	900 °C	GaAs substrate + 20x(26 sec InGaAs + 7 nm GaAs:Er + 15 nm GaAs + 7 nm GaAs:Er) + 100 nm GaAs. Exciton at 991 nm at 300K.
10	2-21-95	750 °C	No Er	Same as 9. No exciton peak observed at 300K.
11	2-22-95	750 °C	900 °C	GaAs substrate + 30x(5 nm GaAs:Er + 16 sec InGaAs:Er + 5 nm GaAs:Er + 18 nm GaAs) + 100 nm GaAs. Shoulder 1000 nm at 300K.
12	5-3-95	776 °C	No Er	GaAs substrate + 5x(4x(21 sec InGaAs + 29s GaAs) + 180 sec GaAs) + 6 min GaAs. Trying to reproduce MOD27. Not measured because screwed up. In temperature too high.
13	5-4-96	750 °C	No Er	Same as 12. Broad shoulder at 1000 nm at 300K.

Er Sample #	Growth Date	In Temp	Er Temp	Structure and Comments
14	5-6-95	750 °C	No Er	Same as 12 except different As pressure, and 6 min GaAs between clusters. No exciton peak.
15	5-7-95	750 °C	No Er	Superlattice. Hasenberg approach. GaAs substrate + 50x(8x(4 sec InAs + 10 sec GaAs) + 143 sec GaAs) + 6 min GaAs. No exciton peak.
16	5-10-95	710 °C	No Er	Superlattice. GaAs substrate + 20x(7x(1 monolayer InAs + 6 monolayer GaAs) + 20 nm GaAs + 6 min. of GaAs. Small exciton at 953 nm at 300K.
17	5-10-95	710 °C	No Er	20x(10x(1 monolayer of InAs + 3 monolayers of GaAs) + 20 nm GaAs) + 6 min. of GaAs. Small exciton at 933 nm at 300K.
18	5-11-95	No In	900 °C	Superlattice. GaAs substrate + 20x(5x(7 monolayers of GaAs:Er + 1.4 monolayers of InAs:Er) + 20 nm GaAs). Trying to resonate with 980 nm $^4I_{15/2}$ to $^4I_{11/2}$ transition in Er^{3+} . Large amount of strain at QW interfaces (InAs 6.1 Å, GaAs 5.7 Å).
19	5-13-95	No In	900 °C	Superlattice. GaAs substrate + 19x(10x(7 monolayers of GaAs:Er + 1.4 monolayers of InAs:Er) + 20 nm GaAs). Trying to resonate with 980 nm $^4I_{15/2}$ to $^4I_{11/2}$ transition in Er^{3+} . Large amount of strain at QW interfaces (InAs 6.1 Å, GaAs 5.7 Å).
20	11-10-95	No In	No Er	MQW. GaAs substrate + 0.6 μm $Al_3Ga_{7.7}As$ + 50x(1nm AlAs + 10 nm GaAs:Er + 1 nm AlAs + 21 nm $Al_3Ga_{7.7}As$) + .6 μm $Al_3Ga_{7.7}As$ + thin GaAs cap. Trying to resonate with 810 nm $^4I_{15/2}$ to $^4I_{9/2}$ transition in Er^{3+} . QW's at 800 nm more easily and reproducibly grown than at 980 nm. No strain.
21	11-13-95	No In	900 °C	Same as 20 except with Er in GaAs QW's only. Varying Er concentration in 21-23.
22	11-14-95	No In	870 °C	Same as 20 except with Er in GaAs QW's only.

Erb Sample #	Growth Date	In Temp	Er Temp	Structure and Comments
23	11-14-95	No In	930 °C	Same as 20 except with Er in GaAs QW's only.
24	11-17-95	No In	800 °C	Same as 20 except with Er in GaAs QW's only, and no 1 nm AlAs spikes around QW. Suspect that Er ³⁺ in QW is reacting with AlAs spikes and so wrecking the QW interfaces.
25	11-20-95	No In	900 °C	Same as 24 except QW thinner to adjust for 1 shift due to removing the AlAs spikes and different Er temperature.
26	11-30-95	No In	900 °C	GaAs substrate + 50x(28 sec GaAs:Er + 60 sec GaAs). No AlGaAs. Er in bulk GaAs.
27	1-18-96	No In	No Er	Trying to reproduce 18 except with no Er.
28	1-31-96	No In	900 °C	GaAs substrate + 50x(0.9 nm AlAs + 13.5 nm Al _x Ga _{1-x} As + 0.9 nm AlAs + 19.2 nm Al ₃ Ga ₇ As) + 5.5nm GaAs cap. Will do SIMS to see how Er affects x concentration in AlGaAs growth.
29	2-1-96	No In	900 °C	AlGaAs:Er 1.7 μm thick.
30	2-1-96	No In	900 °C	Trying to reproduce 18.
31	2-8-96	No In	850 °C	GaAs substrate + 100x(1.8 nm AlAs:Er + 9.5 nm GaAs:Er) + 80 nm GaAs cap. No AlGaAs.
32	2-8-96	No In	800 °C	Same as 31. Vary temp.
33	5-13-96	No In	900 °C	Same as 20 except the Er in AlAs spikes and AlGaAs barriers, but not in GaAs QW's. Trying to figure out how Er interacts with Al.
34	5-14-96	No In	900 °C	Same as 20 except no AlAs spikes, and Er in AlGaAs barriers only.
35	5-15-96	No In	850 °C	Same as 20 except Er in AlAs spikes, AlGaAs barriers, and GaAs QW's; no .6 μm AlGaAs on top (makes SIMS measurement easier).
36	5-16-96	No In	820 °C	Same as 20 except Er in AlAs spikes and GaAs QW's only; no 0.6 μm AlGaAs on top (makes SIMS measurement easier).
37	2-4-97	No In	900 °C	GaAs buffer, 1000 Å Al _{0.65} Ga _{0.35} As, 1 μm Al _{0.65} Ga _{0.35} As:Er, 100 Å GaAs on Top

Appendix B
Summary of NMC Sample Growth

NMC Sample #	Growth Date	Type of Sample	Description and Comments
1		QW	Excitons @ 804 to 809 nm
2	3-29-95	QW	15 x (12.5 nm $\text{In}_{0.03}\text{Ga}_{0.97}\text{As}$ well, 16.8 nm $\text{Al}_{0.3}\text{Ga}_{0.7}\text{As}$ barrier), 0.4 μm of AlGaAs above and below, exciton around 815 nm
3	3-29-95	Mirror	8 x (AlAs $\lambda/4$ and $\text{Al}_{0.07}\text{Ga}_{0.93}$ $\lambda/4$) for $\lambda = 830$ nm @ 4K; did reflectivity @4K and saw strange structure
4		QW	50 x (180 Å GaAs well, 238 Å $\text{Al}_{0.26}\text{Ga}_{0.74}\text{As}$ barrier), 580 nm of $\text{Al}_{0.26}\text{Ga}_{0.74}\text{As}$ underneath only; Absorption shows exciton @812 nm @ 4K
5		QW	50 x (180 Å GaAs well, 8.5 Å AlAs + 190 Å AlGaAs barrier), 580 nm of $\text{Al}_{0.26}\text{Ga}_{0.74}\text{As}$ above and below; Absorption shows exciton @814 nm @ 4K
6	4-4-95	Etalon	R measurement shows dip at 906 nm @ 4K
7	4-8-95	Etalon	High index material is 19 x (2 s AlGaAs / 6 s GaAs); 4 periods top mirror, 6.5 periods bottom mirror; R shows $\lambda_{\text{FP}}=841$ nm @ 4K
8	4-9-95	QW	Like NMC5; exciton at 816 nm @ 4K
9	4-10-95	QW + Etalon	6 P top/9.5 P bottom (86.9%/88.4%); Material is 3 wells (like NMC8) placed near center of 1λ cavity; R shows $\lambda_{\text{FP}}=872$ nm @ 4K with stop band FWHM = 137 nm
10	4-11-95	QW	20 x (100 Å $\text{In}_{0.06}\text{Ga}_{0.94}\text{As}$ well, 920 Å GaAs barrier) with 500 nm AlGaAs above and below; absorption shows exciton @ 856 or 857 nm (depending on whether through glass or glass + super glue as reference
11	4-13-95	QW	20 x (100 Å $\text{In}_{0.06}\text{Ga}_{0.94}\text{As}$ well, 920 Å GaAs barrier) with 500 nm AlGaAs above and below; difference from NMC10 is that In cell has 12.5 Å now as compared to 13.8 Å before; absorption shows exciton @ 851 nm @4K
12	4-14-95	QW + Etalon	"The Half-Big-One" 18P (99.8%)/21.5(99.8%) top and bottom mirrors. Hoped to see lasing but didn't as of 5/17/95. Saw PL @ 805 nm.

NMC Sample #	Growth Date	Type of Sample	Description and Comments
13		QW	Like NMC11 but with 90 sec of GI on both sides; exciton @ 821 nm; $\alpha L = 3$ @4K
14		Etalon	27.5 P / 24 P with 1λ -bulk GaAs (not pseudoalloy spacer; R @ 4K didn't show FP peak (on low-res spectrometer), stop band was centered around 810 nm; transmission on the old SPEX showed peaks at 758, 768, and 851 nm; PL from Ar pump (15 mW) gave PL at 752 and 810 nm.
15	4-18-95	QW	Same as NMC11 but with thinner wells (21 sec (80 Å)), again with 500 nm AlGaAs above and below; exciton @ 843 nm @ 4K
16	4-20-95	Mirror	Start of switch to growing just GaAs/AlAs mirrors; 6 periods. R shows stop band centered around 850 nm
17	4-20-95	QW	20 x (80 Å InGaAs well, 920 Å GaAs barrier) with 500 nm AlGaAs above and below; In temp 670; absorption shows exciton @ 833 nm @4K
18	4-21-95	Etalon	5 P top/7.5 P bottom + 1λ GaAs spacer; R shows $\lambda_{FP}=871$ nm; fit gives $H = 612$ Å, $L=741$ Å, spacer = $4xH = 2447$ Å
19	4-21-95	QW + Etalon	Like NMC17 + NMC18; Jill's fit for 300K data gives $H=618$ Å, $L=750$ Å, $S=3720$ Å, with $\lambda_{FP}=892$ nm
20	4-23-95	QW + Etalon	19P (99.93%)/21.5P (99.92%), $3\lambda/2$ spacer with 2 wells like NMC17 at the two intensity peaks; didn't see FP dip. Saw NMC coupling to HH starting around 834 nm; tried on transmission measurement with 100 1-sec exposure and saw a little NMC, but very noisy; $2\Omega=2.6$ nm
21	4-24-95	QW	20 x (80 Å InGaAs well, 920 Å GaAs barrier) with 500 nm AlGaAs above and below; 90 sec GI before each well; In temp 670; absorption shows exciton @ 834 nm @4K
22	4-25-95	QW + Etalon	14P (99.5%)/16.5P (99.44%), $3\lambda/2$ spacer with 2 wells like NMC21 at the two intensity peaks; saw NMC coupling in two places (one given to Ove and Jill for B-field studies); $2\Omega=2.5$ nm

NMC Sample #	Growth Date	Type of Sample	Description and Comments
23	4-28-95	QW + Etalon	10P (97.69%)/12.5P (97.41%), $3\lambda/2$ spacer with 2 wells like NMC21 at the two intensity peaks; saw three dip NMC coupling in two places; saw coupling to HH and LH
24	4-29-95	QW + Etalon	25P (99.99%)/27.5P (99.99%), $3\lambda/2$ spacer with 2 wells like NMC17 at the two intensity peaks; didn't see NMC, but saw FP dip
25	4-29-95	QW	20 x (80 Å InGaAs well, 920 Å GaAs barrier) with 500 nm AlGaAs above and below; 90 sec GI before each well; absorption shows exciton @ 862 nm @4K; PL shows peak @ 863.8
26	5-2-95	QW + Etalon	25P (99.993%)/27.5P (99.992%), didn't see NMC, or FP dip, and was made to lase
27	5-2-95	QW + Etalon	10P (97.69%)/12.5P (97.41%), $3\lambda/2$ spacer with 2 wells like NMC21 at the two intensity peaks; saw three dip NMC; bigger intentional difference between QW's
28	5-6-95	QW + Etalon	10P (97.69%)/12.5P (97.41%), 1λ spacer with only one well in the center; saw NMC with HH, LH, and GaAs exciton
29	5-7-95	QW + "Etalon"	Messed up calibration sample because of program error
30	5-10-95	QW + Etalon	10P (97.69%)/12.5P (97.41%), $3\lambda/2$ spacer with 2 wells like NMC21 at the two intensity peaks; saw three dip NMC; smaller intentional difference between QW's

REFERENCES

- Agarwal, G.S., "Vacuum-field Rabi splittings in microwave absorption by Rydberg atoms in a cavity," *Phys. Rev. Lett.* **53**, 1732 (1984).
- Alves, E., Da Silva, M.F., Melo, A.A., Soares, J.C., Van Den Hoven, G.N., Polman, A., Evans, K.R., and Jones, C.R., "Lattice location and photoluminescence of Er in GaAs and $\text{Al}_{0.5}\text{Ga}_{0.5}\text{As}$," in Pomrenke *et al.* (1993) p. 175.
- Berger, J.D., Lyngnes, O., Gibbs, H.M., Khitrova, G., Nelson, Jr., T.R., Lindmark, E.K., Kavokin, A.V., Kaliteevski, M.A., and Zapasskii, V.I., "Magnetic-field enhancement of the exciton-polariton splitting in a semiconductor quantum-well microcavity: The strong coupling threshold," *Phys. Rev. B* **54**, 1975-1981 (1996).
- Berman, P.R., ed., *Cavity Quantum Electrodynamics* (Academic Press, Boston, 1994).
- Boltaks, B.I., *Diffusion and Point Defects in Semiconductors* (in Russian) (Nauka, Leningrad, 1972) p. 17.
- Born, M. and Wolf, E., *Principles of Optics* (Pergamon Press, New York, 1980), p. 55.
- Burstein, E. and Weisbuch, C., eds., *Confined Electrons and Photons: New Physics and Devices* (Plenum, New York, 1994).
- Callow, R.J., *The Industrial Chemistry of the Lanthanons, Yttrium, Thorium and Uranium* (Pergamon Press, New York, 1967).
- Chang, R., *Chemistry* (Random House, New York, 1988).
- Coffa, S. Polman, A., and Schwartz, R.N., eds., *Rare Earth Doped Semiconductors II* (Materials Research Society, Pittsburgh, 1996).
- Deppe, D.G. and Holonyak, N., "Atom diffusion and impurity-induced layer disordering in quantum well III-V semiconductor heterostructures," *J. Appl. Phys.* **64**, R93 (1988).
- Desurvire, E., *Erbium-Doped Fiber Amplifiers: Principles and Applications* (John Wiley & Sons, Inc., New York, 1994).
- Dieke, G.H., *Spectra and Energy Levels of Rare Earth Ions* (Interscience Publishers, New York, 1968).

REFERENCES—Continued

- Elsaesser, D.W., Colon, J.E., Yeo, Y.K., Hengehold, R.L., and Pomrenke, G.S., "Annealing studies of Er-implanted GaAs and the excitation mechanism of Er in GaAs," in Pomrenke *et al.* (1993) p. 251.
- Elsaesser, D.W., Yeo, Y.K., Hengehold, R.L., Evans, K.R., and Pedrotti, F.L., "Er-related deep centers in GaAs doped with Er by ion implantation and molecular beam epitaxy," *J. Appl. Phys.* **77**, 3919 (1995).
- Favennec, P.N., L'Haridon, H., Moutonnet, D., Salvi, M., and Gauneau, M., "Optical activation of ion implanted rare-earths," in Pomrenke *et al.* (1993) p. 181.
- Frenkel, I.A.I. *Kinetic Theory of Liquids* (Dover Publications, New York, 1955) pp. 10-11.
- Gelder, J.I., from the CD-ROM: *Animations for Introductory Chemistry* (Oklahoma State University, Stillwater, OK, 1994).
- Haroche, S. "Cavity quantum electrodynamics," in Dalibard, J., Raimond, J. M., and Zinn-Justin, J., eds., *Fundamental Systems in Quantum Optics* (Elsevier Science, New York, 1992) pp. 767-940.
- Higgins, T.V., "Light speeds communications," *Laser Focus World*, Aug., 67 (1995).
- Houdre, R., Stanley, R.P., Oesterle, U., Ilegems, M., and Weisbuch, C., "Room-temperature cavity polaritons in a semiconductor microcavity," *Phys. Rev. B* **49**, 16761 (1994).
- Houdre, R., Gibernon, J.L, Pellandini, P., Stanley, R.P, Oesterle, U., Weisbuch, C., O'Gorman, J., Roycroft, B., and Ilegems, M., "Saturation of the strong-coupling regime in a semiconductor microcavity: free-carrier bleaching of cavity polaritons," *Phys. Rev. B* **52**, 7810 (1995).
- Ivchenko, E.L., Kaliteevski, M.A., Kavokin, A.V., and Nesvizhskii, A.I., "Reflection and absorption spectra from microcavities with resonant Bragg quantum wells," *J. Opt. Soc. Am. B* **13**, 1061 (1996).
- Jahnke, F., Kira, M., Koch, S.W., Khitrova, G., Lindmark, E.K., Nelson, Jr., T.R., Wick, D.V., Berger, J.D., Lyngnes, O., and Gibbs, H.M., "Excitonic nonlinearities of semiconductor microcavities in the nonperturbative regime," *Phys. Rev. Lett.* **77**, 5257 (1996).

REFERENCES—Continued

- Jantsch, W. and Przybylinska, H. in Scheffler, M. and Zimmermann, R., eds., *Proceedings of the 23rd International Conference of the Physics of Semiconductors* (World Scientific, Singapore, 1996) p. 3025.
- Kincade, K., "Erbium lasers vie for spot in medical mainstream," *Laser Focus World*, Aug., 73 (1996).
- Kittel, C., *Introduction to Solid State Physics* (John Wiley & Sons, New York, 1986) p. 292.
- Laidig, W.D., Holonyak, Jr., N., Camras, M.D., Hess, K., Coleman, J.J., Dapkus, P.D., and Bardeen, J., "Disorder of an AlAs-GaAs superlattice by impurity diffusion," *Appl. Phys. Lett.* **38**, 776 (1981).
- Lanoo, M. and Delerue, C., "The theory of rare-earth impurities in semiconductors," in Pomrenke *et al.* (1993) p. 385.
- LePore, J.J., "An improved technique for selective etching of GaAs and Ga_{1-x}Al_xAs," *J. Appl. Phys.* **51**, 6441 (1981).
- Lindmark, E.K., Nelson, Jr., T.R., Khitrova, G., Gibbs, H.M., Kavokin, A.V., and Kaliteevski, M.A., "Three coupled oscillators: normal mode coupling in a microcavity with two different quantum wells," *Opt. Lett.* **21**, 994 (1996).
- Lyngnes, O., *Optical Properties of Semiconductor Nano-structures and Photoactive Yellow Protein* (University of Arizona, 1997) p. 35.
- Michel, J., Zheng, B., Palm, J., Oullette, E., Gan, F., and Kimerling, L.C., "Erbium doped silicon for light emitting devices," in Coffa *et al.* (1996) p. 317.
- Milonni, P.W. and Eberly, J.H., *Lasers* (John Wiley & Sons, New York, 1988) p. 86.
- Murthy, T.K.S. and Gupta, C.K., "Rare earth resources, their extraction and application," in Subbarao, E.C., and Wallace, W.E., eds., *Science and Technology of Rare Earth Materials* (Academic Press, New York, 1980).
- Nelson, Jr., T.R., Lindmark, E.K., Wick, D.V., Tai, K., Khitrova, G., Gibbs, H.M., "Normal-mode coupling in planar semiconductor microcavities," in Rarity, J. and Weisbuch, C. (1996a) pp. 43-57.

REFERENCES—*Continued*

- Nelson, Jr., T.R., Prineas, J.P., Khitrova, G., Gibbs, H.M., Lindmark, E.K., Shin, J.-H., Shin, H.-E., Lee, Y.-H., Tayebati, P., and Javniskis, L. "Room-temperature normal-mode-coupling in a semiconductor microcavity utilizing native-oxide AlAs/GaAs mirrors," *Appl. Phys. Lett.* **69**, 3031 (1996b).
- Ohanian, H.C., *Modern Physics* (Prentice-Hall, Inc., Englewood Cliffs, NJ, 1987).
- Panzarini, G. and Andreani, L.C., "Double quantum well in a semiconductor microcavity: three-oscillator model and ultrafast radiative decay," *Phys. Rev. B* **52**, 10780 (1995).
- Pau, S., Björk, G., Jacobson, J., Cao, H., and Yamamoto, Y., "Microcavity exciton-polariton splitting in the linear regime," *Phys. Rev. B* **51**, 14437 (1995).
- Payne, S. and Krupke, W.F., "A glimpse in the laser crystal ball," *Optics and Photonics News*, Aug., 31 (1997).
- Peyghambarian, N., Koch, S.W., and Mysyrowicz, A., *Introduction to Semiconductor Optics* (Prentice Hall, Englewood Cliffs, New Jersey, 1993) p. 62.
- Pomrenke, G.S., Klein, P.B., and Langer, D.W., eds., *Rare Earth Doped Semiconductors* (Materials Research Society, Pittsburgh, 1993).
- Priolo, F., Coffa, S., Franzo, G., and Polman, A., "Excitation mechanisms and light emitting device performances in Er-doped crystalline Si," in Coffa *et al.* (1996) p. 305.
- Rarity, J. and Weisbuch, C., eds., *Microcavities and Photonic Bandgaps: Physics and Applications* (Kluwer Academic Publishers, Boston, 1996).
- Rhee, J.-K., Citrin, D.S., Norris, T.B., Arakawa, Y., and Nishioka, M., "Femtosecond dynamics of semiconductor-micro cavity polaritons in the nonlinear regime," *Solid State Commun.* **97**, 941 (1996).
- Sanchez-Mondragon, J.J., Narozhney, N.B., and Eberly, J.H., "Theory of spontaneous-emission line shape in an ideal cavity," *Phys. Rev. Lett.* **51**, 550 (1983).
- Stanley, R.P., Houdre, R., Oesterle, U., Ilegems, M., and Weisbuch, C., "Coupled semiconductor microcavities," *Appl. Phys. Lett.* **65**, 2093 (1994).

REFERENCES—Continued

- Stanley, R.P., Houdre, R., Oesterle, U., Pellandini, P., and Ilegems, M., "Cavity-polaritons in semiconductor microcavities," in Rarity and Weisbuch (1996) p. 11.
- Szabadvary, F., "The history of the discovery and separation of the rare earths," in Gschneidner, Jr., K.A., and Eyring, L., eds., *Handbook on the Physics and Chemistry of Rare Earths: Volume 11—Two-Hundred-Year Impact of Rare Earths on Science* (North-Holland, New York, 1988) p. 33.
- Taguchi, A. and Ohno, T., "Total energy calculation for Er impurity in GaAs," *Mater. Sci. Forum* **196-201**, 627 (1995).
- Thompson, R.J., Rempe, G., and Kimble, H.J., "Observation of normal-mode splitting for an atom in an optical cavity," *Phys. Rev. Lett.* **68**, 1132 (1992).
- Trifonov, D.N., *The Rare-Earth Elements* (The Macmillan Company, New York, 1963).
- Trifonov, D.N., *Problems in the Study of Rare Earths* (Israel Program for Scientific Translations, Jerusalem, 1966).
- Tsimperidis, I., Gregorkiewicz, T., and Ammerlaan, C.A.J., "Excitation of rare earths in semiconductors by the excitonic Auger recombination," *Mater. Sci. Forum* **196-201**, 591 (1995).
- Wallace, W.E., *Rare Earth Intermetallics* (Academic Press, New York, 1973) p. 34.
- Weast, R.C., *CRC Handbook of Chemistry and Physics 55th Edition* (CRC Press, Cleveland, 1974) p. F-198.
- Weisbuch, C., Nishioka, M., Ishikawa, A., and Arakawa, Y., "Observation of the coupled exciton-photon mode splitting in a semiconductor quantum microcavity," *Phys. Rev. Lett.* **69**, 3314 (1992).
- Wick, D.V., Nelson, Jr., T.R., Lindmark, E.K., Gibbs, H.M., Khitrova, G., and Tai, K., "Semiconductor microcavities in the strong coupling regime," in *Proceedings of the SPIE—Physics and Simulation of Optoelectronic Devices IV*, SPIE Proceedings **2693**, 160-169 (1996).
- Wolf, S. and Tauber, R.N., *Silicon Processing for the VLSI Era Volume 1—Process Technology* (Lattice Press, Sunset Beach, CA, 1986).

REFERENCES—Continued

- Yariv, A., *Optical Electronics* (Holt, Rinehart and Winston, Inc., New York, 1985) p. 88.
- Yassievich, I.N. and Kimerling, L.C., "The mechanisms of electronic excitation of rare earth impurities in semiconductors," *Semicond. Sci. Technol.* **8**, 718-727 (1993).
- Yokoyama, H. and Ujihara, K., *Spontaneous Emission and Laser Oscillation in Microcavities* (CRC Press, Boca Raton, 1995).
- Zhang, T., Sun, J., Edwards, N.V., Moxey, D.E., Koibas, R.M., and Caldwell, P.J., "Photoluminescence study of energy transfer processes in erbium doped $\text{Al}_x\text{Ga}_{1-x}\text{As}$ grown by MBE," in Pomrenke *et al.* (1993) p. 257.
- Zhu, Y., Gauthier, D.J., Morin, S.E., Wu, Q., Carmichael, H.J., and Mossberg, T.W., "Vacuum Rabi splitting as a feature of linear-dispersion theory: analysis and experimental observations," *Phys. Rev. Lett.* **64**, 2499 (1990).